ETH
Eidgenössische Technische Hochschule Zürich
Swiss Federal Institute of Technology Zurich

A semi-Lagrangian approach to incompressible flows

Master Thesis

W.R. Tonnon

Thursday 4th November, 2021

Advisor: Prof. Dr. R. Hiptmair

Seminar of Applied Mathematics, D-MATH, ETH Zürich

Abstract

Already in 1757, Leonhard Euler introduced a set of equations—nowadays known as the Euler equations—to describe ideal fluids. Ever since, the Euler equations have received considerable attention from a wide range of communities including physicists, mathematicians, and engineers. To emphasize the difficulty of these equations, we note that only very recently blow-up of the exact solutions of the Euler equations was observed by Elgindi. In 1822, the Euler equations were extended the Navier-Stokes equations—the same equations with an added term to account for resistive effects. The existence of smooth and global solutions to the Navier-Stokes equation is an open problem that is one of the millenial problems defined by the Clay Mathematics Institute. The age of the problem and the considerable attention it has received, show the difficulty and importance of the mathematical description of fluids.

Despite the theoretical difficulties, the Euler and Navier-Stokes equations have been succesfully used in practice by physicists and engineers. Since in practical situations the solutions to these equations are not known, one often resorts to the use of numerical methods. A plethora of numerical methods has been developed for solving the Euler and Navier-Stokes equations. Traditional finite-element methods work very well for the Navier-Stokes equations with a dominant diffussion term, while traditional finite-volume methods work well for the Euler equations or, equivalently, the Navier-Stokes equations without diffussion term. A practical problem that requires attention is that of solving the Navier-Stokes equations with a very weak diffusion term. In this case, the solution exhibits properties of both the Euler equations and the Navier-Stokes equations with strong diffusion. In this work, we develop a numerical scheme on the basis of semi-Lagrangian, vectorial advection. Numerical experiments show that this scheme performs very well for any value of the viscosity.

The Euler and Navier-Stokes equations can also be coupled with the Maxwell equations to obtain a mathematical description of magnetohydrodynamics. In this description, it is assumed that the fluid carries the magnetic field along, while the magnetic field exhibits a force on the fluid through the Lorentz force. We extend the scheme that we developed for the Navier-Stokes equations to magnetohydrodynamics. In this case, we show that the semi-Lagrangian-based scheme does not yield a natural discretization of the Lorentz force and that this leads to instabilities. It is also shown that the scheme fails to satisfy a discrete energy bound and thus it is not unexpected that instabilities occur.

The code used for all numerical experiments in this thesis is made available under the GNU Public License at [61].

Acknowledgements

First and foremost, I would like to thank Prof. Dr. Ralf Hiptmair for his supervision throughout this project. You gave me a lot of freedom in my research, but you were also always there to support me in case I needed it. I would also like to thank Dr. Cecilia Pagliantini and Dr. Kaibo Hu for the fruitful discussions that led to the understanding of the instabilities observed for the magnetohydrodynamics equations.

I would also like to thank my parents, Jaap and Marjo, and my sister, Mijke, for supporting me throughout my studies. Lastly, I would like to thank my friends in Zürich for giving me a good time before, during, and after the lockdowns.

Contents

Chapter 1

Semi-Lagrangian Advection of Differential Forms

1.1 Introduction

We search $\boldsymbol{u}(x,t)$ on a bounded domain $\Omega \subset \mathbb{R}^n$ such that

$$\partial_t \boldsymbol{u} - \mathbf{curl}\, \varepsilon\, \mathbf{curl}\, \boldsymbol{u} + \mathbf{grad}(\boldsymbol{\beta} \cdot \boldsymbol{u}) + \mathbf{curl}\, \boldsymbol{u} \times \boldsymbol{\beta} = \boldsymbol{f}, \qquad \text{in } \Omega, \tag{1.1}$$

$$\boldsymbol{u} = \boldsymbol{g}, \qquad \text{on } \Gamma_{in}, \tag{1.2}$$

where $\varepsilon > 0$, $\boldsymbol{\beta} : \Omega \mapsto \mathbb{R}^n$, $\boldsymbol{f} : \Omega \mapsto \mathbb{R}^n$, and $\boldsymbol{g} : \Omega \mapsto \mathbb{R}^n$ are given. $\partial\Omega$ and Γ_{in} denote the boundary of Ω and $\Gamma_{in} = \{x \in \partial\Omega; \boldsymbol{\beta} < 0\}$. We will assume that the velocity $\boldsymbol{\beta} : \Omega \mapsto \mathbb{R}^n$ satisfies $\operatorname{div} \boldsymbol{\beta} = 0$. These equations have variety of applications including (but not limited to) fluid dynamics, plasma, and astrophysics. These applications often require values for ε that are small compared to the other quantities.

For the scalar version of equation (1.1), we search $u(x,t)$ on a bounded domain $\Omega \subset \mathbb{R}^n$ such that

$$\partial_t u - \operatorname{div} \varepsilon\, \mathbf{grad}\, u + \boldsymbol{\beta} \cdot \mathbf{grad}\, u = f, \qquad \text{in } \Omega, \tag{1.3}$$

$$u = g, \qquad \text{on } \partial\Omega, \tag{1.4}$$

where $\varepsilon > 0$, $\boldsymbol{\beta} : \Omega \mapsto \mathbb{R}^n$, $f : \Omega \mapsto \mathbb{R}$, and $g : \Omega \mapsto \mathbb{R}$ are given. This type of equation has received considerable attention in literature. The most common approaches consider some form of stabilized Eulerian scheme; a type of scheme where first spatial discretization is performed after which a suitable timestepping scheme is chosen. Some examples of this type of methods include discontinuous Galerkin schemes [30, 34, 52] and subgrid viscosity techniques [19]. These methods turn out to be particularly robust against spurious oscillations [24, 53, 41]. However, if $\varepsilon > 0$ is large, these techniques require solving a large non-symmetric sparse system of non-linear equations. This requires a lot of computational effort and is therefor undesirable.

An alternative to the above methods are semi-Lagrangian schemes. These types of schemes perform time discretization in the Lagrangian frame of reference in a similar fashion as done for Lagrangian schemes. However, where traditional Lagrangian schemes advect the entire mesh, semi-Lagrangian schemes project the fields back onto a fixed-mesh. This avoids the large computational complexity involved with remeshing at every timestep. Also, due to the discretization in the Lagrangian frame, we avoid solving the non-symmetric system of equations. A plethora of research is available on semi-Lagrangian schemes for scalar advection-diffusion equations (1.1) [6, 7, 8, 17, 20, 25, 45, 54, 58]. Also, some work has been done on semi-Lagrangian schemes for equation (1.1) [26, 28, 27]. However, these works only address a first-order semi-Lagrangian scheme. In [9], a second-order semi-Lagrangian scheme was introduced for scalar advection-diffusion equations, where elements of the mesh were only approximately transported along the velocity field. Instead of transporting the elements exactly (and thus in general introducing curved boundaries), the vertices of the elements were transported and interpolated to form an approximation of the transported element. In this work, we will use ideas of [27] and [9] to construct a second-order scheme for equation (1.1). [27] also includes an elaborate analysis of the introduced first-order semi-Lagrangian scheme for equation (1.1). This shows that the constant of convergence remains bounded as $\varepsilon \to 0$: a property that is not common in Eulerian schemes. For an overview of the analysis of semi-Lagrangian schemes we refer to [27, Chapter 5].

1.2 The calculus of differential forms

This section is meant as an introduction to the notation that will be used in this work. For background information on differential geometry and differential forms, the author refers to [13], [32], and [57]. In this work, we will follow the notation as introduced in [27]. We repeat the definitions that will be relevant in our work.

Let Ω be a smooth, compact, oriented, d-dimensional Riemannian manifold with boundary and let $T_x\Omega$ be the tangent space of Ω at $x \in \Omega$. We denote by $\Lambda^k(\Omega)$ the set of differential k-forms on Ω and by $\mu \in \Lambda^d(\Omega)$ the volume form of Ω. The set $S(k,d)$ contains the permutations σ of numbers $\{1,\ldots,d\}$ such that $\sigma(1) < \ldots < \sigma(k)$ and $\sigma(k+1) < \ldots < \sigma(d)$, and $\operatorname{sign}(\sigma)$ denotes the sign of the permutation. In the remainder of this section, $\boldsymbol{v}_1,\ldots,\boldsymbol{v}_d$ denote arbitrary smooth vector fields, while $\boldsymbol{e}_1,\ldots,\boldsymbol{e}_d$ denotes an orthonormal frame with respect to a Riemannian manifold. We will need the following definitions from [27].

Definition 1 [57, Definition 1.2.2a] The exterior product $\wedge : \Lambda^j(\Omega) \times \Lambda^k(\Omega) \mapsto$

$\Lambda^{j+k}(\Omega)$ is defined by

$$(\omega \wedge \eta)(\boldsymbol{v}_1, \dots, \boldsymbol{v}_{j+k}) = \sum_{\sigma \in S(k,j+k)} \operatorname{sign}(\sigma)\omega(\boldsymbol{v}_{\sigma(1)}, \dots, \boldsymbol{v}_{\sigma(j)})\eta(\boldsymbol{v}_{\sigma(j+1)}, \dots, \boldsymbol{v}_{\sigma(j+k)}).$$

Definition 2 [57, Definition 1.2.2b] The scalar product $(\cdot,\cdot) : \Lambda^k(\Omega) \times \Lambda^k(\Omega) \mapsto \Lambda^0(\Omega) = C^\infty(\Omega)$ is defined by

$$(\omega, \eta) = \sum_{\sigma \in S(k,d)} \operatorname{sign}(\sigma)\omega(\boldsymbol{e}_{\sigma(1)}, \dots, \boldsymbol{e}_{\sigma(k)})\eta(\boldsymbol{e}_{\sigma(1)}, \dots, \boldsymbol{e}_{\sigma(k)}).$$

Definition 3 [57, Definition 1.2.2c] The Hodge operator $\star : \Lambda^k(\Omega) \mapsto \Lambda^{d-k}(\Omega)$ yields the unique $(d-k)$-form $\star\omega$ such that

$$\eta \wedge \star\omega = (\eta, \omega)\mu.$$

Definition 4 The scalar product $(\cdot,\cdot)_\Omega : \Lambda^k(\Omega) \times \Lambda^k(\Omega) \mapsto \mathbb{R}$ is defined by

$$(\omega, \eta)_\Omega = \int_\Omega \omega \wedge \star\eta.$$

Definition 5 The scalar product $(\cdot,\cdot)_\Omega : \Lambda^l(\Omega) \times \Lambda^k(\Omega) \mapsto \mathbb{R}$, $l + k = d$ is defined by

$$(\omega, \eta)_\Omega = \int_\Omega \omega \wedge \eta.$$

Definition 6 [57, Definition 1.2.2e] The exterior derivative $\mathrm{d} : \Lambda^{k-1}(\Omega) \mapsto \Lambda^k(\Omega)$ at $x \in \Omega$ is defined by

$$\begin{aligned} \mathrm{d}\omega(\boldsymbol{v}_1, \dots, \boldsymbol{v}_k) = &\sum_{0 \le j \le k} D_{\boldsymbol{v}_j}[\omega(\boldsymbol{v}_1, \dots, \hat{\boldsymbol{v}}_j, \dots, \boldsymbol{v}_k)] \\ &+ \sum_{0 \le i < j \le k} (-1)^{i+j}\omega([\boldsymbol{v}_i, \boldsymbol{v}_j], \boldsymbol{v}_0, \dots, \hat{\boldsymbol{v}}_i, \dots, \hat{\boldsymbol{v}}_j, \dots, \boldsymbol{v}_k), \end{aligned}$$

where $D_X f$ denotes the differential of $f \in \Lambda^0(\Omega)$ with respect to the vector field X on Ω, $[\cdot,\cdot]$ denotes the Lie Bracket, and $\hat{\boldsymbol{v}}_i$ means that $\boldsymbol{v}_i$ is omitted.

Definition 7 [57, Definition 1.2.2d] The contraction $i_{\boldsymbol{\beta}} : \Lambda^k(\Omega) \mapsto \Lambda^{k-1}(\Omega)$ for a vector field $\boldsymbol{\beta}$ is defined by

$$(i_{\boldsymbol{\beta}}\omega)(\boldsymbol{v}_1, \dots, \boldsymbol{v}_{k-1}) = \omega(\boldsymbol{\beta}, \boldsymbol{v}_1, \dots, \boldsymbol{v}_{k-1}).$$

Definition 8 [57, p. 21] The Lie derivative $L_{\boldsymbol{\beta}} : \Lambda^k(\Omega) \mapsto \Lambda^k(\Omega)$ is defined by

$$L_{\boldsymbol{\beta}} = \mathrm{i}_{\boldsymbol{\beta}}\mathrm{d}\omega + \mathrm{d}\mathrm{i}_{\boldsymbol{\beta}}\omega.$$

Definition 9 [57, p. 22] Let Ω' be a manifold and $\varphi : \Omega \mapsto \Omega'$ a smooth map, then the pullback $\varphi^* : \Lambda^k(\Omega') \mapsto \Lambda^k(\Omega)$ is defined as

$$(\varphi^*\omega)_x(\boldsymbol{v}_1, \dots, \boldsymbol{v}_k) = \omega_{\varphi(x)}(D\varphi_x \boldsymbol{v}_1, \dots, D\varphi_x \boldsymbol{v}_k),$$

where ω_x is the k-form associated with ω at $x \in \Omega$ and $D\varphi_x$ is the differential of φ at x.

Definition 10 [27] Tthe trace $\mathrm{tr} : \Lambda^k(\Omega) \mapsto \Lambda^k(\partial\Omega)$ is the pullback of the inclusion map $i : \Omega \mapsto \partial\Omega$.

Definition 11 [26, p. 8] The exterior coderivative $\delta : \Lambda^k(\Omega) \mapsto \Lambda^{k-1}(\Omega)$ yields the unique $(k-1)$-form $\delta\omega$ such that

$$\star\delta\omega = (-1)^k \mathrm{d} \star \omega.$$

An important result is the following [13]

Theorem 1 Let $\boldsymbol{\beta} : \Omega \mapsto T\Omega = \mathbb{R}^d$ be stationary and Lipschitz-continuous, then

$$\frac{\partial}{\partial\tau} X_\tau(x) = \boldsymbol{\beta}(X_\tau(x)) \tag{1.5}$$

$$X_0(x) = x \tag{1.6}$$

is well-defined and yields the following equality for $\omega \in \Lambda^k(\Omega)$

$$L_{\boldsymbol{\beta}}\omega = \left.\frac{\partial}{\partial\tau} X_\tau^* \omega \right|_{\tau=0}$$

We are now ready to formulate the nonstationary advection-diffusion problem as in [27]: we search $\omega(t) \in \Lambda^1(\Omega)$ such that

$$\partial_t\omega + \delta\varepsilon\mathrm{d}\omega + L_{\boldsymbol{\beta}}\omega = \varphi, \qquad \text{in } \Omega, \tag{1.7a}$$

$$\omega = \psi_g, \qquad \text{on } \Gamma_{in}, \tag{1.7b}$$

$$\omega|_{t=0} = \omega_0, \tag{1.7c}$$

where ω_0 and $\boldsymbol{\beta}$ are given, $\psi_g \in \Lambda^1(\Omega)$ is the differential form corresponding to the vector proxy $\boldsymbol{g}$ and also given. Γ_0 denotes the boundary of Ω and $\Gamma_{in} = \{x \in \Gamma_0; \boldsymbol{\beta} \cdot \boldsymbol{n} < 0\}$ is the inflow boundary. From theorem 1 it is clear that equation (1.7) constitutes a transport problem for $\varepsilon = 0$. In fact, we find the formal solution

$$(\omega(t))_x = (X_{-\tau}^*\omega(0))_x + \int_0^t (X_{\tau-t}^*\varphi(\tau))_x \mathrm{d}\tau, \tag{1.8}$$

where we assumed for simplicity that $\boldsymbol{\beta} \cdot n = 0$ on $\partial\Omega$.

1.3 Discrete differential forms

In this section, we introduce a generalization to higher orders for differential Whitney p-forms, a lowest-order discrete differential form. This type of discrete differential forms has the advantage that its degrees of freedom lie on p-simplices [21] as opposed to on q-simplices with $q > p$ as is common for higher-order discrete differential forms [3]. Good resources on the theory of discrete differential forms are [4] and [3]. For an elaborate overview of the theory presented in this section, we refer to [21].

Let $\Omega \subset \mathbb{R}^d$ be a polyhedral domain, then we can define a mesh m as a partition of Ω into d-simplices in such a way that two of those simplices are only allowed to intersect on a common face of dimension $0 \leq p \leq d-1$. Let $\mathcal{S}^p$ and $|\mathcal{S}^p|$ be the space of p-simplices of m and its cardinality. A p-chain c is linear combination of simplices in $\mathcal{S}^p$ and can be represented as a sum $c = \sum_{s \in \mathcal{S}^p} c_s s$. In practice, c can be stored as a vector $(c_s)_{s \in \mathcal{S}^p}$ and the space of p-chains thus forms a vector space. A p-cochain is an element of the dual space associated with the space of p-chains and can be associated with a differentiable p-form as we will see later.

A p-cochain $\overline{b}$ can be constructed from a differential p-form b by defining it as the map $c \mapsto \sum_{s \in \mathcal{S}^p} c_s \int_s b$ or, on a computer, as the vector $\overline{b} = (\int_s b)_{s \in \mathcal{S}^p}$. The conversion from a differential p-form to a p-cochain is called the deRham map or the projection map, $\overline{b} = \mathcal{R}b$. Given a p-cochain $\overline{b} : c \mapsto \sum_{s \in \mathcal{S}^p} c_s b_s$ and suitable differentiable p-forms w^s (to be defined later), we can construct the differential p-form $b = \sum_{s \in \mathcal{S}^p} b_s w^s$. This construction is known as the Whitney map (or prolongation), $b = \mathcal{P}\overline{b}$. These constructions show us that p-cochains are the discrete analogue of differential p-forms.

Another important operator is the boundary operator $\partial : \mathcal{S}^p \mapsto \mathcal{S}^{p-1}$. This operator takes a p-simplex σ and maps it to a sum of its faces ($p-1$-simplices), $\partial s = \sum_{s \in \mathcal{S}^{p-1}} \boldsymbol{d}_\sigma^s s$, where

$$\boldsymbol{d}_\sigma^s = \begin{cases} 0, & s \notin \partial\sigma, \\ 1, & s \in \partial\sigma, \text{ orientation } s \text{ agrees with orientation induced by } \sigma, \\ -1, & s \in \partial\sigma, \text{ orientation } s \text{ disagrees with orientation induced by } \sigma. \end{cases}$$

The map can be linearly extended to p-chains as $\partial c = \sum_{s \in \mathcal{S}^p} c_s \partial s$. Using the boundary operator and Stokes' theorem, we can define the concept of exterior derivative d for p-cochains.

Suppose b is a differential p-form, then $\mathrm{d}b$ is a differential $p+1$-form. Suppose we are given $\mathcal{R}b$ and we are interested in finding $\mathcal{R}\mathrm{d}b$. The exterior derivative of $\mathcal{R}b$ is not defined, but we can take the exterior derivative of $\mathcal{P}\mathcal{R}b$. This will yield a $p+1$-form (that is in general different from $\mathrm{d}b$), which we can project onto a $p+1$-cochain in order to represent it on a computer.

This means that we are interested in integrating $\mathrm{d}\mathcal{P}\mathcal{R}b$ over $p+1$-chains, say $\sum_{s\in\mathcal{S}^p} c_s s$. Using Stokes' theorem, we find

$$\int_{\sum_{s\in\mathcal{S}^{p+1}} c_s s} \mathrm{d}\mathcal{P}\mathcal{R}b = \int_{\partial\left(\sum_{s\in\mathcal{S}^{p+1}} c_s s\right)} \mathcal{P}\mathcal{R}b = \sum_{s\in\mathcal{S}^{p+1}} c_s \int_{\partial s} \mathcal{P}\mathcal{R}b.$$

The right-hand side of this equation can be evaluated as $\mathcal{P}\mathcal{R}b$ is a p-form and the operator ∂ reduces the $p+1$-simplex s to a p-simplex ∂s, thus the above equation is well-defined. Recall that the prolongation operator $\mathcal{P}$ implicitly depends on chosen w^s. It can be shown that the w^s we find later has the property that $\mathcal{R}\mathrm{d}\mathcal{P}\mathcal{R}b = \mathcal{R}\mathrm{d}b$ [21].

Let $\sigma \in \mathcal{S}^p$ and $s \in \mathcal{S}^{p-1}$, then we can define $\lambda_{\sigma-s}(x)$ to be the barycentric coordinate associated with element σ and node l, where node l is the only node of σ that is not contained in s. This allows us to define the differential Whitney p-forms, w^s, as follows [21].

Definition 12 The differential Whitney p-form w^σ of polynomial degree 1 associated to the p-simplex σ is

$$w^\sigma = \sum_{s\in\mathcal{S}^{p-1}} \boldsymbol{d}_\sigma^s \lambda_{\sigma-s} \mathrm{d}w^s,$$

where $w^n = \lambda_n$ for $p = 0$ and $\Lambda^p_{h,1}(\Omega) = \operatorname{span}\{w^\sigma; \sigma \in \mathcal{S}^p\}$.

It now remains to extend the definition of differential Whitney p-forms to higher polynomial degrees. We write $\boldsymbol{k} = (k_0, \ldots, k_d)$ for an ordered set of integers with $k_i \geq 0$ and denote by $|k|$ their sum. Then, we define $\mathcal{I}(d+1, |k|)$ as the set of multi-index $\boldsymbol{k}$ with $d+1$ components and sum $|k|$. In the remainder of the document, we will also use the notation $\boldsymbol{\lambda}^{\boldsymbol{k}} = \prod_{i=0}^d (\lambda_i)^{k_i}$. To each multi-index $\boldsymbol{k} \in \mathcal{I}(d+1, |k|)$ and d-simplex σ corresponds a map $\mathcal{K}$ defined as

$$\mathcal{K} = \mathcal{H}\left(\frac{1}{k_0+1}, a_0\right) \circ \mathcal{H}\left(\frac{k_0+1}{k_1+k_0+1}, a_1\right) \circ \cdots \circ \mathcal{H}\left(\frac{k_{d-1}+\cdots+k_1+1}{k+1}, a_d\right),$$

where $a_0, \ldots, a_d$ are the vertices of σ and $\mathcal{H}$ is the mapping

$$\mathcal{H}(r, \boldsymbol{a}) : \mathbb{R}^d \ni \boldsymbol{x} \mapsto \boldsymbol{a} + r(\boldsymbol{x} - \boldsymbol{a}) \in \mathbb{R}^d.$$

Using $\mathcal{K}$, we can define the degrees of freedom associated with differential Whitney p-forms as the small p-simplices associated with σ, where small simplices are defined as follows.

Definition 13 We call small p-simplices the images $\mathcal{K}(S)$ for all (big) p-simplices $S \in \mathcal{S}^p$ and all $\boldsymbol{k} \in \mathcal{I}(d+1, k)$, and denote them by $s = \{\boldsymbol{k}, S\}$.

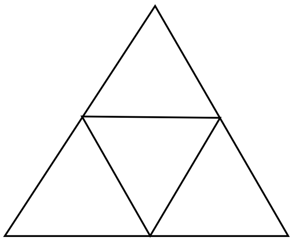

Figure 1.1: Degrees-of-freedom of a second-order element in 2D. All the edges between the different connection points are degrees-of-freedom. In 3D, we simply have all these degrees-of-freedom on the faces of the simplex.

We refer to fig. 1.1 for an example of small simplices of a second-order simplex in 2D. For a 3D simplex, there are no interior degrees-of-freedom and we the degrees-of-freedom of the faces agree with those presented in fig. 1.1.

We define the differential Whitney p-forms to small-simplices as follows.

Definition 14 The differential Whitney p-forms associated to small simplex $s = \{\boldsymbol{k}, S\}$ is $w^s = \boldsymbol{\lambda}^{\boldsymbol{k}} w^S$, where w^S is the differential Whitney p-form of polynomial degree 1 associated to S as defined in definition 12. We denote and $\Lambda^p_{h,1}(\Omega) = \text{span}\{w^s; s = \{\boldsymbol{k}, S\}, \boldsymbol{k} \in \mathcal{I}(d+1, k), S \in \mathcal{S}^p\}$.

It can be shown that the differential Whitney p-forms constitute a partition of unity, but they are not linearly independent [21]. In practice this means that we have to find a least-squares solution when applying the deRham map. Also, it can be shown that the differential Whitney p-forms satisfy the deRham complex [21].

In the remainder of this text, we may leave out the Whitney map $\mathcal{P}$ if it is clear from the context that it should be applied.

1.4 Discrete material derivative

Consider the material derivative for a time-dependent differential p-form ω

$$\frac{D\omega}{Dt} := \frac{\partial}{\partial \tau} X^*_\tau \omega(t+\tau)\bigg|_{\tau=0} = \partial_t \omega + L_\beta \omega. \tag{1.9}$$

Using explicit Euler and Heun's method, we obtain for a timestep $\tau > 0$

$$\frac{D\omega}{Dt} = \frac{1}{\tau}\left[\omega(t) - X^*_{-\tau}\omega(t-\tau)\right] + \mathcal{O}(\tau) \tag{1.10}$$

and

$$\frac{D\omega}{Dt} = \frac{1}{2\tau}\left[3\omega(t) - 4X^*_{-\tau}\omega(t-\tau) + X^*_{-2\tau}\omega(t-2\tau)\right] + \mathcal{O}(\tau^2).$$

For simplicity of notation, we will restrict the following explanation to the case of first order. However, all that follows is directly applicable to the second-order case unless stated otherwise.

Suppose that, instead of a time-dependent p-form $\omega(t)$, we have a p-cochain defined at every timestep denoted by $\bar{\omega}^n, \bar{\omega}^{n+1}$, etc. We cannot simply plug in $\bar{\omega}^n$ for ω, since the operator $X^*_{-\tau}$ is not defined on p-cochains. Instead, we first apply the Whitney map $\mathcal{P}$ to obtain a differential p-form from the p-cochain and plug that into equation (1.10). We find

$$\frac{D\bar{\omega}}{Dt} = \frac{1}{\tau}\left[\bar{\omega}^n - X^*_{-\tau}\mathcal{P}\bar{\omega}^{n-1}\right] + \mathcal{O}(\tau).$$

Since $X^*_{-\tau}\mathcal{P}\bar{\omega}^{n-1}$ is not a p-cochain, we need to apply the deRham map $\mathcal{R}$. We find

$$\frac{D\bar{\omega}}{Dt} = \frac{1}{\tau}\left[\bar{\omega}^n - \mathcal{R}X^*_{-\tau}\mathcal{P}\bar{\omega}^{n-1}\right] + \mathcal{O}(\tau).$$

Recall from section 1.3 that evaluating the deRham map $\mathcal{R}$ is equivalent to evaluating integrals of p-forms over (small) p-simplices. In this work, we will focus on the evaluation of 1-forms and thus integrals over (small) 1-simplices, that is, straight lines. Let us denote by e such a 1-simplex, and let e_1 and e_2 denote its vertices. We are interested in evaluating $\int_e X^*_{-\tau}\mathcal{P}\bar{\omega}^{n-1}$. We do this in the following way

$$\int_e X^*_{-\tau}\mathcal{P}\bar{\omega}^{n-1} = \int_{X_{-\tau}(e)} \mathcal{P}\bar{\omega}^{n-1} \approx \int_{\bar{X}_{-\tau}(e)} \mathcal{P}\bar{\omega}^{n-1}, \tag{1.11}$$

where

$$\bar{X}_{-\tau}(e) = \left\{(1-t)X_{-\tau}(e_1) + tX_{-\tau}(e_2); 0 \leq t \leq 1\right\}.$$

Instead of transporting the edge e using the flow $X_{-\tau}$ exactly, we instead only transport the vertices back and obtain a linear (second-order) approximation of the transported edge. See fig. 1.2 for an illustration. We can approximate the flow by solving equation (1.5) using explicit Euler or Heun's method for the first- and second-order case, respectively.

In fig. 1.2, we can also see that the approximate transported edge spans four different elements of the mesh. If we need to evaluate equation (1.11), it can happen that there are discontinuities of $\mathcal{P}\bar{\omega}^{n-1}$ along $\bar{X}_{-\tau}(e)$. Therefore, it is not recommended to apply a quadrature rule over the entire integral. Instead, we split $\bar{X}_{-\tau}(e)$ in four different pieces that are each contained in a single element. Then, we can evaluate the integrals over these individual pieces exactly, because we know that $\mathcal{P}\bar{\omega}^{n-1}$ is of polynomial form when restricted to individual elements of the mesh (see section 1.3).

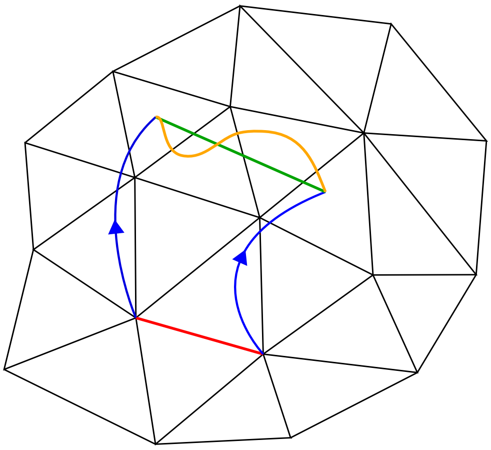

Figure 1.2: Edge e (in red) is transported using the flow $\boldsymbol{\beta}$ (in blue). The exact transported edge $X_\tau(e)$ and the approximate transported edge $\bar{X}_\tau(e)$ are given in orange and green.

1.5 A first- and second-order scheme

We now have all the tools to our disposal to construct a fully-discrete first- and second-order scheme to solve equation (1.7). We have the following weak formulation

$$\int_\Omega (\overbrace{\partial_t \omega + L_{\boldsymbol{\beta}}\omega}^{\frac{D\omega}{Dt}}) \wedge \star\eta + \int_\Omega \mathrm{d}\omega \wedge \star\mathrm{d}\eta = \int_{\partial\Omega} \mathrm{d}\omega \wedge \star\eta + \int_\Omega f \wedge \star\eta, \quad \forall \eta \in \Lambda^1(\Omega), \tag{1.12a}$$

where $\frac{D\omega}{Dt}$ denotes the material derivative with respect to the flow $\boldsymbol{\beta}$. Using the finite-dimensional subspaces as defined in section 1.3 and using the discrete material derivative as defined in section 1.4, we get the following first-order scheme. Given $\bar{\varpi}^{n-1} \in \Lambda^1_{h,1}(\Omega)$, we search $\bar{\varpi}^n \in \Lambda^1_{h,1}(\Omega)$ such that

$$\int_\Omega \frac{1}{\tau}\left[\bar{\varpi}^n - \mathcal{R}\bar{X}^*_{-\tau}\mathcal{P}\bar{\varpi}^{n-1}\right] \wedge \star\eta + \int_\Omega \mathrm{d}\bar{\varpi}^n \wedge \star\mathrm{d}\eta \tag{1.13a}$$

$$= \int_{\partial\Omega} \mathrm{d}\bar{\varpi}^n \wedge \star\eta + \int_\Omega f \wedge \star\eta, \quad \forall \eta \in \Lambda^1_{h,1}(\Omega), \tag{1.13b}$$

where $\tau > 0$ denotes the chosen timestep. A second-order scheme can be constructed as follows. Given $\bar{\varpi}^{n-2}, \bar{\varpi}^{n-1} \in \Lambda^1_{h,2}(\Omega)$, we search $\bar{\varpi}^n \in \Lambda^1_{h,2}(\Omega)$

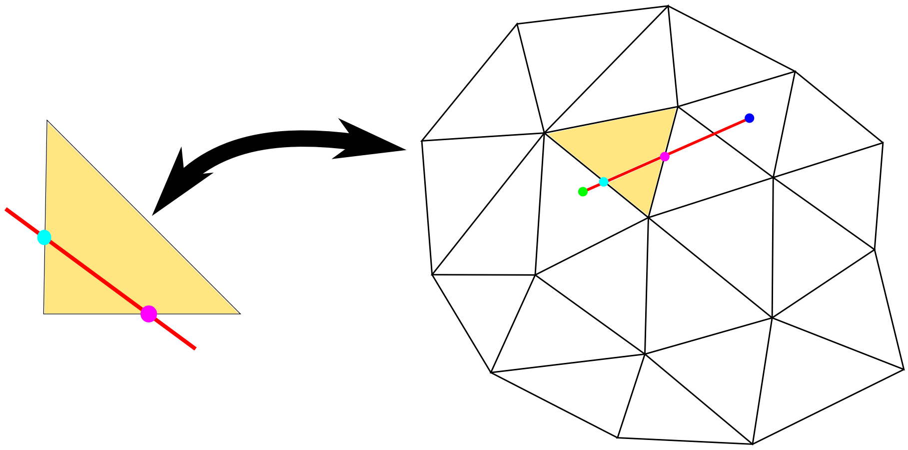

Figure 1.3: The red line indicates the line that spans multiple elements. On the left we see the reference element corresponding to the yellow element in the mesh on the right.

such that

$$\begin{aligned}\int_\Omega \frac{1}{2\tau}\left[3\bar{\omega}^n - 4\mathcal{R}\bar{X}^*_{-\tau}\mathcal{P}\bar{\omega}^{n-1} + \mathcal{R}\bar{X}^*_{-2\tau}\mathcal{P}\bar{\omega}^{n-2}\right]\wedge\star\eta \\ + \int_\Omega \mathrm{d}\bar{\omega}^n\wedge\star\mathrm{d}\eta = \int_{\partial\Omega}\mathrm{d}\bar{\omega}^n\wedge\star\eta + \int_\Omega f\wedge\star\eta, \qquad \forall\eta\in\Lambda^1_{h,2}(\Omega).\end{aligned}$$

1.6 Implementation

This section is meant to shed some light on implementation details of the numerical scheme. We will not go into details regarding the implementation of discrete differential forms as those details can be found in [21]. Instead, we will focus on a problem first described in section 1.4. In that section, we encountered the problem that a transported edge could span multiple elements in the mesh and we need to split this edge in individual parts that are all contained in a single element. The presented algorithm works for simplicial meshes of dimension 2 and higher.

Consider the situation on the right-hand side of fig. 1.3. We would like to split the red line into four different segments that are each contained in a single element. To do so, we will ”walk” over the red line and store the element ids of the elements we pass. Indeed, we start our walk at the green dot and we walk as far as we can without leaving the first element, that is, until we reach the light-blue dot. As soon as we reach the blue dot, we store the element id in an array for later reference. Currently, we are standing on the light blue dot and thus we are standing on a face of the first element. The next element we will be walking is the element on the other side of the face.

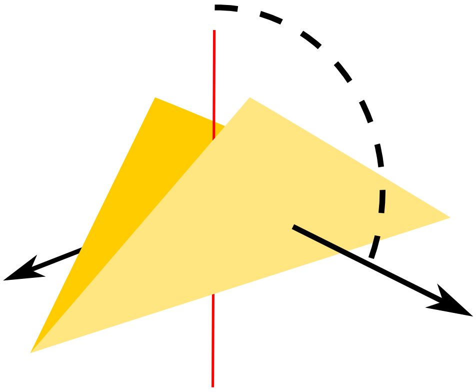

Figure 1.4: The red line indicates the walking path. The yellow faces indicate the faces of the next element that contain the edge. The corresponding black arrows indicate their normal vectors. The pictured angle clearly needs to be larger than 90 degrees.

We consult the mesh connectivity table to obtain the id of this element. Then, we walk further down the line until we reach the purple point, consult the mesh connectivity table again to find the next element, and so on. This ends when we reach the blue point.

It remains to discuss how we determine how far we can walk before we leave the element. Suppose we are standing at the light blue dot and would like to see how far we can walk across the yellow element. To figure this out, we transform the mesh element to its reference element and we also transform the direction of the red line and the light blue and purple point to the reference space (see left side of fig. 1.3). Since we know the coordinates of the vertices in the reference space, we can compute how far we can walk.

In the above example, we implicitly assumed that we would always walk across faces of the element. However, in practice, it is also possible to hit a vertex or (in 3D) an edge. If we cross a vertex we can, just like we did with a face, check the mesh connectivity table to see which elements are touching this vertex. However, this could be many elements and we have to make sure to take the right one. We can decide that by going one step (of half the mesh-width) further down the path and then checking for every element whether we are currently in that element. Note that this is rather computationally expensive, but this is not an issue as hitting a vertex exactly (up to numerical precision) barely happens. In 3D, we have a similar issue when we hit edges. We can find the elements that touch the edge, but we need to decide which of those elements we need. To do so, we take for every element its two faces that contain the edge. If the normal vectors of both of

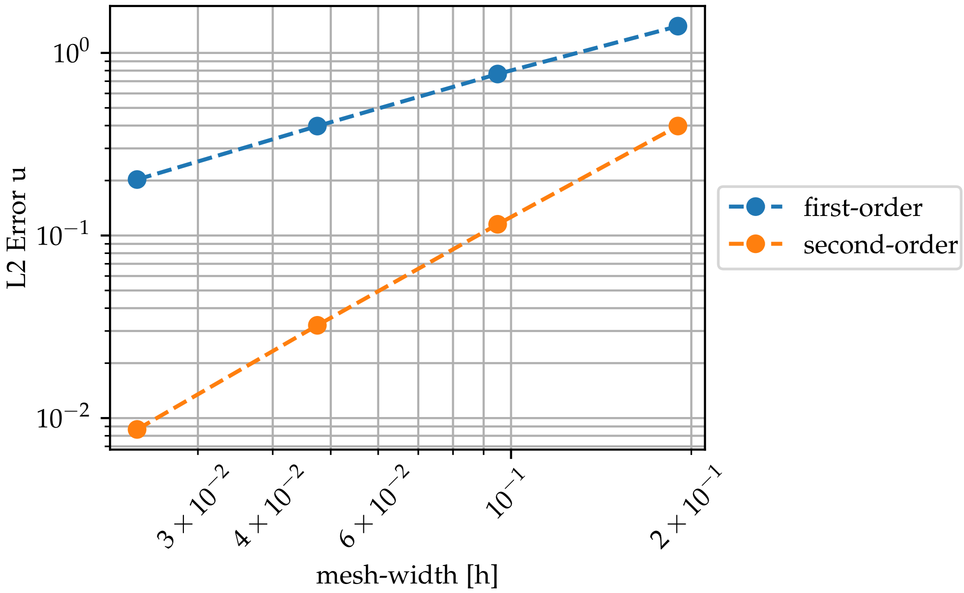

Figure 1.5: Section 1.7.1 computed until 0.4 seconds using the first- and second-order scheme as defined in section 1.5. The timestep is coupled to the mesh width using a sufficiently small CFL condition.

these faces have an angle bigger than 90 degrees with the red line, we know this is the element we need. See fig. 1.4 for illustration.

1.7 Experimental validation

In this section we present some numerical results that validate our first- and second-order scheme for advection of differential forms by means of three examples. We only consider advection ($\varepsilon = 0$) as that is the most challenging case for simulation [27]. The code used for all numerical experiments can be found at [61].

1.7.1 Vectorial rotating hump problem

This example was inspired by [27, Section 6.3]. We consider the domain $\Omega = \{x \in \mathbb{R}^2; -1 \leq x_1, x_2 \leq 1\}$ with velocity

$$\boldsymbol{\beta} = \begin{bmatrix} x_2 \\ -x_1 \end{bmatrix},$$

and source term $f = 0$. Also, we have the initial condition

$$\boldsymbol{\beta} = \begin{bmatrix} x_2 \\ -x_1 \end{bmatrix},$$

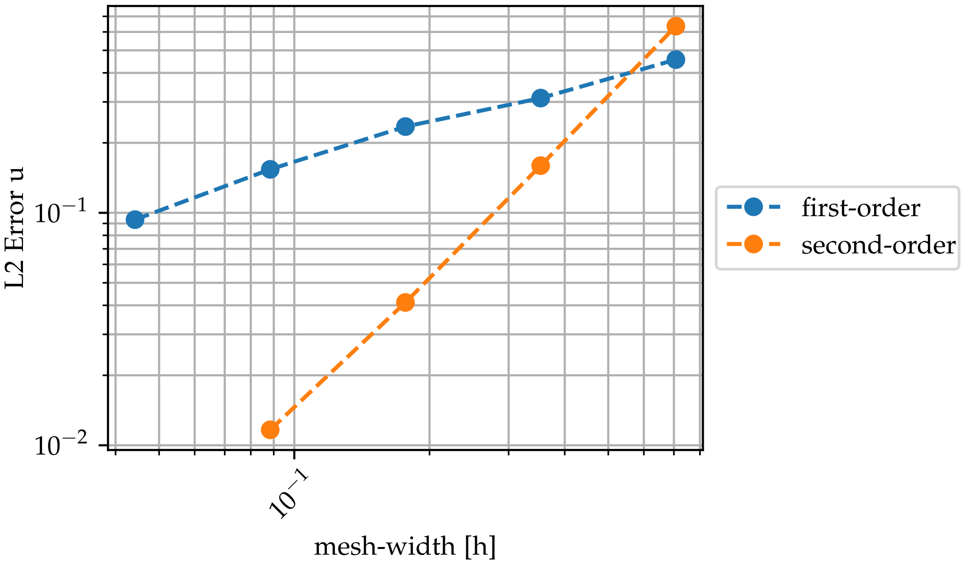

Figure 1.6: Section 1.7.2 computed until 1 second using the first- and second-order scheme as defined in section 1.5. The timestep is coupled to the mesh width using a sufficiently small CFL condition.

The vector proxy of the initial condition is given by

$$\boldsymbol{u}_0(x_1,x_2) = \begin{cases} \mathbf{grad}\, u(\boldsymbol{x}), & \text{for } \sqrt{x_1^2 + (x_2 - \frac{1}{4})^2} \leq \frac{1}{2}, \\ \mathbf{0}, & \text{else,} \end{cases}$$

where

$$u(x_1,x_2) = \cos\left(\pi\sqrt{x_1^2 + \left(x_2 - \frac{1}{4}\right)^2}\right)^4.$$

The vector proxy of the exact solution is then given by

$$\boldsymbol{u}(t,\boldsymbol{x}) = \boldsymbol{R}(t)^{-1}\boldsymbol{u}_0\left(\boldsymbol{R}(t)\boldsymbol{x}\right), \qquad \boldsymbol{R}(t) = \begin{bmatrix} \cos(t) & -\sin(t) \\ \sin(t) & \cos(t) \end{bmatrix}.$$

The results of the experiment for a simulation until a final time are given in fig. 1.5 and show a first- and second-order algebraic convergence.

1.7.2 Steady Taylor-Green vortex

We consider a Taylor-Green Vortex as introduced in [60]. We have

$$\boldsymbol{u}(\boldsymbol{x},t) = \begin{bmatrix} \cos(\pi x)\sin(\pi y)\sin(\pi z) \\ -\frac{1}{2}\sin(\pi x)\cos(\pi y)\sin(\pi z) \\ -\frac{1}{2}\sin(\pi x)\sin(\pi y)\cos(\pi z) \end{bmatrix},$$

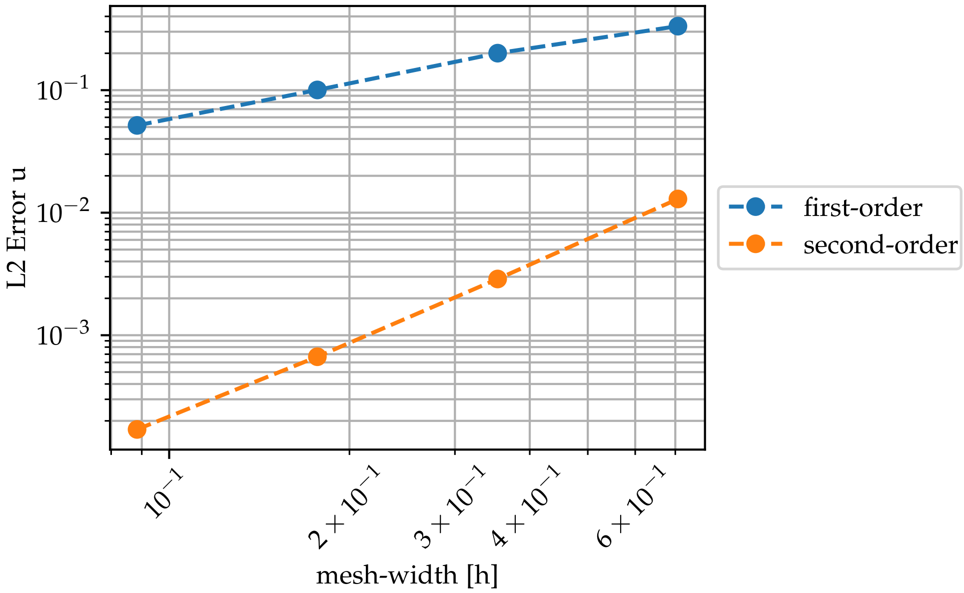

Figure 1.7: Section 1.7.3 computed until 1 second using the first- and second-order scheme as defined in section 1.5. The time step is coupled to the mesh width using a sufficiently small CFL condition.

and choose the source term and inflow boundary conditions such that this is a solution to equation (1.7) with $\varepsilon = 0$. The results of the experiment for a simulation until a final time of 1 second are given in fig. 1.6. Again, we observe first- and second-order algebraic convergence.

1.7.3 An unsteady solution in 3D

We consider

$$\boldsymbol{u}(\boldsymbol{x}, t) = \begin{bmatrix} -y\cos(\frac{1}{4}t + yz) \\ -z\cos(\frac{1}{4}t + xz) \\ -x\cos(\frac{1}{4}t + xy) \end{bmatrix},$$

and choose the source term and inflow boundary conditions such that this is a solution to equation (1.7) with $\varepsilon = 0$. The results of the experiment for a simulation until a final time of 1 second are given in fig. 1.7. Again, we observe first- and second-order algebraic convergence.

Chapter 2

Incompressible Euler Equations

2.1 Introduction

We search a solution $\boldsymbol{u}(x,t)$ and $p(x,t)$ on a bounded domain $\Omega \subset \mathbb{R}^n$ such that

$$\begin{aligned} \partial_t \boldsymbol{u} + \boldsymbol{u} \cdot \nabla \boldsymbol{u} - \varepsilon \Delta \boldsymbol{u} + \nabla p &= \boldsymbol{f}, && \text{in } \Omega, && (2.1)\\ \nabla \cdot \boldsymbol{u} &= 0, && \text{in } \Omega, && (2.2)\\ \boldsymbol{u} \cdot \boldsymbol{n} &= \boldsymbol{g} \cdot \boldsymbol{n}, && \text{on } \partial\Omega, && (2.3)\\ \boldsymbol{n} \times \nabla \times \boldsymbol{u} &= \boldsymbol{n} \times \nabla \times \boldsymbol{g}, && \text{on } \partial\Omega, && (2.4)\\ \boldsymbol{u} &= \boldsymbol{g}, && \text{on } \Gamma_{in}, && (2.5) \end{aligned}$$

where $\varepsilon > 0$ and $\boldsymbol{g} : \Omega \mapsto \mathbb{R}^n$ are given. $\partial\Omega$ and Γ_{in} denote the boundary of Ω and the influx boundary $\Gamma_{in}(t) = \{x \in \partial\Omega; \boldsymbol{g}(x,t) \cdot \boldsymbol{n}(x,t) < 0\}$. The Arnold′ interpretation [5] provides a generalization of the above set of equations to arbitrary Riemannian manifolds. In that form, it becomes clear that the system can be interpreted as an optimal transport problem over the infinite-dimensional Lie group of volume-preserving diffeomorphisms on the manifold. Through this formulation it is natural to replace the first two terms of the first equation above by the material derivative

$$D_t \boldsymbol{u} := \partial_t \boldsymbol{u} + \boldsymbol{u} \cdot \nabla \boldsymbol{u}. \tag{2.6}$$

The material derivative is equal to the derivative of the $\boldsymbol{u}$ along the velocity field and physically corresponds to the rate-of-change of the velocity of a specific particle [15]. Semi-Lagrangian schemes discretize the material derivative over the flow field to preserve this natural structure of the above set of equations.

Semi-Lagrangian schemes for the numerical solution of the incompressible Euler equations have already received some interest in literature. In [14, 64, 63], different semi-Lagrangian schemes were developed. These schemes make use of spectral/hp elements [44, 33]—a combination of finite-element and spectral methods—to obtain exponential convergence in space. The degrees of freedom lie on points in the elements, so the semi-Lagrangian approach amounts to transporting these point values using the flow map. Although these schemes provide reasonable results, the resulting discrete set of equations does not match the geometric structure of the underlying continuous equations.

Although the issue of not preserving the geometric structure of equations under discretization might not be apparent at first, it can be shown that there is a strong link between the preservation of geometric structure and the stability of the numerical schemes [4, 3]. There is a considerable amount of literature available that discuss numerical methods for the Euler equations that preserve its geometric structure [40, 22, 24, 37, 36, 66], but this literature does not include any semi-Lagrangian-type schemes. Arnold et al. [4] proposed a general framework for conserving geometric structure in the discretization of partial differential equations using the concept discrete differential forms. Heumann et al. [26, 28, 27] used this framework to develop a semi-Lagrangian scheme for scalar and vectorial advection that satisfies the geometric structure of the equations. However, these works did not discuss higher-order schemes and the incompressible Euler equations were not considered. The scheme presented in this work will fill that gap.

A class of methods similar to semi-Lagrangian methods are those termed Lagrange-Galerkin (LG) methods. LG methods transport the velocity field $\boldsymbol{u}$ back using the flow field and then multiply it with a test function and integrate over it. If these integrals can be evaluated exactly, the schemes provide unconditional stability [45, 58]. In practice it is impossible to evaluate these integrals exactly and therefore they are often approximated using high-order quadrature rules. Unfortunately, the approximate evaluation of the integrals using quadrature leads to instabilities as disccused in [49, 9, 10, 39, 59, 50, 46]. The remedy for these instabilities is often to approximately transport the mesh by only transporting the vertices using the flow map and then to linearly interpolate to obtain the locations of the other points. Then, the integrals can be evaluated exactly, since the integrand is piecewise-polynomial. However, splitting the transported mesh into smaller elements on which the integrand is polynomial, is computationally expensive in two and three dimensions. The semi-Lagrangian method as presented in this work does not suffer from this issue as, independently of the dimension of the mesh, we only need to split the domains of line-integrals, i.e. one-dimensional integrals.

In this work, we introduce a second-order, conservative, structure-preserving semi-Lagrangian scheme to solve the incompressible Euler equations in two and three dimensions on simplicial meshes. In section 2.2, we will introduce the geometric formulation of the incompressible Euler equations using the language of differential forms. This section will also discuss the conservation of energy and helicity for the incompressible Euler equations. In section 2.3, we will introduce the numerical scheme. This includes the spatial discretization using suitable higher-order discrete differential forms as discussed in [21, 51]. Also, we will show how to apply the semi-Lagrangian advection operator for discrete differential forms as introduced in [26, 28, 27] to the incompressible Euler equations and how to extend it to second-order. The resulting non-conservative scheme will be implicit, but only requires solving a symmetric, linear system at every time-step. Section 2.3 will also include a discusion on how we achieve conservation of energy and helicity using appropriate Lagrange multipliers. Section 2.4 will provide a numerical validation of the scheme.

2.2 The Euler equations and exterior calculus

In this section, we will review a famous work by Arnold [5]. The work discusses infinite-dimensional Lie Groups and their application to the incompressible Euler equations. In particular, it shows that the incompressible Euler equations can be interpreted as a minimization problem over the space of measure-preserving diffeomorphisms. In the following, we will assume sufficient regularity and we will not be particularly concerned regarding the limitations of infinite-dimensional Lie groups. For a short introduction into Lie groups and the associated notation, see appendix A.

2.2.1 Velocity field as volume-preserving diffeomorphism

As shown in [5], a solution $\boldsymbol{u}$ to the incompressible Euler equations can be associated with a measure-preserving diffeomorphism $\boldsymbol{\varphi}_t$ by means of the system

$$\begin{cases} \frac{\partial}{\partial t}\boldsymbol{\varphi}_t(x) = \boldsymbol{u}(t, \boldsymbol{\varphi}_t(x)), \\ \boldsymbol{\varphi}_0(x) = x. \end{cases} \tag{2.7}$$

It follows that for all $t \in \mathbb{R}_+$ such that the solution of the above equation exists, we must have that $\boldsymbol{\varphi}_t : \Omega \mapsto \Omega$ is a diffeomorphism. We denote $SDiff(\Omega)$ the set of measure-preserving diffeomorphisms from Ω to itself. We have Liouville's Lemma as follows.

Lemma 2 Let $\boldsymbol{\varphi}_t : \Omega \mapsto \Omega$ be defined by equation (2.7), then, for $J_t(x) = \det(D_x\boldsymbol{\varphi}_t(x))$ with $D_x\boldsymbol{\varphi}_t(x)$ the Jacobian of $\boldsymbol{\varphi}_t$, we have

$$\begin{cases} \frac{\partial J_t}{\partial t}(x) = (\nabla \cdot \boldsymbol{u})(t, \boldsymbol{\varphi}_t(x))J_t(x) \\ J_0(x) = 1. \end{cases} \tag{2.8}$$

Proof See appendix B.1 ☐

Corollary 3 Since $\boldsymbol{u}$ as a solution to the incompressible Euler equations is divergence-free, we must have $\det(D_x\boldsymbol{\varphi}_t(x)) = 1$, i.e. $\boldsymbol{\varphi}_t$ is measure-preserving.

We will consider $SDiff(\Omega)$ as an infinite-dimensional Lie Group, where map composition defines the group action. The definition of such a Lie Group is non-trivial and mostly irrelevant for the current work. We refer to [18] for an elaborate theoretical analysis.

The main result by Arnold is the following [5].

Theorem 4 (Arnold) Let $\boldsymbol{\varphi} : [0,T] \ni t \mapsto \boldsymbol{\varphi}(t,\cdot) \in SDiff(\Omega)$ be such that $\dot{\boldsymbol{\varphi}}$ is constant with respect to the L^2-norm and $\boldsymbol{\varphi}$ is a minimizer with respect to the Lagrangian

$$\int_0^T L(\boldsymbol{\varphi},\dot{\boldsymbol{\varphi}})dt := \int_0^T \frac{1}{2}\int_\Omega |\dot{\boldsymbol{\varphi}} \circ \boldsymbol{\varphi}(x)|^2 dxdt. \tag{2.9}$$

Then, the vector field $\boldsymbol{u} = \dot{\boldsymbol{\varphi}} \circ \boldsymbol{\varphi}^{-1}$ solves the incompressible Euler equation as stated in equation (2.1).

Proof The proof makes use of dynamical reduction theory. We introduce the relevant aspects of this theory in the next section. For the complete proof of Arnold's theorem using the theory introduced in the next section, see appendix B.3. ☐

2.2.2 Reduction theory

As we saw in the previous section, every velocity field $\boldsymbol{u}(x,t)$ can be associated with a C^1-curve $\boldsymbol{\varphi}_t \in SDiff(\Omega)$. A natural question that arises is whether all elements of $SDiff(\Omega)$ are required to describe the dynamics of the system. It turns out that this is not the case. According to theorem 4, the dynamics of the system are described by the Lagrangian on $SDiff(\Omega)$ for which we have

$$\begin{aligned} L(\boldsymbol{\varphi},\dot{\boldsymbol{\varphi}}) &= \frac{1}{2}\int_\Omega |\dot{\boldsymbol{\varphi}} \circ \boldsymbol{\varphi}(x)|^2 dx \\ &= \frac{1}{2}\int_\Omega |\dot{\boldsymbol{\varphi}} \circ \mathrm{Id}(x)|^2 \underbrace{|\det(D(\boldsymbol{\varphi}^{-1} \circ \mathrm{Id}))|}_{=1} dx = L(e,\dot{\boldsymbol{\varphi}}) \end{aligned} \tag{2.10}$$

for any $\boldsymbol{\varphi} \in SDiff(\Omega)$. Indeed, we can conclude that our Lagrangian is left-invariant by the following definition.

Definition 15 Let G be a Lie group. A lagrangian $L : G \times TG \mapsto \mathbb{R}$ is left-invariant if for all $g \in G$ holds

$$L(g,\dot{g}) = L(e,\dot{g}),$$

where e denotes the identity element of G.

Intuitively, this means that the only relevant information for the Lagrangian is the velocity of the fluid rather than the position. Physically this makes sense, since the behaviour of the fluid should be coordinate-independent. Mathematically, this means that instead of considering all the tangent spaces along a curve through $SDiff(\Omega)$, we can simply only consider the tangent space at the identity $T_eSDiff(\Omega)$—the Lie algebra of $SDiff(\Omega)$. This is a powerful result, since it means that we can neglect the geometry of $SDiff(\Omega)$ and only focus on the vector space structure of $T_eSDiff(\Omega)$.

There is one problem left: our Lagrangian is defined on $SDiff(\Omega)$, not on $T_eSDiff(\Omega)$. Recall that the Lagrangian is only dependent on the velocity. Suppose we have a curve in $f : [0, T] \mapsto SDiff(\Omega)$ such that $f(0) = g$, then we can identify the velocity $\dot{f}(0) \in T_gSDiff(\Omega)$ with a velocity in $T_eSDiff(\Omega)$ by simply multiplying the curve f by g^{-1}. In this way we can define a reduced Lagrangian on $T_eSDiff(\Omega)$. This was formalized for arbitrary Lie groups by Marsden [35] in the form of the following theorem.

Theorem 5 Let G be a Lie group, $\mathfrak{g}$ its Lie algebra, and let $L : G \times TG \mapsto \mathbb{R}$ be left-invariant, then we can define the reduced lagrangian $l : \mathfrak{g} \mapsto \mathbb{R}$ as

$$T_eG \cong \mathfrak{g} \ni \dot{g} \mapsto l(\dot{g}) := L(e, \dot{g}). \tag{2.11}$$

Now let $g : [0, T] \mapsto G$ be a curve in G, and define $\xi : [0, T] \mapsto T_eG \cong \mathfrak{g}$ as $\xi(t) := \frac{d}{ds}\Big|_{s=t} \{s \mapsto g^{-1}(t)g(s)\}$, then the following are equivalent.

1. The variational principle

$$\delta \int_0^T L(g(t), \dot{g}(t))dt = 0$$

holds for variations with fixed endpoints.

2. The variational principle

$$\delta \int_0^T l(\xi(t))dt = 0$$

holds on $\mathfrak{g}$, using variations of the form

$$\delta\xi = \dot{\eta} + [\xi, \eta],$$

with $\eta : [0, T] \mapsto T_eG$ and $\eta(0) = 0 = \eta(T)$.

3. The Euler-Poincaré equations hold, that is, for all $v \in T_eSDiff(\Omega)$

$$\left(\frac{d}{dt} \frac{\delta l}{\delta \xi}, v \right) = - \left(\frac{\delta l}{\delta \xi}, [\xi, v] \right),$$

where $\frac{\delta l}{\delta \xi}$ is defined such that

$$\left(\frac{\delta l}{\delta \xi}, v\right) = \left.\frac{d}{d\varepsilon}\right|_{\varepsilon=0} l(\xi + \varepsilon v)$$

is satisfied.

Proof See appendix B.2. □

In the next section, we will see how the above theorem can be used to obtain a geometric version of the incompressible Euler equations.

2.2.3 Geometric formulation of the Euler equations

Note that in the case of the incompressible Euler equations, we have for $\boldsymbol{\varphi} : [0, T] \mapsto SDiff(\Omega)$ and $\xi := \left.\frac{d}{ds}\right|_{s=0} \{s \mapsto \boldsymbol{\varphi}^{-1}(0)\boldsymbol{\varphi}(s)\}$. This yields

$$l(\xi) = \frac{1}{2}\int_\Omega |\dot{\boldsymbol{\varphi}}|^2 dx. \tag{2.12}$$

We thus find the identification

$$\frac{\partial l}{\partial \xi} = \dot{\boldsymbol{\varphi}} = \boldsymbol{u}. \tag{2.13}$$

However, on the other hand, we can apply property 3 of theorem 5. Let $\omega \in \Lambda^1(T_e SDiff(\Omega))$ be such that for all $\eta \in T_e SDiff(\Omega)$

$$\int_\Omega \omega(\eta)\mu = \left(\frac{\delta l}{\delta \xi}, \eta\right). \tag{2.14}$$

We can thus identify $\boldsymbol{u}$ with a 1-form $\omega := \boldsymbol{u}^\flat$ in the Hilbert space $L^2(\Omega)$. From (3) in theorem 5, we find

$$\int_\Omega \frac{d}{dt}\omega(\eta)dx = \int_\Omega \omega([\xi, \eta])dx. \tag{2.15}$$

For $\Omega = \mathbb{R}^d$ with $d = 2, 3$, this reduces to [40, section 2.2]

$$\int_\Omega \frac{d}{dt}\omega(\eta)dx = -\int_\Omega L_\xi \omega(\eta)dx. \tag{2.16}$$

Since we can also identify η with the 1-form $v := \eta^\flat$, we find

$$\int_\Omega \frac{d\omega}{dt} \wedge \star v + \int_\Omega L_\xi \omega \wedge \star v = 0. \tag{2.17}$$

Since ω can be identified with $\dot{\boldsymbol{\varphi}}$ with $\boldsymbol{\varphi}$ a volume-preserving diffeomorphism, we must have that the divergence of $\omega^\sharp$ vanishes, that is, $\omega^\sharp$ is incompressible.

Adding a Lagrange multiplier to enforce the incompressibility of ω reveals the pressure term. We obtain for all $v \in \Lambda^1(\Omega)$, $\psi \in \Lambda^0(\Omega)$, and $\Omega = \mathbb{R}^d$ with $d = 2, 3$

$$\int_\Omega \left[\frac{d\omega}{dt} + \int_\Omega L_\xi \omega \right] \wedge \star v + \int_\Omega \mathrm{d}p \wedge \star v = 0. \tag{2.18}$$

$$\int \omega \wedge \star \mathrm{d}\psi = 0, \tag{2.19}$$

where we left out source- and boundary-terms for simplicity. Adding the viscosity term yields

$$\int_\Omega \left[\frac{d\omega}{dt} + \int_\Omega L_\xi \omega \right] \wedge \star v + \varepsilon \int_\Omega \mathrm{d}\omega \wedge \star \mathrm{d}v + \int_\Omega \mathrm{d}p \wedge \star v = 0. \tag{2.20}$$

$$\int \omega \wedge \star \mathrm{d}\psi = 0. \tag{2.21}$$

It can be shown [16] that the inviscid, incompressible Euler equations conserve the energy

$$E(\omega) = \int_\Omega \omega \wedge \star \omega, \tag{2.22}$$

and the helicity

$$H(\omega) = \int_\Omega \mathrm{d}\omega \wedge \omega. \tag{2.23}$$

The helicity can physically be interpreted as the total amount of corkscrew movement present in the fluid. It is important that numerical schemes conserve both properties on the discrete level.

2.3 A semi-Lagrangian discretization

In this section, we will discuss a semi-Lagrangian discretization of equation (2.20). In the spirit of the semi-Lagrangian approach, we will start by discretizing the material derivative.

2.3.1 Approximation of the flow map

For the discretization of the material derivative, we proceed mostly as described in section 1.4. However, the flow is to be set equal to the velocity field $\boldsymbol{u}$ corresponding to the Euler equations. Therefore, equation (1.5) changes to

$$\frac{\partial}{\partial \tau} X_{t+\tau}(x) = \boldsymbol{u}(X_{t+\tau}(x), t), \tag{2.24a}$$

$$X_t(x) = x. \tag{2.24b}$$

As discussed in section 1.4, we are mostly interested in flow backwards in time. We can use explicit Euler to make the first-order approximation

$$X_{t-\tau}(x) = x - \tau \boldsymbol{u}(x, t) + \mathcal{O}(\tau), \tag{2.25}$$

where $\tau > 0$ denotes the timestep. In practice, we do not have access to $\boldsymbol{u}$ as it is an unknown. Instead, we will have access to an approximation of ω at each timestep. Since the 1-form ω can be identified with the velocity field $\boldsymbol{u} = \omega^\sharp$, we can identify the approximations of ω by approximate velocity fields $\ldots, \boldsymbol{u}^{n-1}, \boldsymbol{u}^n, \boldsymbol{u}^{n+1}, \ldots$ corresponding to times $\ldots, t_{n-1}, t_n, t_{n+1}, \ldots$. Note that on the level of implementation, $\boldsymbol{u}^n$ and ω^n are the same and we will thus not distinguish in the remainder of this text. Also, we will assume them to be accurate up to sufficiently high order, such that we find

$$X_{t_n - \tau}(x) = x - \tau \boldsymbol{u}^n(x) + \mathcal{O}(\tau). \tag{2.26}$$

Note that the approximation $\boldsymbol{u}^n$ resides in a space of (higher-order) discrete differential forms as discussed in section 1.3. This means that only tangential continuity across faces of elements in the mesh is guaranteed, while discontinuities may appear in the normal direction of the faces. Therefore, $\boldsymbol{u}^n$ is not point-wise defined—even though equation (2.26) requires point-wise evaluation. To solve this, we need to introduce a smoothened version of $\boldsymbol{u}^n$. There are plenty of possibilities, but we would like the smoothened version of $\boldsymbol{u}^n$ to be

- at least Lipschitz continuous to ensure existence and uniqueness,
- well-defined on every point in the mesh,
- practically computable,
- second-order accurate.

An easy-to-compute method of smoothing that comes to mind immediately, is a method where we average the values over the neighbouring cells if we are evaluating at a point that lies exactly on a vertex or face of the mesh. If we are evaluating a point that lies within the interior of an element, we can use the prolongation operator to obtain a value. However, this method does not provide a function that is in $C^0(\Omega)$, because there will still be jumps of the tangential value across faces. In practice, this can lead to instabilities.

Instead, we introduce a smoothened version of $\boldsymbol{u}^n$ as follows. Let h denote the mesh-width, $(u_i^n)_{i=1,..,d}$ the components of $\boldsymbol{u}^n$, then

$$\bar{u}_i^n(\boldsymbol{x}) = \frac{1}{h} \int_{x_i - \frac{h}{2}}^{x_i - \frac{h}{2}} u_i^n([x_1, \ldots, x_{i-1}, \xi, x_{i+1}, \ldots, x_d]^T) d\xi \tag{2.27}$$

provides a second-order, Lipschitz-continuous approximation of $\boldsymbol{u}^n$. Note that the above integral can be evaluated up to numerical accuracy using the algorithm as described in section 1.6 and provides a second-order approximation of $\boldsymbol{u}^n(\boldsymbol{x})$.

The above scheme is theoretically sound. However, in practice we do not have access to $\boldsymbol{u}^n$, but only to the approximations at the previous timesteps

$\dots, \boldsymbol{u}^{n-2}, \boldsymbol{u}^{n-1}$. Since our flow field is assumed to be bounded, a suitable first-order approximation would be to replace $\boldsymbol{u}^n$ by the constant extrapolation $\boldsymbol{u}^{n-1}$. Our final first-order approximation of $X_{t-\tau}(x)$ for x any vertex of the mesh, is then

$$\bar{X}_{t-\tau}(x) := x - \tau \bar{\boldsymbol{u}}^{n-1}(x). \tag{2.28}$$

For any point x that is not a vertex, we obtain $\bar{X}_{t-\tau}(x)$ through its barycentric coordinates with respect to the transported vertices of the corresponding element as described in section 1.4. Similarly, but using Heun's method [62] instead of explicit Euler, we find the following second-order approximations

$$X_{t-\tau}(x) = x - \frac{\tau}{2}\left[\boldsymbol{u}^n(x) + \boldsymbol{u}^{n-1}(x - \tau \boldsymbol{u}^n(x))\right] + \mathcal{O}(\tau^2), \tag{2.29}$$

$$X_{t-2\tau}(x) = x - \tau\left[\boldsymbol{u}^n(x) + \boldsymbol{u}^{n-2}(x - 2\tau \boldsymbol{u}^n(x))\right] + \mathcal{O}(\tau^2), \tag{2.30}$$

where we can replace $\boldsymbol{u}^n$ by the linear extrapolation $\boldsymbol{u}^* = 2\boldsymbol{u}^{n-1} - \boldsymbol{u}^{n-2}$ to obtain the second-order approximations for x any vertex of the mesh

$$\bar{X}_{t-\tau}(x) := x - \frac{\tau}{2}\left[\bar{\boldsymbol{u}}^*(x) + \bar{\boldsymbol{u}}^{n-1}(x - \tau \bar{\boldsymbol{u}}^*(x))\right], \tag{2.31}$$

$$\bar{X}_{t-2\tau}(x) := x - \tau\left[\bar{\boldsymbol{u}}^*(x) + \bar{\boldsymbol{u}}^{n-2}(x - 2\tau \bar{\boldsymbol{u}}^*(x))\right], \tag{2.32}$$

where we also replaced $\boldsymbol{u}^k$ by the smoothened version $\bar{\boldsymbol{u}}^k$ for $k = n-1, n-2, *$. For any point x that is not a vertex, we again obtain $\bar{X}_{t-\tau}(x)$ through its barycentric coordinates with respect to the transported vertices of the corresponding element as described in section 1.4.

2.3.2 A first- and second-order scheme

We are now ready to extend the scheme in section 1.5 to the incompressible Euler equations. For the first-order scheme, we have the following. Given $\omega^{n-1} \in \Lambda^1_{h,1}(\Omega)$, we search $p^n \in \Lambda^0_{h,1}(\Omega), \omega^n \in \Lambda^1_{h,1}(\Omega)$ such that

$$\begin{aligned}\left(\frac{1}{\tau}\left[\omega^n - \mathcal{R}\bar{X}^*_{-\tau}\mathcal{P}\omega^{n-1}\right], \eta\right)_\Omega + \varepsilon\,(\mathrm{d}\omega^n, \mathrm{d}\eta)_\Omega + (\mathrm{d}p^n, \eta)_\Omega \qquad& \\ = \varepsilon\,(\mathrm{d}\omega^n, \eta)_{\partial\Omega} + (f, \eta)_\Omega, \qquad& \forall \eta \in \Lambda^1_{h,1}(\Omega), \\ (\omega^n, \mathrm{d}\psi)_\Omega = 0, \qquad& \forall \psi \in \Lambda^0_{h,1}(\Omega),\end{aligned}$$

where $\mathcal{R}$ and $\mathcal{P}$ denote the projection and prolongation operator as defined in section 1.3. For the second-order scheme, we use second-order timestepping.

Given $\omega^{n-2}, \omega^{n-1} \in \Lambda^1_{h,2}(\Omega)$, we search $\omega^n \in \Lambda^1_{h,2}(\Omega)$ such that

$$\begin{aligned}\left(\frac{1}{2\tau}\left[3\omega^n - 4\mathcal{R}\bar{X}^*_{-\tau}\mathcal{P}\omega^{n-1} + \mathcal{R}\bar{X}^*_{-2\tau}\mathcal{P}\omega^{n-2}\right], \eta\right)_\Omega & \\ +\varepsilon\left(\mathrm{d}\omega^n, \mathrm{d}\eta\right)_\Omega + \left(\mathrm{d}p^n, \eta\right)_\Omega = \varepsilon\left(\mathrm{d}\omega^n, \eta\right)_{\partial\Omega} + \left(f, \eta\right)_\Omega, & \quad \forall \eta \in \Lambda^1_{h,2}(\Omega), \\ \left(\omega^n, \mathrm{d}\psi\right)_\Omega = 0, & \quad \forall \psi \in \Lambda^0_{h,2}(\Omega).\end{aligned}$$

Through numerical experiments, we will later see that these schemes indeed do provide first- and second-order convergence. However, there is no guarantee that the invariants of the incompressible Euler equations are preserved. Note that the schemes presented in this section only require solving a symmetric, linear system of equations at every time-step.

2.3.3 Conservation of invariants

In this section, we will show how the numerical schemes from section 2.3.2 can be adapted in such a way that the invariants are preserved on the discrete level. We will limit ourselves to the first-order scheme, but the same method can be applied to the second-order scheme. We discuss conservation of energy and conservation of helicity separately. However, these two methods can be combined to design a scheme that conserves both energy and helicity.

Conservation of energy

In order to enforce energy conservation—conservation of the L^2-norm—we add a suitable Lagrange multiplier to the discrete system proposed in section 2.3.2. Given $\omega^{n-1} \in \Lambda^1_{h,1}(\Omega)$, we search $\omega^n \in \Lambda^1_{h,1}(\Omega)$, $p^n \in \Lambda^0_{h,1}(\Omega)$, and $\mu \in \mathbb{R}$ such that

$$\begin{aligned}\left(\frac{1}{\tau}\left[\omega^n - \mathcal{R}\bar{X}^*_{-\tau}\mathcal{P}\omega^{n-1}\right], \eta\right)_\Omega & \\ + \left(\mathrm{d}p^n, \eta\right)_\Omega + \mu\left(\omega^n, \eta\right)_\Omega = \left(f, \eta\right)_\Omega, & \quad \forall \eta \in \Lambda^1_{h,1}(\Omega), \\ \left(\omega^n, \mathrm{d}\psi\right)_\Omega = 0, & \quad \forall \psi \in \Lambda^0_{h,1}(\Omega), \\ \left(\omega^n, \omega^n\right)_\Omega = \left(\omega^{n-1}, \omega^{n-1}\right)_\Omega. &\end{aligned}$$

Note that μ is necessary to add an extra degree-of-freedom to the discrete system such that we can use this freedom to enforce the conservation constraint.

Since the above system is nonlinear, it is not clear how we can obtain the value for ω^n. We propose the following fixed-point iteration. Let $\omega^n_{k-1} \in \Lambda^1_{h,1}(\Omega)$ be some given approximation of ω^n, then we want to find a new approximation $\omega^n_k \in \Lambda^1_{h,1}(\Omega)$ that is closer to ω^n. We define ω^n_k to satisfy the above system with the third equation replaced by an approximate version. We obtain this approximate version by expanding the left-hand side using a first-order Taylor approximation around ω^n_{k-1} as

$$(\omega^n, \omega^n)_\Omega \approx (\omega^n_k, \omega^n_k)_\Omega = \left(\omega^n_{k-1}, \omega^n_{k-1}\right)_\Omega + 2\left(\omega^n_{k-1}, \omega^n_k - \omega^n_{k-1}\right). \tag{2.36}$$

The system that is satisfied by ω^n_k is the following. Given $\omega^{n-1}, \omega^n_{k-1} \in \Lambda^1_{h,1}(\Omega)$, we search $\mu_k \in \mathbb{R}$, $\omega^n_k \in \Lambda^1_{h,1}(\Omega)$, $p^n_k \in \Lambda^0_{h,1}(\Omega)$ such that

$$\begin{aligned}
&\left(\frac{1}{\tau}\left[\omega^n_k - \mathcal{R}\bar{X}^*_{-\tau}\mathcal{P}\omega^{n-1}\right], \eta\right)_\Omega \\
&\qquad + (\mathrm{d}p^n_k, \eta)_\Omega + \mu_k\left(\omega^n_{k-1}, \eta\right)_\Omega = (f, \eta)_\Omega, && \forall \eta \in \Lambda^1_{h,1}(\Omega), \\
&\qquad\qquad (\omega^n_k, \mathrm{d}\psi)_\Omega = 0, && \forall \psi \in \Lambda^0_{h,1}(\Omega), \\
&\left(\omega^n_{k-1}, \omega^n_{k-1}\right)_\Omega + 2\left(\omega^n_{k-1}, \omega^n_k - \omega^n_{k-1}\right) = \left(\omega^{n-1}, \omega^{n-1}\right)_\Omega.
\end{aligned}$$

This is a symmetric, linear system that can be solved.

Conservation of helicity

In order to enforce helicity conservation, we add a suitable Lagrange multiplier to the discrete system proposed in section 2.3.2. Given $\omega^{n-1} \in \Lambda^1_{h,1}(\Omega)$, we search $\lambda \in \mathbb{R}$, $\omega^n \in \Lambda^1_{h,1}(\Omega)$ such that

$$\begin{aligned}
&\left(\frac{1}{\tau}\left[\omega^n - \mathcal{R}\bar{X}^*_{-\tau}\mathcal{P}\omega^{n-1}\right], \eta\right)_\Omega + (\mathrm{d}p^n, \eta)_\Omega \\
&\quad + \lambda(\omega^n, \mathrm{d}\eta)_\Omega + \lambda(\mathrm{d}\omega^n, \eta)_\Omega = (f, \eta)_\Omega, && \forall \eta \in \Lambda^1_{h,1}(\Omega), \\
&\qquad\qquad (\omega^n, \mathrm{d}\psi)_\Omega = 0, && \forall \psi \in \Lambda^0_{h,1}(\Omega), \\
&\qquad\qquad (\omega^n, \mathrm{d}\omega^n)_\Omega = \left(\omega^{n-1}, \mathrm{d}\omega^{n-1}\right)_\Omega.
\end{aligned}$$

Similarly as for conservation of energy, we obtain the following fixed-point iteration. At every iteration, given $\omega^{n-1}, \omega^n_{k-1} \in \Lambda^1_{h,1}(\Omega)$, we search $\lambda_k \in \mathbb{R}$,

$\omega_k^n \in \Lambda^1_{h,1}(\Omega)$, $p_k^n \in \Lambda^0_{h,1}(\Omega)$ such that

$$\begin{aligned}
&\left(\frac{1}{\tau}\left[\omega_k^n - \mathcal{R}\bar{X}^*_{-\tau}\mathcal{P}\omega^{n-1}\right], \eta\right)_\Omega + (\mathrm{d}p_k^n, \eta)_\Omega \\
&+\lambda_k(\omega_{k-1}^n, \mathrm{d}\eta)_\Omega + \lambda_k(\mathrm{d}\omega_{k-1}^n, \eta)_\Omega = (f, \eta)_\Omega, && \forall \eta \in \Lambda^1_{h,1}(\Omega), \\
&(\omega_k^n, \mathrm{d}\psi)_\Omega = 0, && \forall \psi \in \Lambda^0_{h,1}(\Omega),
\end{aligned}$$

$$\left(\omega_{k-1}^n, \mathrm{d}\omega_k^n\right)_\Omega + \left(\omega_k^n, \mathrm{d}\omega_{k-1}^n\right)_\Omega - \left(\omega_{k-1}^n, \mathrm{d}\omega_{k-1}^n\right)_\Omega = \left(\omega^{n-1}, \mathrm{d}\omega^{n-1}\right)_\Omega.$$

Again, we obtain a linear, symmetric system of equations and it is observed in practice that the fixed-point iteration converges in about three iterations.

2.4 Numerical Validation

In this section, we consider multiple numerical experiments for validation. We use the non-conservative version of our scheme unless stated otherwise. The code used for all numerical experiments can be found at [61].

2.4.1 Experiment 1: Decaying Taylor-Green Vortex

We consider the incompressible Euler equations with $\varepsilon = \pi^{-2}$, $\Omega = [-\frac{1}{2}, \frac{1}{2}]^2$, no source term, and vanishing normal boundary conditions. An exact, classical solution is the following Taylor-Green vortex [60]

$$\boldsymbol{u}(\boldsymbol{x}, t) = \begin{bmatrix} \cos(\pi x_1)\sin(\pi x_2) \\ -\sin(\pi x_1)\cos(\pi x_2) \end{bmatrix} e^{-2t}. \tag{2.40}$$

We ran a h-convergence analysis and summarize the results in fig. 2.1.

2.4.2 Experiment 2: Taylor-Green Vortex

We consider the incompressible Euler equations for different values of $\varepsilon \in \{0, 10^{-2}, 1\}$ and with vanishing boundary conditions on the domain $\Omega = [-\frac{1}{2}, \frac{1}{2}]^2$. The source term is chosen such that

$$\boldsymbol{u}(\boldsymbol{x}, t) = \begin{bmatrix} \cos(\pi x_1)\sin(\pi x_2) \\ -\sin(\pi x_1)\cos(\pi x_2) \end{bmatrix} \tag{2.41}$$

is an exact, classical solution. We ran a h-convergence analysis for all parameters and summarize the results in fig. 2.2. We observe first- and second-order algebraic convergence for the corresponding schemes. An important observation is that the scheme performs similarly for different values of ε. As $\varepsilon \to 0$ the constant of convergence remains bounded. This is in agreement with

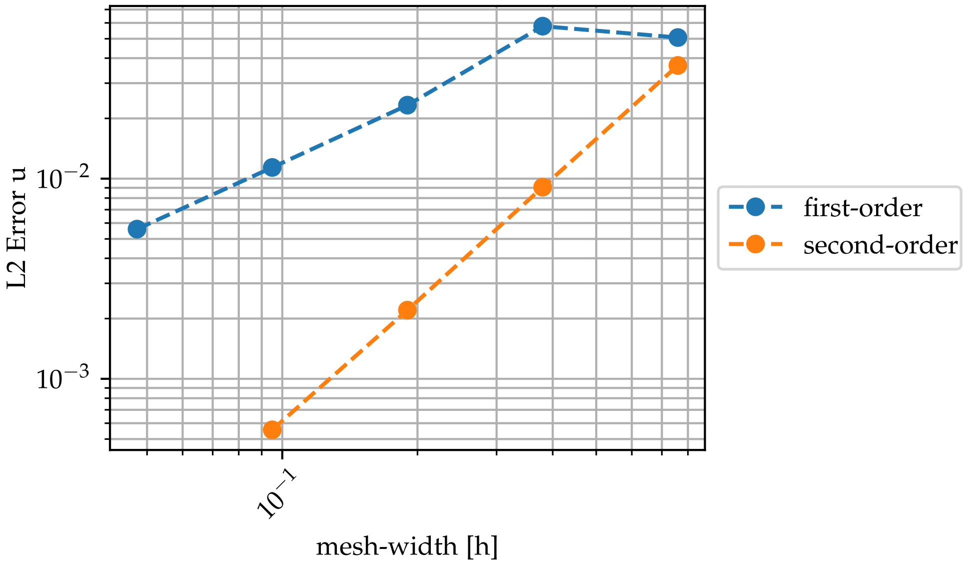

Figure 2.1: Convergence results for experiment 1 using the first- and second-order, non-conservative schemes on simplicial meshes with mesh-width h, timestep $\tau = 0.263214h$, and final time $T = 1$. We observe first- and second-order algebraic convergence.

the analysis performed on the vectorial advection equations presented in [27]. This experiment thus suggests that this analysis can be extended to the scheme presented in this work. For completeness, we also track the energy for the case $\varepsilon = 0$ in fig. 2.3.

2.4.3 Experiment 3: A rotating hump problem

The Taylor-Green vortices are interesting to observe, since they are analytical solutions. However, practical problems will often be significantly more dynamic. This experiment is meant to reflect such behaviour. We consider the incompressible Euler equations with $\varepsilon = 0$, $\Omega = [-\frac{1}{2}, \frac{1}{2}]^2$, no source term, and vanishing normal boundary conditions. We have the following initial condition

$$\boldsymbol{u}_0(\boldsymbol{x}) = \begin{bmatrix} -\pi e^{x_1}\cos(\pi x_1)\sin(\pi x_2) \\ \pi e^{x_1}\sin(\pi x_1)\cos(\pi x_2) - e^{x_1}\cos(\pi x_1)\cos(\pi x_2) \end{bmatrix}. \tag{2.42}$$

The exact solution to this problem is unknown, so we compare our solution to the solution produced by the incompressible Euler solver Gerris [48]. The algorithm used in this solver is described in [47]. We computed the solution to the problem using the second-order, conservative scheme presented in this work. Then, we plotted the magnitude of the computed velocity vector field

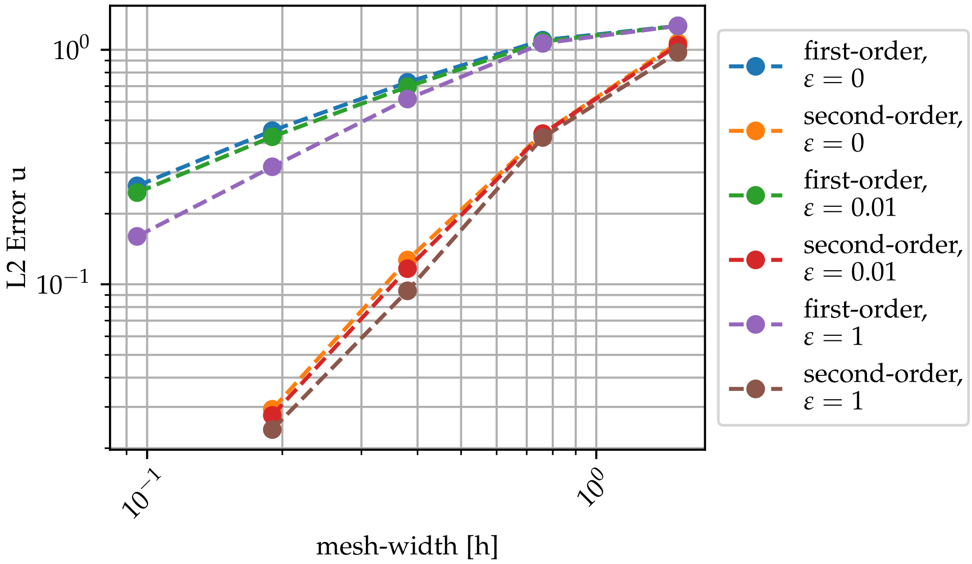

Figure 2.2: Convergence results for experiment 2 using the first- and second-order, non-conservative schemes on simplicial meshes with mesh-width h, timestep $\tau = 0.13161h$, and final time $T = 1$. As $\varepsilon \to 0$ the constant of convergence remains bounded.

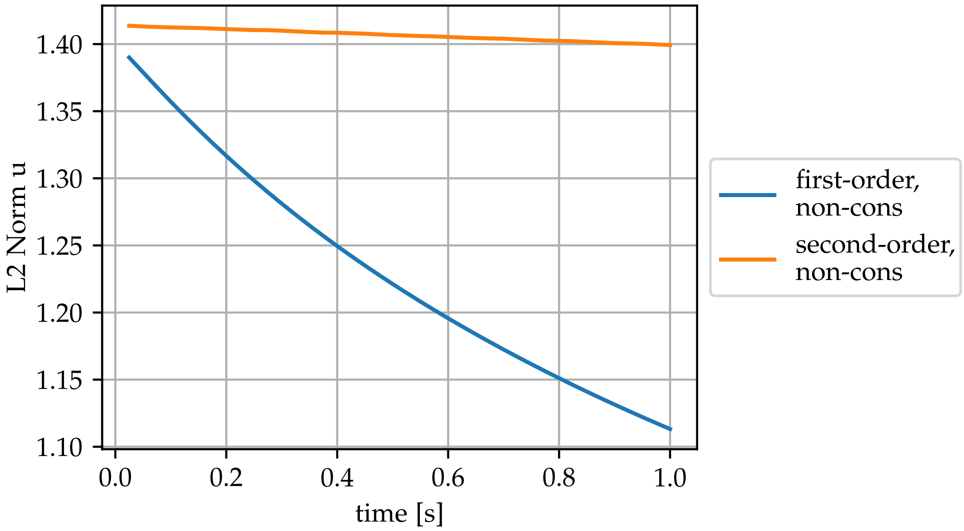

Figure 2.3: Energy of the discrete solution for experiment 2 using the first- and second-order, non-conservative schemes on a simplicial mesh with mesh-width $h = 0.189959$, timestep $\tau = 0.025$, and final time $T = 1$.

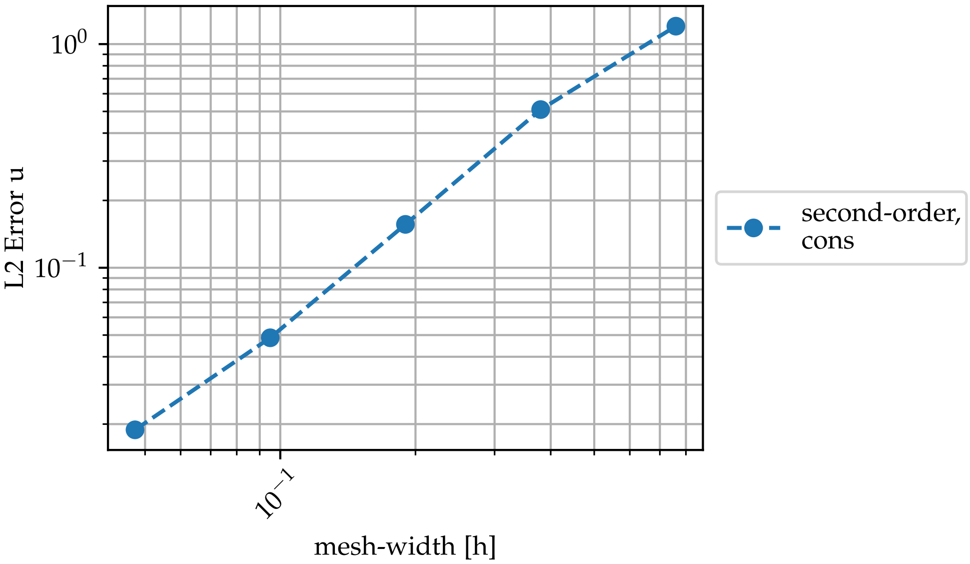

Figure 2.4: Convergence results for experiment 2 using the second-order, conservative scheme on simplicial meshes with mesh-width h, timestep $\tau = 0.06580h$, and final time $T = 1$. The reference solution is a solution computed by Gerris [47]

for different mesh-sizes and time-steps at different time instances in figs. 2.5 to 2.8. Note that different visualisation tools were used to visualize the fields computed using the different solvers, but we can see a clear correspondence between the two solvers. Also, we observe that solution computed by the semi-Lagrangian scheme comes visually closer to the solution computed by Gerris as we decrease the mesh-width. This is confirmed by fig. 2.4, where we display the L2 error between the solution computed using the semi-Lagrangian scheme and the solution computed using Gerris. In fig. 2.10, we display the vector field as computed using the second-order, conservative semi-Lagrangian scheme.

Also, in fig. 2.11 we display the values of the L2 norm over time of the solutions produced using our first- and second-, conservative and non-conservative schemes. Note that the conservative schemes preserve the L2 norm as expected. The first-order, non-conservative scheme seems unstable at first, but in reality the ordinate axis spans a very small range and it turns out that the L2 norm converges to a bounded value for longer run-times. Note that the helicity is not defined in two dimensions.

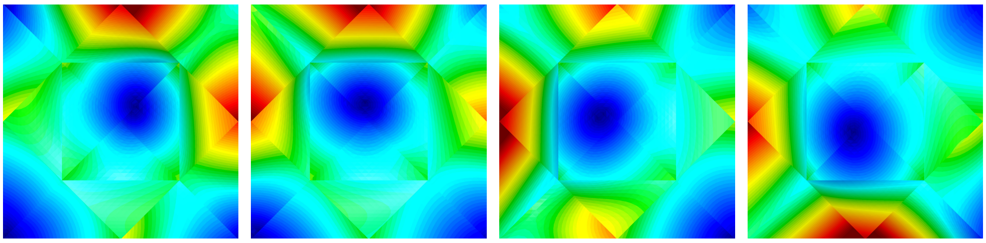

(a) $t = 0.25$ (b) $t = 0.5$ (c) $t = 0.75$ (d) $t = 1$

Figure 2.5: Experiment 3: mesh-width $h = 0.379918$ and time-step $\tau = 0.025$.

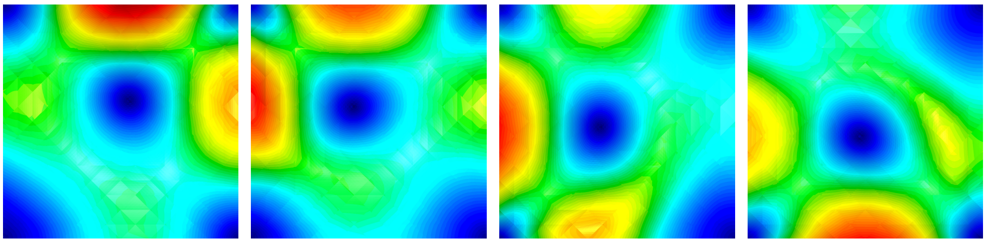

(a) $t = 0.25$ (b) $t = 0.5$ (c) $t = 0.75$ (d) $t = 1$

Figure 2.6: Experiment 3: mesh-width $h = 0.0949795$ and time-step $\tau = 0.00625$.

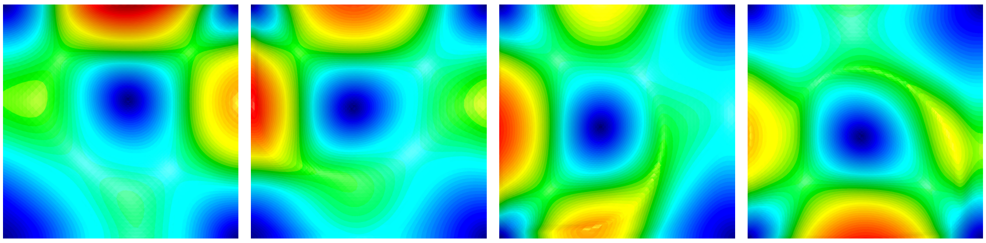

(a) $t = 0.25$ (b) $t = 0.5$ (c) $t = 0.75$ (d) $t = 1$

Figure 2.7: Experiment 3: mesh-width $h = 0.023744875$ and time-step $\tau = 0.0015625$.

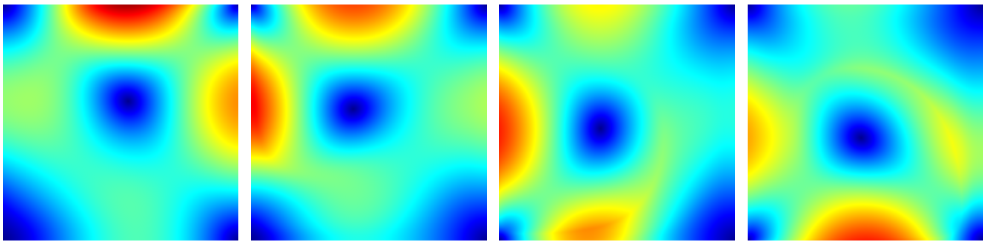

(a) $t = 0.25$ (b) $t = 0.5$ (c) $t = 0.75$ (d) $t = 1$

Figure 2.8: Reference solution experiment 3 computed using [48].

Figure 2.9: Colorbar corresponding to figs. 2.5 to 2.8

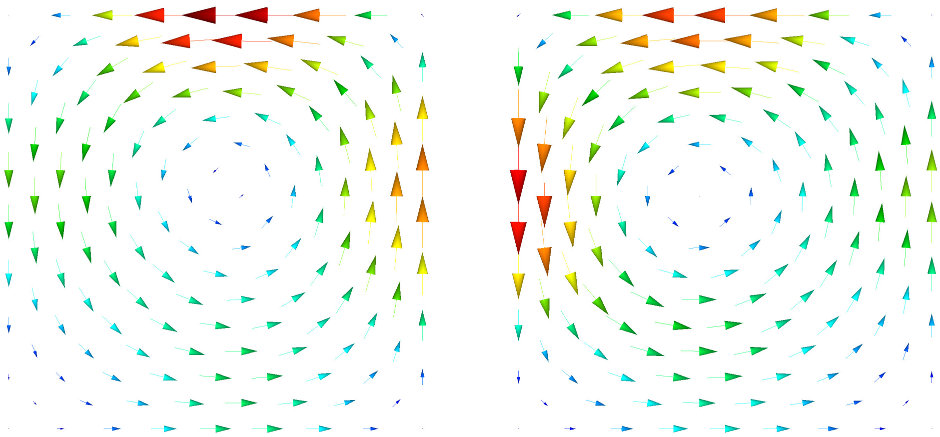

(a) $t = 0.25$ (b) $t = 0.5$

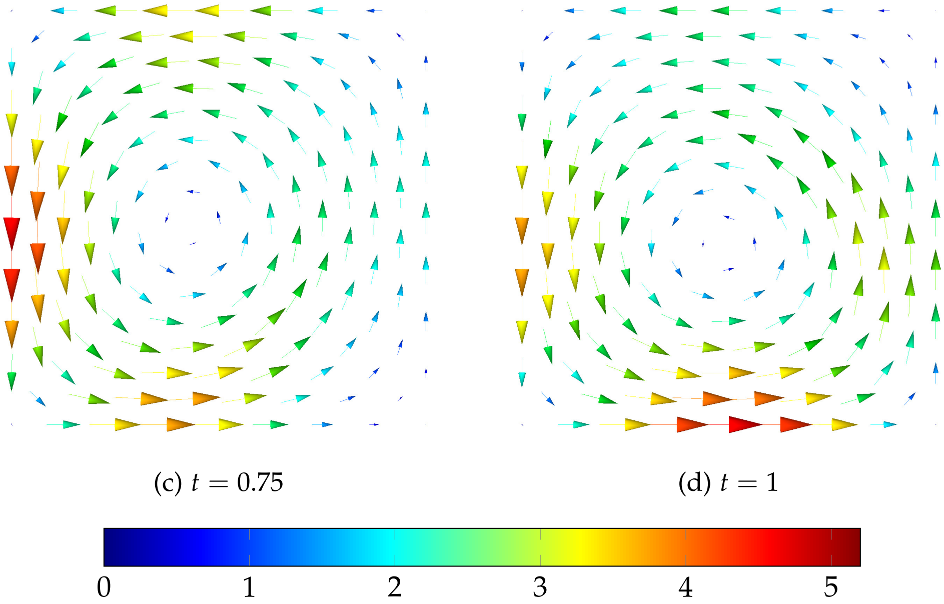

(c) $t = 0.75$ (d) $t = 1$

Figure 2.10: Velocity field for experiment 3 computed using the second-order, conservative semi-Lagrangian scheme on a simplicial mesh with mesh-width $h = 0.189959$ and time-step $\tau = 0.0125$. The colors indicate the magnitude of the vector.

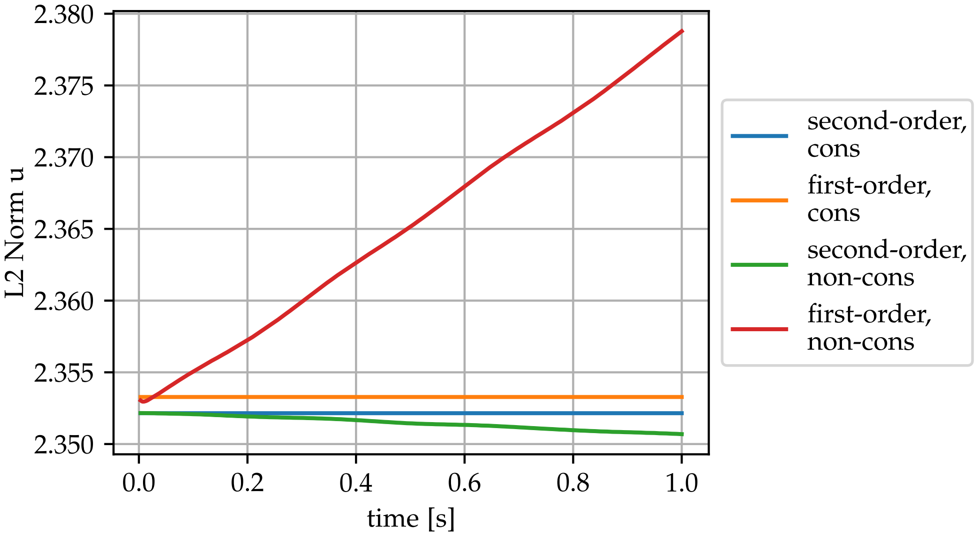

Figure 2.11: The L2 norm of the computed solutions for experiment 3 using different variants of the semi-Lagrangian scheme on a simplicial mesh with mesh-width $h = 0.04748975$ and time-step $\tau = 0.003125$. In the legend, 'cons' is short for 'conservative'.

2.4.4 Experiment 4: Taylor-Green Vortex in 3D

To observe conservation of helicity, we need to consider a problem in 3D. We consider the incompressible Euler equations with $\varepsilon = 0$ and vanishing normal boundary conditions on the domain $\Omega = [-\frac{1}{2}, \frac{1}{2}]^3$. The source term is chosen such that

$$\boldsymbol{u}(\boldsymbol{x}, t) = \begin{bmatrix} \cos(\pi x_1)\sin(\pi x_2)\sin(\pi x_3) \\ -\frac{1}{2}\sin(\pi x_1)\cos(\pi x_2)\sin(\pi x_3) \\ -\frac{1}{2}\sin(\pi x_1)\sin(\pi x_2)\cos(\pi x_3) \end{bmatrix} \tag{2.43}$$

is a solution. We run several experiments using the first- and second-order, conservative semi-Lagrangian schemes. We summarize the results in fig. 2.12 and we observe first- and second-order algebraic convergence for the corresponding schemes. In fig. 2.13 and fig. 2.14 we plot the L2 norm and helicity over time of the discrete solution for both the first- and second-order scheme. We observe that both quantities are conserved up to machine precision. Note that the range of fig. 2.14 is very small.

2.4.5 Experiment 5: A transient solution in 3D

To verify the scheme for transient solutions in 3D, we consider the incompressible Euler equations with vanishing normal boundary conditions on the

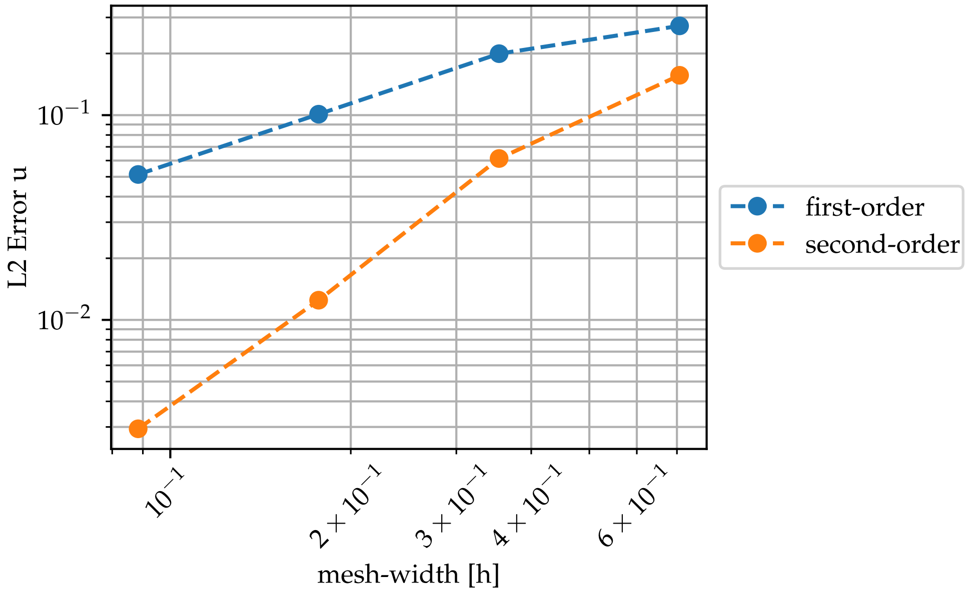

Figure 2.12: Convergence results for experiment 4 using the first- and second-order, conservative schemes on simplicial meshes with mesh-width h, timestep $\tau = \frac{1}{\sqrt{2}}h$, and final time $T = 1$.

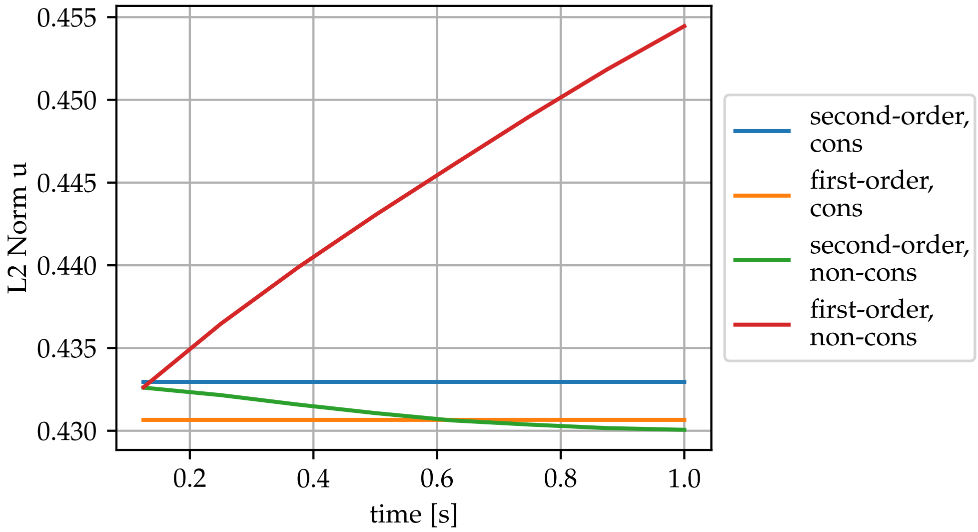

Figure 2.13: The L2 norm of the computed solutions for experiment 4 using different variants of the semi-Lagrangian scheme on a simplicial mesh with mesh-width $h = 0.08838834764$ and time-step $\tau = 0.0625$. In the legend, 'cons' is short for 'conservative'.

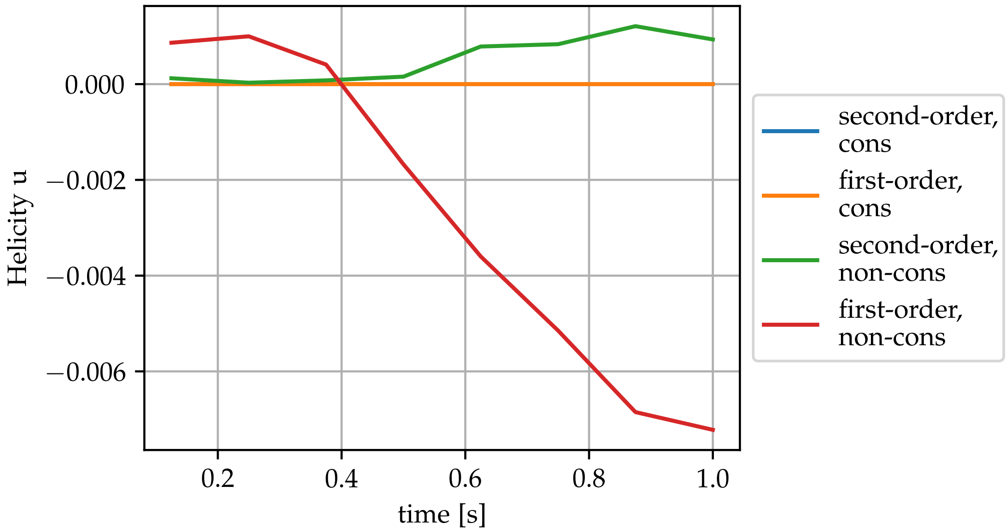

Figure 2.14: The helicity of the computed solutions for experiment 3 using different variants of the semi-Lagrangian scheme on a simplicial mesh with mesh-width $h = 0.08838834764$ and time-step $\tau = 0.0625$. In the legend, 'cons' is short for 'conservative'.

domain $\Omega = [-\frac{1}{2}, \frac{1}{2}]^3$. The source term is chosen such that

$$\boldsymbol{u}(\boldsymbol{x}, t) = \begin{bmatrix} -x_2\pi\cos(\frac{t}{4} + \pi x_2 x_3)\cos(\pi x_2) \\ -x_3\pi\cos(\frac{t}{4} + \pi x_1 x_3)\cos(\pi x_3) \\ -x_1\pi\cos(\frac{t}{4} + \pi x_1 x_2)\cos(\pi x_1) \end{bmatrix} \tag{2.44}$$

is a solution. We ran a simulation until a final time of 1 second for different mesh-sizes with time-steps determined by a suitable CFL condition. We summarize the results in fig. 2.15. We observe second-order convergence for the second-order scheme. The first-order scheme also achieves higher-order convergence than first-order, but this is expected to converge to first-order as the mesh-size gets smaller.

2.4.6 Experiment 6: Lid-driven cavity with slippery walls

In this section, we simulate a situation that resembles a lid-driven cavity problem for the incompressible Euler equations with $\varepsilon = 0$ on the domain $\Omega = [-\frac{1}{2}, \frac{1}{2}]^2$. We apply vanishing normal boundary conditions and the initial velocity field is set equal to zero. Then, to simulate a moving lid at the top, we apply the force-field $\boldsymbol{f}(\boldsymbol{x}, t) = [v(\boldsymbol{x}), 0]^T$ with

$$v(\boldsymbol{x}) = \begin{cases} \exp\left(1 - \frac{1}{1-100(0.5-x_2)^2}\right), & \text{if } 1 - 100(0.5 - x_2)^2 > 0, \\ 0, & \text{else.} \end{cases} \tag{2.45}$$

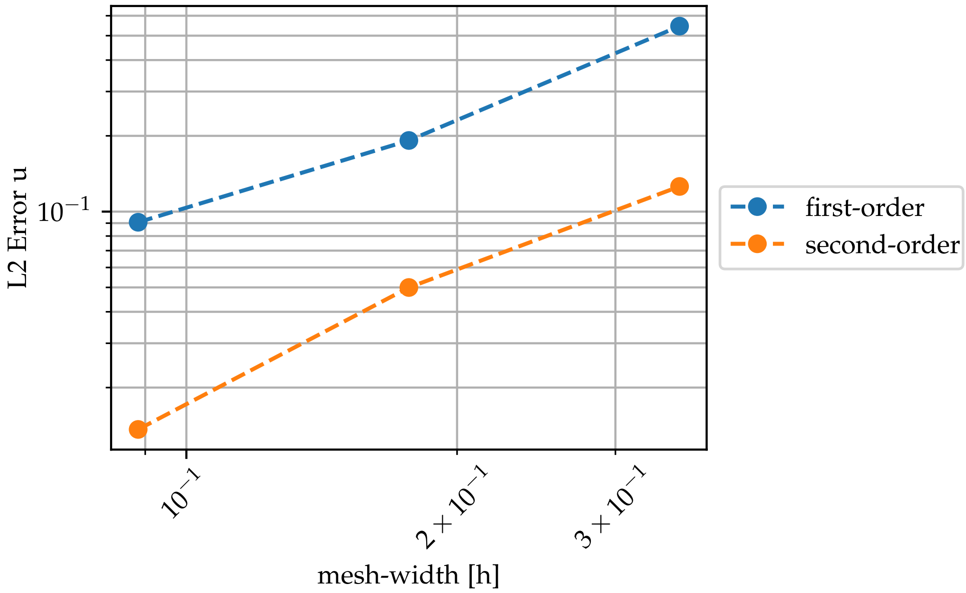

Figure 2.15: Convergence results for experiment 5 using the first- and second-order, non-conservative schemes on simplicial meshes with mesh-width h, timestep $\tau = \frac{1}{\sqrt{2}}h$, and final time $T = 1$.

This force field gives a strong force in the x_1-direction close to the top lid, but quickly tappers of to zero as we go further from the top lid. In fig. 2.16, we display the computed velocity field. Note that, because we only apply normal boundary conditions and thus no slip-related boundary conditions, we do not expect to observe vortices. The numerical solution reproduces this expectation.

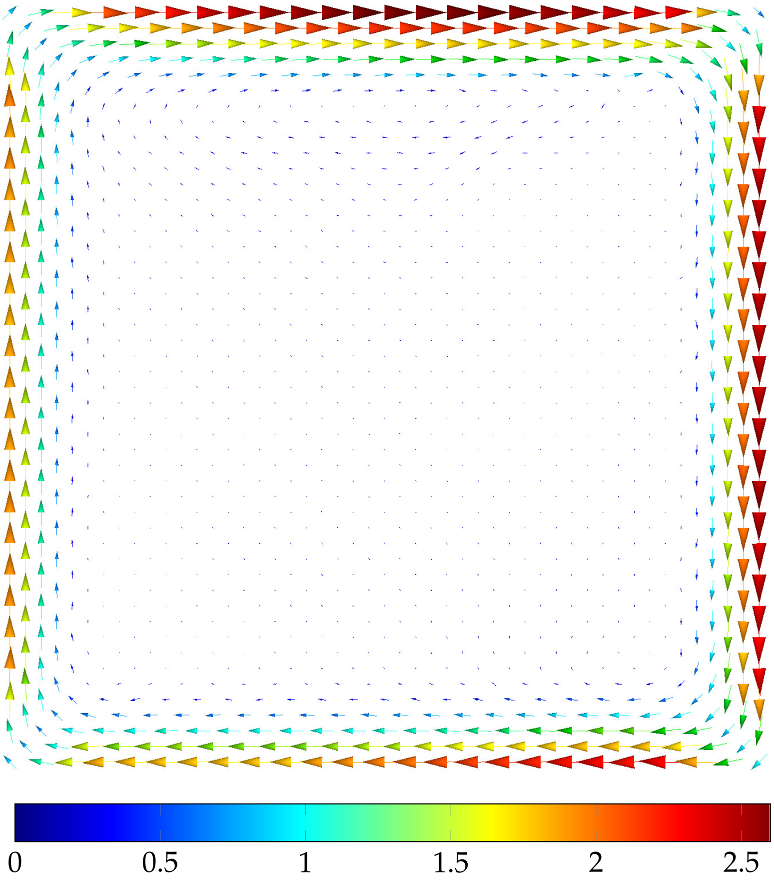

Figure 2.16: Velocity field at $T = 7.93s$ of experiment 6 computed using the second-order, non-conservative semi-Lagrangian scheme on a simplicial mesh with mesh-width $h = 0.189959$ and $\tau = 0.01$.

Chapter 3

Incompressible Magnetohydrodynamics

3.1 Introduction

We consider the magnetostatic approximation of the resistive, viscous magnetohydrodynamics (MHD) equations, that is, we are interested in finding solutions to

$$\partial_t \boldsymbol{u} + (\boldsymbol{u} \cdot \nabla)\boldsymbol{u} + \mathbf{grad}\, p - \nu \Delta \boldsymbol{u} - \kappa \boldsymbol{J} \times \boldsymbol{B} = \boldsymbol{f}, \tag{3.1a}$$

$$\partial_t \boldsymbol{B} + \mathbf{curl}\, \boldsymbol{E} = 0, \tag{3.1b}$$

$$\mathbf{curl}\, \boldsymbol{H} - \boldsymbol{J} = 0, \tag{3.1c}$$

$$\operatorname{div} \boldsymbol{u} = 0, \tag{3.1d}$$

$$\operatorname{div} \boldsymbol{B} = 0, \tag{3.1e}$$

where $\boldsymbol{u} : [0,T] \times \Omega \mapsto \mathbb{R}^n$ is the velocity field, $p : [0,T] \times \Omega \mapsto \mathbb{R}$ is the pressure, $\boldsymbol{J} : [0,T] \times \Omega \mapsto \mathbb{R}^n$ is the current, $\boldsymbol{B} : [0,T] \times \Omega \mapsto \mathbb{R}^n$ is the magnetic induction, $\boldsymbol{H} : [0,T] \times \Omega \mapsto \mathbb{R}^n$ is the magnetic field, $\boldsymbol{f} : [0,T] \times \Omega \mapsto \mathbb{R}^n$ is an external force stirring the fluid, $\nu \in \mathbb{R}$ is the fluid viscosity, and $\kappa \in \mathbb{R}$ is the magnetic coupling factor. We will apply appropriate boundary conditions later. Additionally, we have the following two material laws

$$\boldsymbol{B} = \mu \boldsymbol{H}, \tag{3.2a}$$

$$\boldsymbol{J} = \sigma(\boldsymbol{E} + \boldsymbol{u} \times \boldsymbol{B}), \tag{3.2b}$$

where $\mu \in \mathbb{R}$ is the magnetic permeability and $\sigma \in \mathbb{R}$ the electric conductivity —both assumed constant in space and time. If we take $\nu \to 0$ and $\sigma \to \infty$, we obtain the ideal MHD equations. For ease of notation, we will assume $\mu = 1$ in the remainder of this text. In [11], several modeling applications of the incompressible MHD equations are mentioned including aluminum electrolysis, electromagnetic pumping, and the MHD generator. Typical values for ν and σ are given to be around 10^{-4} and 1 for these applications.

The steady, incompressible MHD equations have received considerable attention in literature. In [23, 19, 55] several stabilized and mixed finite-element schemes have been proposed for the steady, incompressible MHD equations. Of particular interest is the scheme presented in [55]. In this work, Schötzau et al. proposed a scheme that discretizes $\boldsymbol{u}$ with $\boldsymbol{H}^1(\Omega)$-conforming finite-elements and $\boldsymbol{B}$ with $\boldsymbol{H}(\mathbf{curl}, \Omega)$-conforming finite-elements. This scheme yields an approximation of the magnetic induction $\boldsymbol{B}_h$ that is only weakly divergence-free. This means that $\boldsymbol{B}_h$ is orthogonal to all discrete gradient fields.

In recent years, the importance of satisfying the divergence-free condition for $\boldsymbol{B}$ on the discrete level has received increased interest for the development of codes for the simulation of fusion reactors [2, 1]. In [12] it is shown that when the divergence-free condition for $\boldsymbol{B}_h$ is not exactly satisfied, a non-physical force can lead to large numerical errors. An overview of the different methods that can be used to enforce the divergence-free condition for the magnetic field, can be found in [31]. Other works that cover this particular issue include [67, 65, 42, 43]. In [29], a scheme was proposed using the formulation of the incompressible MHD equations based on the magnetic vector potential $\boldsymbol{A}$ with $\boldsymbol{B} = \mathbf{curl}\, \boldsymbol{A}$. In this scheme, a discrete version of the magnetic vector potential $\boldsymbol{A}_h$ is constructed using $\boldsymbol{H}(\mathbf{curl}, \Omega)$-conforming finite-elements. Through the theory of discrete differential forms [4, 3], it then naturally follows that the discrete magnetic field $\boldsymbol{B}_h = \mathbf{curl}\, \boldsymbol{A}_h$ is divergence-free. In this work, we will follow a similar approach.

In section 3.2, we will see that $\boldsymbol{A}$ can be interpreted as the solution of an advection equation with respect to the flow field $\boldsymbol{u}$. This allows us to apply the theory of advection of discrete differential forms as proposed in [27, 26, 28] and extended to second-order in chapter 1 of this work. Also the incompressible Navier-Stokes equation can be solved using semi-Lagrangian-type methods as described in chapter 2 of this work. We will combine these methods into a semi-Lagrangian scheme for the incompressible MHD equations. We refer to chapter 1 and chapter 2 for a literature overview of semi-Lagrangian methods for the incompressible Navier-Stokes equation and advection-diffusion equations.

This work is organized as follows. In section 3.2, we introduce an alternative form of the incompressible MHD equations based on the magnetic vector potential. Then, in section 3.3 we introduce the main numerical scheme (scheme A) and slight variations to it (partial scheme B, C, etc.). In section 3.4, we provide numerical experiments for the validation of our method. We observe that the scheme works well for sufficiently low conductivity or sufficiently low viscosity, but shows instabilities for the limit case of high conductivity and low viscosity.

3.2 Introduction to the MHD equations

In this section, we will derive two alternative formulations of the incompressilbe MHD equations that both yield slightly different schemes. First, let us introduce the magnetic vector potential as $\boldsymbol{A} : [0, T] \times \Omega \mapsto \mathbb{R}^n$ with $\boldsymbol{B} = \mathbf{curl}\, \boldsymbol{A}$. Then, we can reformulate the above system of equations as

$$\begin{aligned} \partial_t \boldsymbol{u} + (\boldsymbol{u} \cdot \nabla)\boldsymbol{u} + \mathbf{grad}\, p - \nu \Delta \boldsymbol{u} - \kappa \mathbf{curl}\,\mathbf{curl}\, \boldsymbol{A} \times \mathbf{curl}\, \boldsymbol{A} &= \boldsymbol{f}, && (3.3a)\\ \mathbf{curl}\left(\partial_t \boldsymbol{A} + \frac{1}{\sigma}\mathbf{curl}\,\mathbf{curl}\, \boldsymbol{A} - \boldsymbol{u} \times \mathbf{curl}\, \boldsymbol{A}\right) &= 0, && (3.3b)\\ \mathbf{curl}\,\mathbf{curl}\, \boldsymbol{A} - \boldsymbol{J} &= 0, && (3.3c)\\ \operatorname{div} \boldsymbol{u} &= 0. && (3.3d) \end{aligned}$$

Since the curl of the gradient vanishes, we can write the second equation as

$$\mathbf{curl}\left(\partial_t \boldsymbol{A} + \frac{1}{\sigma}\mathbf{curl}\,\mathbf{curl}\, \boldsymbol{A} - \boldsymbol{u} \times \mathbf{curl}\, \boldsymbol{A} + \mathbf{grad}(\boldsymbol{A} \cdot \boldsymbol{u}) + \mathbf{grad}\, \psi\right) = 0, \quad (3.4)$$

where $\psi : [0, T] \times \Omega \mapsto \mathbb{R}$ is an arbitrary function. Considering $\boldsymbol{A}$ as the vector-proxy of a 1-form and fixing the gauge, we find

$$\begin{aligned} \partial_t \boldsymbol{A} + L_{\boldsymbol{u}} \boldsymbol{A} + \frac{1}{\sigma}\mathbf{curl}\,\mathbf{curl}\, \boldsymbol{A} + \mathbf{grad}\, \psi &= 0, && (3.5)\\ \operatorname{div} \boldsymbol{A} &= 0. && (3.6) \end{aligned}$$

Similarly, we can regard $\boldsymbol{u}$ as the vector-proxy of a 1-form (as explained in chapter 2) to obtain the following

$$\begin{aligned} \partial_t \boldsymbol{u} + L_{\boldsymbol{u}} \boldsymbol{u} + \mathbf{grad}\, p + \nu\, \mathbf{curl}\,\mathbf{curl}\, \boldsymbol{u} - \kappa \boldsymbol{J} \times \mathbf{curl}\, \boldsymbol{A} &= \boldsymbol{f}, && (3.7a)\\ \partial_t \boldsymbol{A} + L_{\boldsymbol{u}} \boldsymbol{A} + \mathbf{grad}\, \psi + \frac{1}{\sigma}\mathbf{curl}\,\mathbf{curl}\, \boldsymbol{A} &= 0, && (3.7b)\\ \mathbf{curl}\,\mathbf{curl}\, \boldsymbol{A} - \boldsymbol{J} &= 0, && (3.7c)\\ \operatorname{div} \boldsymbol{u} &= 0, && (3.7d)\\ \operatorname{div} \boldsymbol{A} &= 0. && (3.7e) \end{aligned}$$

We obtain a weak formulation by multiplying with a suitable vector proxy of a 1-form and integrating by parts. We search $\boldsymbol{u}, \boldsymbol{A}, \boldsymbol{J} \in \Lambda^1(\Omega)$ and $p, \psi \in \Lambda^0(\Omega)$

such that, for all $\boldsymbol{u}', \boldsymbol{A}' \in \Lambda^1(\Omega)$ and $p', \psi' \in \Lambda^0(\Omega)$, we have

$$\begin{aligned}\int_\Omega (\partial_t \boldsymbol{u} + L_{\boldsymbol{u}}\boldsymbol{u}) \cdot \boldsymbol{u}' dx dx + \int_\Omega \nu \,\mathbf{curl}\, \boldsymbol{u} \cdot \mathbf{curl}\, \boldsymbol{u}' dx \\ + \int_\Omega \mathbf{grad}\, p \cdot \boldsymbol{u}' dx - \kappa \int_\Omega \boldsymbol{J} \times \mathbf{curl}\, \boldsymbol{A} \cdot \boldsymbol{u}' dx = \int_\Omega \boldsymbol{f} \cdot \boldsymbol{u}' dx,\end{aligned} \tag{3.8a}$$

$$\begin{aligned}\int_\Omega (\partial_t \boldsymbol{A} + L_{\boldsymbol{u}}\boldsymbol{A}) \cdot \boldsymbol{A}' dx + \int_\Omega \mathbf{grad}\, \psi \cdot \boldsymbol{A}' dx \\ + \frac{1}{\sigma} \int_\Omega \mathbf{curl}\, \boldsymbol{A} \cdot \mathbf{curl}\, \boldsymbol{A}' dx = 0,\end{aligned} \tag{3.8b}$$

$$\int_\Omega \mathbf{curl}\, \boldsymbol{A} \cdot \mathbf{curl}\, \boldsymbol{J}' dx - \int_\Omega \boldsymbol{J} \cdot \boldsymbol{J}' dx = 0, \tag{3.8c}$$

$$\int_\Omega \boldsymbol{u} \cdot \mathbf{grad}\, p' dx = 0, \tag{3.8d}$$

$$\int_\Omega \boldsymbol{A} \cdot \mathbf{grad}\, \psi' dx = 0, \tag{3.8e}$$

where we assumed the following boundary conditions for simplicity

$$\boldsymbol{u} \cdot \boldsymbol{n} = 0, \quad \text{on } \partial\Omega, \tag{3.9}$$
$$\boldsymbol{A} \cdot \boldsymbol{n} = 0, \quad \text{on } \partial\Omega, \tag{3.10}$$
$$\boldsymbol{n} \times \mathbf{curl}\, \boldsymbol{u} = \mathbf{0}, \quad \text{on } \partial\Omega, \tag{3.11}$$
$$\boldsymbol{n} \times \mathbf{curl}\, \boldsymbol{u} = \mathbf{0}, \quad \text{on } \partial\Omega. \tag{3.12}$$

We identify the following material derivatives

$$D_t \boldsymbol{u} := \partial_t \boldsymbol{u} + L_{\boldsymbol{u}} \boldsymbol{u}, \tag{3.13}$$
$$D_t \boldsymbol{A} := \partial_t \boldsymbol{A} + L_{\boldsymbol{u}} \boldsymbol{A}. \tag{3.14}$$

Note that the material derivative of $\boldsymbol{A}$ is the derivative with respect to the flow field $\boldsymbol{u}$.

3.3 Numerical scheme

In this section, we will describe the proposed numerical schemes for solving the incompressible MHD equations. We will denote these schemes by the letters A, B, C, etc. Note that A is the most important scheme as that is the scheme we study. Partial scheme B, C, etc are merely there to provide a rigorous experimental analysis of why scheme A shows instabilities.

3.3.1 Scheme A

Our starting point will be the weak formulation of the MHD equations as presented in equation (3.15). Following the same philosophy as in section 2.3, we discretize the material derivative. Given $\boldsymbol{u}_h^{n-1}, \boldsymbol{u}_h^{n-2}, \boldsymbol{A}_h^{n-1}, \boldsymbol{A}_h^{n-2} \in \Lambda_h^1(\Omega)$, we search $\boldsymbol{u}_h^n, \boldsymbol{A}_h^n, \boldsymbol{J}_h^n \in \Lambda_h^1(\Omega)$ and $p_h^n, \psi_h^n \in \Lambda_h^0(\Omega)$ such that

$$\begin{aligned}\int_\Omega \frac{1}{2\tau}\left[3\boldsymbol{u}_h^n - 4\mathcal{R}\bar{X}_{-\tau}^*\mathcal{P}\boldsymbol{u}_h^{n-1} + \mathcal{R}\bar{X}_{-2\tau}^*\mathcal{P}\boldsymbol{u}_h^{n-2}\right] \cdot \boldsymbol{u}_h' dx dx \\ + \int_\Omega \nu\, \mathbf{curl}\, \boldsymbol{u}_h^n \cdot \mathbf{curl}\, \boldsymbol{u}_h' dx + \int_\Omega \mathbf{grad}\, p_h^n \cdot \boldsymbol{u}_h' dx \\ -\kappa \int_\Omega \boldsymbol{J}_h^n \times \mathbf{curl}\, \boldsymbol{A}_h^n \cdot \boldsymbol{u}_h' dx = \int_\Omega \boldsymbol{f} \cdot \boldsymbol{u}_h' dx,\end{aligned} \tag{3.15a}$$

$$\begin{aligned}\int_\Omega \left[3\boldsymbol{A}_h^n - 4\mathcal{R}\bar{X}_{-\tau}^*\mathcal{P}\boldsymbol{A}_h^{n-1} + \mathcal{R}\bar{X}_{-2\tau}^*\mathcal{P}\boldsymbol{A}_h^{n-2}\right] \cdot \boldsymbol{A}_h' dx \\ + \int_\Omega \mathbf{grad}\, \psi_h^n \cdot \boldsymbol{A}_h' dx + \frac{1}{\sigma}\int_\Omega \mathbf{curl}\, \boldsymbol{A}_h^n \cdot \mathbf{curl}\, \boldsymbol{A}_h' dx = 0,\end{aligned} \tag{3.15b}$$

$$\int_\Omega \mathbf{curl}\, \boldsymbol{A}_h^n \cdot \mathbf{curl}\, \boldsymbol{J}_h' dx - \int_\Omega \boldsymbol{J}_h^n \cdot \boldsymbol{J}_h' dx = 0, \tag{3.15c}$$

$$\int_\Omega \boldsymbol{u}_h^n \cdot \mathbf{grad}\, p_h' dx = 0, \tag{3.15d}$$

$$\int_\Omega \boldsymbol{A}_h^n \cdot \mathbf{grad}\, \psi_h' dx = 0, \tag{3.15e}$$

for all $\boldsymbol{u}_h', \boldsymbol{A}_h' \in \Lambda_h^1(\Omega)$ and $p_h', \psi_h' \in \Lambda^0(\Omega)$. Note that we left out the boundary terms for simplicity and $\tau > 0$ denotes the time-step size. Since $D_t\boldsymbol{u}$ and $D_t\boldsymbol{A}$ denote material derivatives with respect to the flow $\boldsymbol{u}$, X_τ denotes the transport map with respect to the flow $\boldsymbol{u}$ defined through system (2.24). As described in section 2.3.1, the operator $\mathcal{R}\bar{X}_{-\tau}^*\mathcal{P}$ only depends on $\boldsymbol{u}^{n-1}$ and $\boldsymbol{u}^{n-2}$. Therefore, the above system decouples—we first solve for $\boldsymbol{A}_h^n$ and ψ_h^n, then $\boldsymbol{J}_h^n$, and finally for $\boldsymbol{u}_h^n$ and p_h^n. This avoids the need to solve one large linear system of equations, but requires solving three smaller linear systems of equations. In the following, we will introduce some schemes that are simplifications of the above scheme. These schemes cannot be applied in practice, because they assume knowledge of some of the unknowns. However, they can be of great help when analyzing the reasons for instability of the above scheme in some cases.

3.3.2 Partial scheme B

In this scheme we remove the effect of the solution $\boldsymbol{A}_h^n$ on the computation of $\boldsymbol{J}_h^n$ such that we can see if the observed instabilities are inherent to the discrete Lorentz force. To be precise, we consider equation (3.15c)

$$\int_\Omega \mathbf{curl}\, \boldsymbol{A}_h^n \cdot \mathbf{curl}\, \boldsymbol{J}_h' dx - \int_\Omega \boldsymbol{J}_h^n \cdot \boldsymbol{J}_h' dx = 0 \tag{3.16}$$

and replace it by

$$\int_\Omega \mathbf{curl}\, \mathcal{R}A(t_n,\cdot) \cdot \mathbf{curl}\, \boldsymbol{J}_h' dx - \int_\Omega \boldsymbol{J}_h^n \cdot \boldsymbol{J}_h' dx = 0 \tag{3.17}$$

where $\mathcal{R}A(t_n,\cdot)$ is the projection of $\boldsymbol{A}$ at time t_n onto the space of second-order, discrete differential forms $\Lambda^1_{h,2}(\Omega)$. The rest of scheme A remains unchanged.

3.3.3 Partial scheme C

In this scheme, we replace the fully-discrete computation of the Lorentz force term in scheme A by a semi-discrete computation, that is, we replace

$$\int_\Omega \boldsymbol{J}_h^n \times \mathbf{curl}\, \boldsymbol{A}_h^n \cdot \boldsymbol{u}_h' dx$$

by

$$\int_\Omega \boldsymbol{J}_h^n \times \mathbf{curl}[\mathcal{R}\boldsymbol{A}(t_n,\cdot)] \cdot \boldsymbol{u}_h' dx.$$

The rest of the scheme is the same as scheme A.

3.3.4 Partial scheme E

Recall that the operator $\bar{X}^*_{-\tau}$ is based on the following evaluation of Heun's method as introduced in (2.29)

$$X_{t-\tau}(x) = x - \frac{\tau}{2}\left[\boldsymbol{u}^n(x) + \boldsymbol{u}^{n-1}(x - \tau \boldsymbol{u}^n(x))\right] + \mathcal{O}(\tau^2). \tag{3.18}$$

For partial scheme E, we will replace $\boldsymbol{u}^n$ by $\bar{u}(t_n,\cdot)$ and thus evaluate

$$X_{t-\tau}(x) = x - \frac{\tau}{2}\left[\boldsymbol{u}(t_n,x) + \boldsymbol{u}(t_{n-1}, x - \tau \boldsymbol{u}(t_n,x))\right] + \mathcal{O}(\tau^2). \tag{3.19}$$

The remainder of scheme A is not changed.

3.4 Numerical results

In this section, we evaluate the performance of the numerical schemes. Using scheme A we observe instabilities in the case that the conductivity is high and the viscosity is low, i.e. in the ideal MHD limit. If either the conductivity is low or the viscosity is high, we observe convergence of the numerical scheme. To show this, we did elaborate numerical tests inspired by [29]. The code used for all numerical experiments can be found at [61].

3.4.1 Approximation of the Lorentz force

In this section, we evaluate the computation of the Lorentz force based on some given approximation of the magnetic vector potential $\boldsymbol{A_h} \in \Lambda^1_h(\Omega)$. We project

$$\boldsymbol{A}(\boldsymbol{x}) = \begin{bmatrix} 0 \\ \sin(x) \\ 0 \end{bmatrix} \tag{3.20}$$

onto $\Lambda^1_{h,p}(\Omega)$ with $p = 1, 2$ and denote the projection as $\boldsymbol{A}_h := \mathcal{R}\boldsymbol{A}$. Next, we compute $\boldsymbol{J}_h$ analogously to scheme A, that is, we find $\boldsymbol{J}_h \in \Lambda^1_{h,p}(\Omega)$ such that for all $\boldsymbol{\eta}_h \in \Lambda^1_{h,p}(\Omega)$

$$\int_\Omega \boldsymbol{J}_h \cdot \boldsymbol{\eta}_h dx = \int_\Omega \mathbf{curl}\, \boldsymbol{A}_h \cdot \mathbf{curl}\, \boldsymbol{\eta}_h dx. \tag{3.21}$$

Then, we compute the Lorentz force $\boldsymbol{F}_h \in \Lambda^1_{h,p}(\Omega)$ as

$$\int_\Omega \boldsymbol{F}_h \cdot \boldsymbol{\eta}_h dx = \int_\Omega \boldsymbol{J}_h \times \mathbf{curl}\, \boldsymbol{A}_h \cdot \boldsymbol{\eta}_h dx. \tag{3.22}$$

We compute the L^2-error of $\boldsymbol{J}_h$ and $\boldsymbol{F}_h$ compared with their exact solutions. In table 3.2 and table 3.1 the computed errors are displayed for different mesh-sizes. We observe no convergence for first-order discrete differential forms and first-order convergence for second-order discrete differential forms. For this reason, we only consider a second-order scheme in this work.

3.4.2 Experiment 1

In this section, we consider the following problem inspired by [29]. We fix the magnetic coupling factor $\kappa = 1$, but vary the viscosity ν and conductivity σ. We choose the source terms and boundary conditions such that

$$\boldsymbol{u}(t, \boldsymbol{x}) = \begin{bmatrix} 0 \\ \sin(t)\sin(x_2) \\ 0 \end{bmatrix} \tag{3.23}$$

Mesh-width	L^2-error J_h	L^2-error $J_h \times \textbf{curl}\, A_h$
0.707107	0.0846115	0.0348872
0.353553	0.0391167	0.0139575
0.176777	0.0183738	0.00656131
0.0883883	0.00873568	0.00314751

Table 3.1: Experiment to evaluate the accuracy of computing the Lorentz force as described in section 3.4.1 using second-order discrete differential forms in $\Lambda^1_{h,2}(\Omega)$.

Mesh-width	L^2-error J_h	L^2-error $J_h \times \textbf{curl}\, A_h$
0.707107	0.104125	0.202954
0.353553	0.105169	0.102365
0.176777	0.114354	0.0566125
0.0883883	0.120679	0.0392805
0.0441942	0.128613	0.0347103
0.0220971	0.133755	0.0340028

Table 3.2: Experiment to evaluate the accuracy of computing the Lorentz force as described in section 3.4.1 using first-order discrete differential forms in $\Lambda^1_{h,1}(\Omega)$.

and

$$\boldsymbol{A}(t,\boldsymbol{x}) = \begin{bmatrix} 0 \\ \sin(t + x_1) \\ 0 \end{bmatrix} \tag{3.24}$$

are solutions to the incompressible MHD equations. We run all the experiments on the domain $\Omega = [-\frac{1}{2}, \frac{1}{2}]^3$ and untill time $T = 0.4$. The experiments presented in figs. 3.1 and C.4 show that the scheme converges if either the viscosity is high enough or the conductivity is low enough, but does not work if the viscosity is low and the conductivity is high. In other words, scheme A does not converge if we consider the case of ideal MHD. The results suggest that the scheme becomes unstable and we will see in experiment 3 that this is indeed the case.

Through the experiments on partial scheme E as summarized in figs. 3.4 and C.1, we observe that the instability is less severe if the interaction of $\boldsymbol{u}$ on $\boldsymbol{A}$ is removed. However, experiment 3 will show that the spurious oscillation that prelude the instability are also present for this case. Through the experiments on partial scheme C as summarized in figs. 3.5 and 3.6,

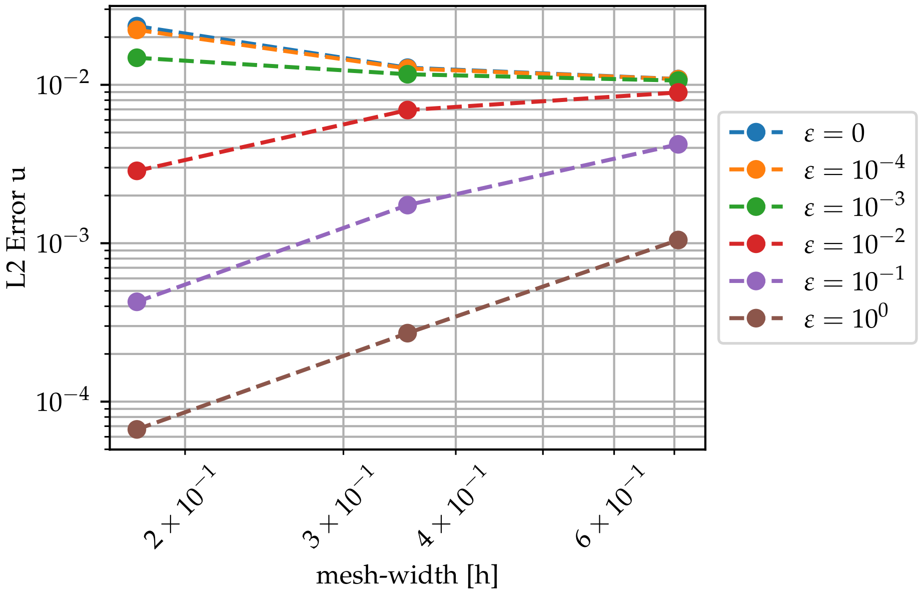

Figure 3.1: Experiment 1 performed using scheme A using a CFL condition of $\sqrt{\frac{1}{5}}$ on a simplicial mesh for varying viscosities ε and fixed conductivity $\sigma = \infty$.

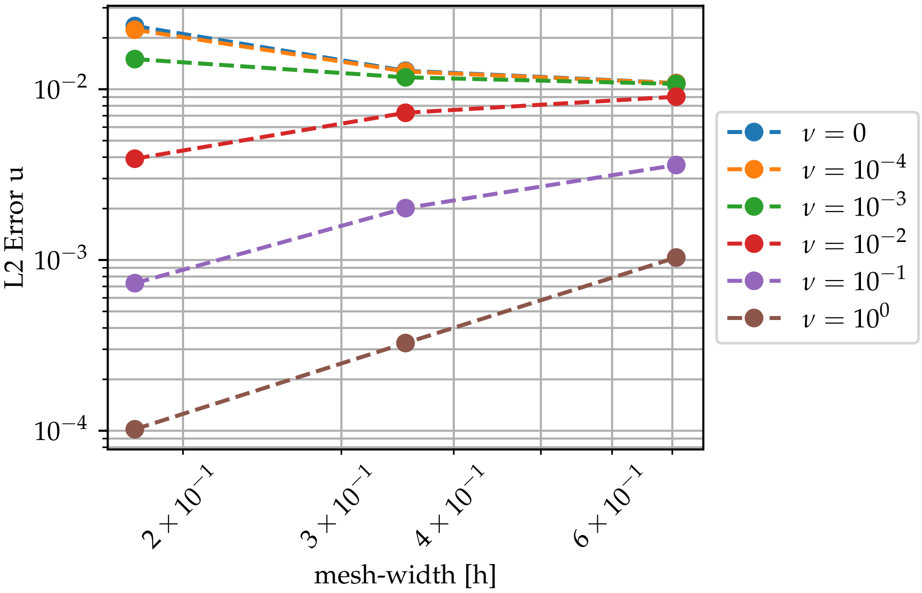

Figure 3.2: Experiment 1 performed using scheme A using a CFL condition of $\sqrt{\frac{1}{5}}$ on a simplicial mesh for fixed viscosity $\varepsilon = 0$ and varying values for the conductivity $\sigma = \frac{1}{\nu}$.

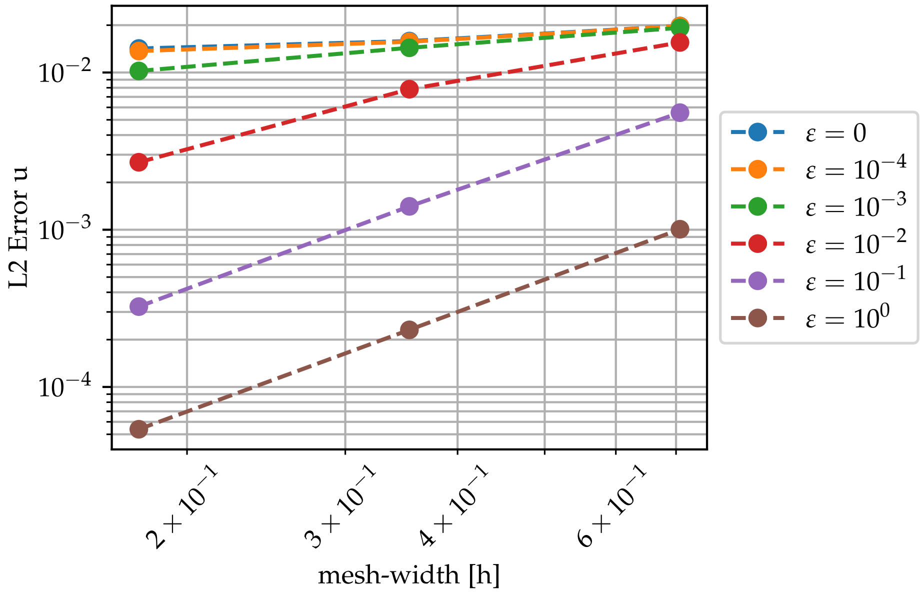

Figure 3.3: Experiment 1 performed using partial scheme E using a CFL condition of $\sqrt{\frac{1}{5}}$ on a simplicial mesh for varying viscosities ε and fixed conductivity $\sigma = \infty$.

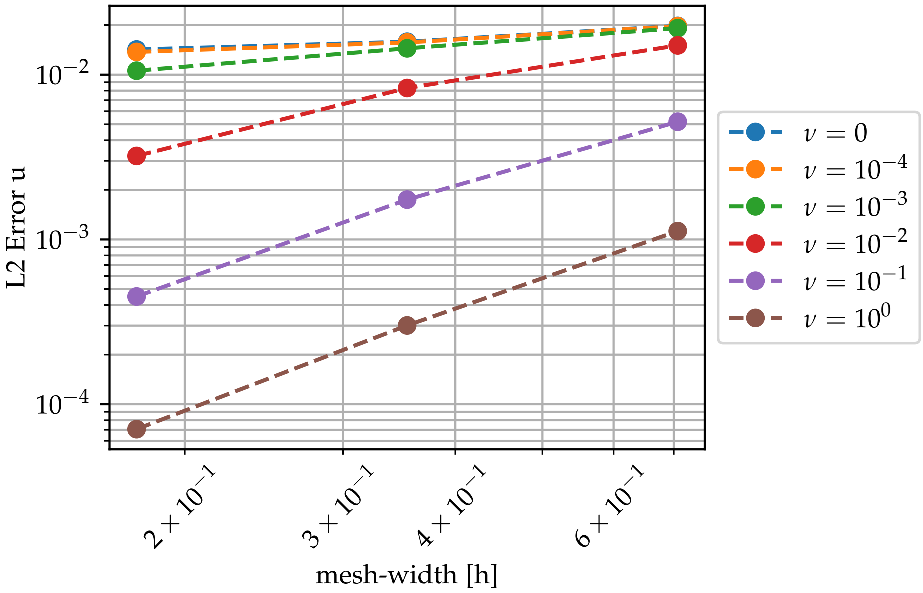

Figure 3.4: Experiment 1 performed using partial scheme E using a CFL condition of $\sqrt{\frac{1}{5}}$ on a simplicial mesh for fixed viscosity $\varepsilon = 0$ and varying values for the conductivity $\sigma = \frac{1}{\nu}$.

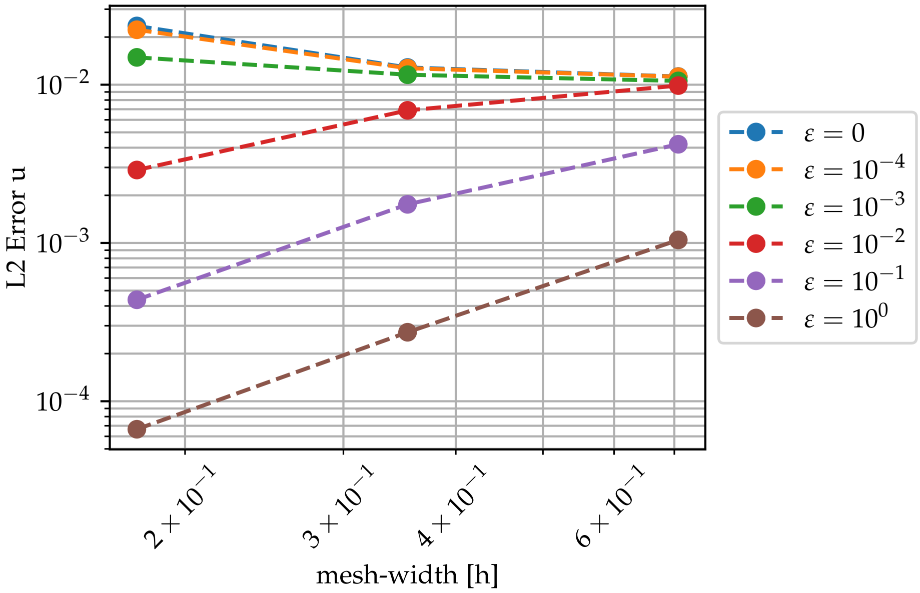

Figure 3.5: Experiment 1 performed using partial scheme C using a CFL condition of $\sqrt{\frac{1}{5}}$ on a simplicial mesh for varying viscosities ε and fixed conductivity $\sigma = \infty$.

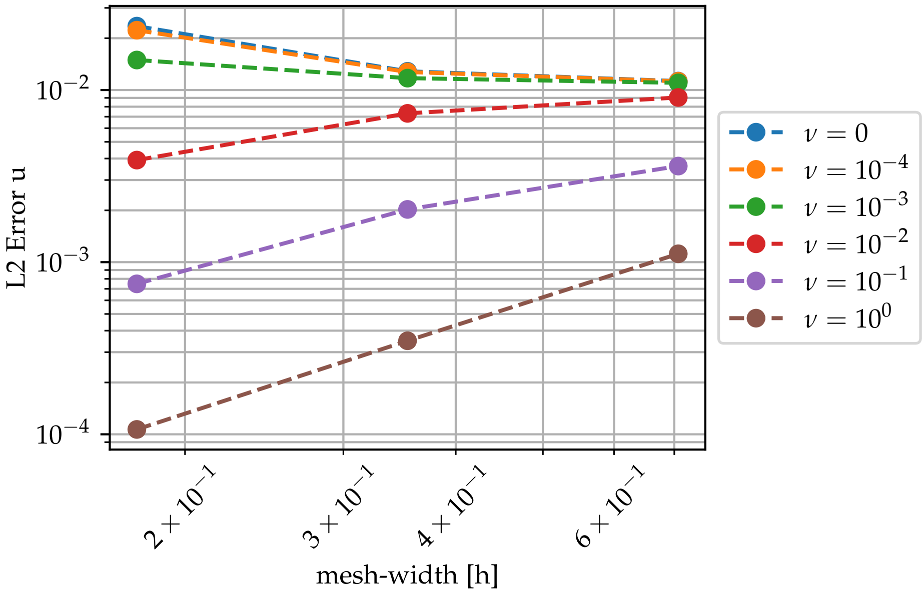

Figure 3.6: Experiment 1 performed using partial scheme C using a CFL condition of $\sqrt{\frac{1}{5}}$ on a simplicial mesh for fixed viscosity $\varepsilon = 0$ and varying values for the conductivity $\sigma = \frac{1}{\nu}$.

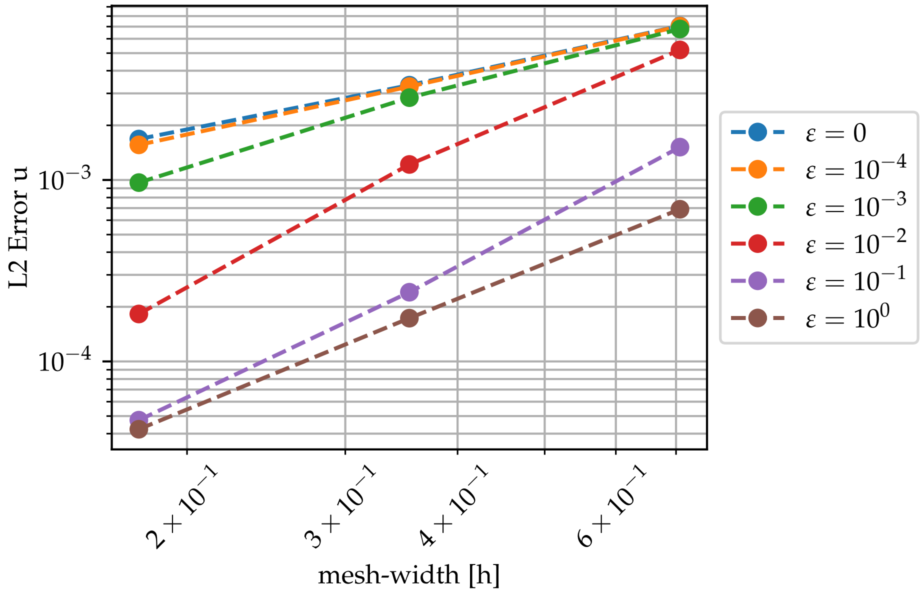

Figure 3.7: Experiment 1 performed using partial scheme B using a CFL condition of $\sqrt{\frac{1}{5}}$ on a simplicial mesh for varying viscosities ε and fixed conductivity $\sigma = \infty$.

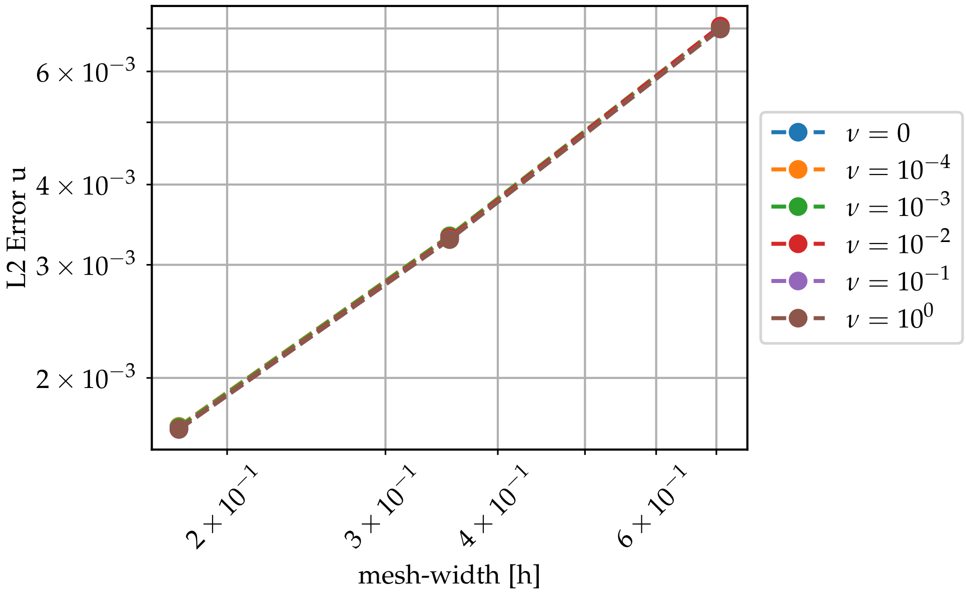

Figure 3.8: Experiment 1 performed using partial scheme B using a CFL condition of $\sqrt{\frac{1}{5}}$ on a simplicial mesh for fixed viscosity $\varepsilon = 0$ and varying values for the conductivity $\sigma = \frac{1}{\nu}$.

we see that A_h^n in the Lorentz force does not have much of an influence on stability. Through the experiments on partial scheme B as summarized in figs. 3.7 and C.9, we observe that the computation of J_h^n is important for the cause of the instability, since replacing A_h^n by the exact solution removes the instability.

The experiments in chapters 1 and 2 show that the semi-Lagrangian scheme is stable for the incompressible Euler equations and the vectorial advection equation. This fact in combination with the reasoning above, leads us to the conclusion that the instability is likely caused by the discretization of the Lorentz force.

For convergence rates for the magnetic vector potential and convergence analysis of the L^∞-error, we refer to the results in figs. 3.1, 3.4 to 3.7 and C.1 to C.27.

3.4.3 Experiment 2

In this section, we consider the following problem inspired by [29]. We fix the magnetic coupling factor $\kappa = 1$, but we vary the viscosity ν and conductivity σ. We choose the source terms and boundary conditions such that

$$\boldsymbol{u}(t, \boldsymbol{x}) = \begin{bmatrix} x_2 e^{-t} \\ x_3 \cos(t) \\ x_1 \end{bmatrix} \tag{3.25}$$

and

$$\boldsymbol{A}(t, \boldsymbol{x}) = \begin{bmatrix} x_3 \\ 0 \\ x_2 \cos(t) \end{bmatrix} \tag{3.26}$$

are solutions to the incompressible MHD equations. This case is of particular interest, because the linear nature of the solution means that it lies in the space of second-order discrete differential forms. We run all the experiments on the domain $\Omega = [-\frac{1}{2}, \frac{1}{2}]^3$ and until time $T = 0.5$.

The results are similar to those of Experiment 1. However, using partial scheme E, we now observe first-order convergence as summarized in figs. 3.10 and C.28. The results are unconclusive on whether the scheme can be considered stable in this case, but the performance is certainly better compared to experiment 1. We will see similar behaviour of partial scheme E for experiment 3, where we have the ability to visualize the results for a better understanding. Scheme A, B, and C perform similarly as for experiment 1. The results of a plethora of similar experiments can be found in figs. 3.10 and C.28 to C.58.

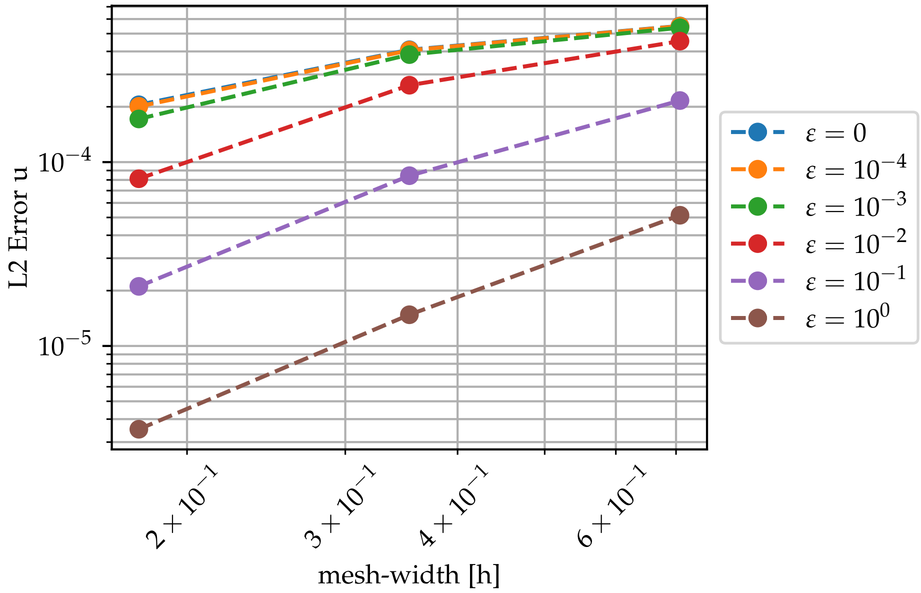

Figure 3.9: Experiment 2 performed using partial scheme E using a CFL condition of $\sqrt{\frac{1}{20}}$ on a simplicial mesh for varying viscosities ε and fixed conductivity $\sigma = \infty$.

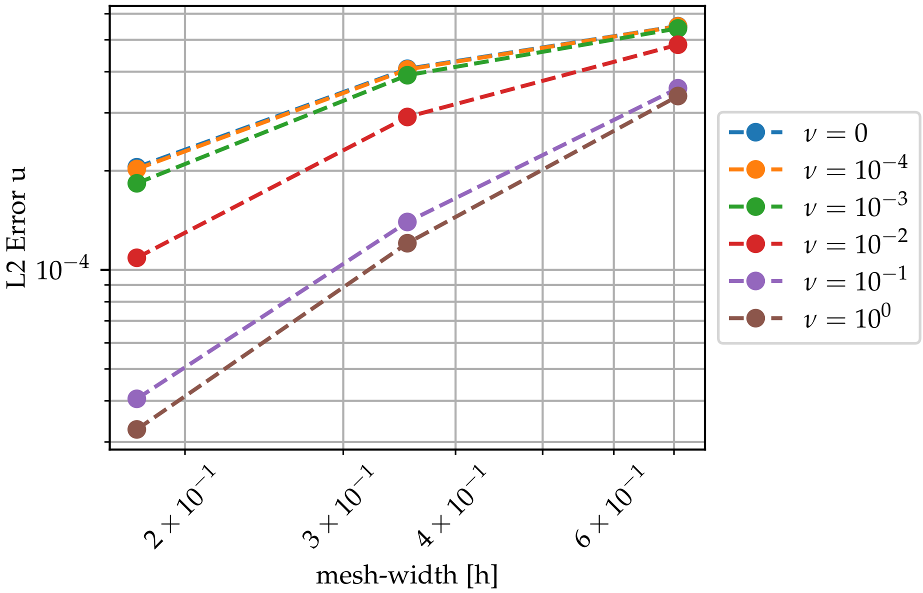

Figure 3.10: Experiment 2 performed using partial scheme E using a CFL condition of $\sqrt{\frac{1}{20}}$ on a simplicial mesh for fixed viscosity $\varepsilon = 0$ and varying values for the conductivity $\sigma = \frac{1}{\nu}$.

3.4.4 Experiment 3

In this section, we consider an experiment in 2D for the incompressible MHD equations with $\kappa = 0.1$, $\varepsilon = 0$, $\sigma = \infty$, vanishing normal boundary conditions, and a source term such that

$$\boldsymbol{u}(t, \boldsymbol{x}) = \begin{bmatrix} \sin(\pi y)\cos(\pi x) \\ -\cos(\pi y)\sin(\pi x) \end{bmatrix} e^{-t} \tag{3.27}$$

and

$$\boldsymbol{A}(t, \boldsymbol{x}) = \begin{bmatrix} \sin(\pi y)\cos(\pi x) \\ -\cos(\pi y)\sin(\pi x) \end{bmatrix} e^{-t} \tag{3.28}$$

form a exact solution. We refer to fig. 3.12 for a summary of the results. We observe a clear instability for scheme A, while partial scheme B performs very well and remains stable. Partial scheme E performs rather well as it remains stable, but converges with a rather slow rate.

In figs. 3.16 to 3.18, we display the magnitude of the velocity field, magnetic vector potential, and Lorentz force for different times as computed using scheme A, B, and E. We observe that for scheme A spurious oscillations in the Lorentz force appear around $t = 0.05$. Then, these spurious oscillations spill over into the the velocity field and we see clear spurious oscillations in the velocity field around $t = 0.1$. Eventually these spurious oscillations end up in an instability. The magnetic vector potential suffers the least from the spurious oscillations as it is not directly influenced by the Lorentz force. Partial scheme E shows similar spurious oscillations compared to scheme A, but needs more time for the oscillations to appear. Partial scheme B shows no spurious oscillations or instability.

In figs. 3.13 to 3.15, we display the magnitude of the velocity field, magnetic vector potential, and Lorentz force for different meshes as computed using scheme A, B, and E. We observe that the spurious oscillations have periods that are associated to the mesh-width.

From this experiment, we can conclude that scheme A and E show spurious oscillations, while partial scheme B remains stable. A potential reason for the instability of scheme A could be that it does not satisfy an appropriate energy bound. In [31], Hu et al. designed a numerical scheme that satisfies a discrete energy bound that is analogous to the continuous energy bound associated with the MHD equations. The discrete energy bound for the case of ideal MHD is

$$\|\boldsymbol{u}_h^n\|^2 + 2\tau\kappa \|\boldsymbol{J}_h^n\|^2 \leq \left\|\boldsymbol{u}_h^{n-1}\right\|^2 + 2\tau \left(\boldsymbol{f}_h^n, \boldsymbol{u}_h^n\right). \tag{3.29}$$

We track the energy (left-hand side of the inequality) and the energy bound (right-hand side of the inequality) and visualize the results in fig. 3.11. We observe that the discrete energy bound is not satisfied.

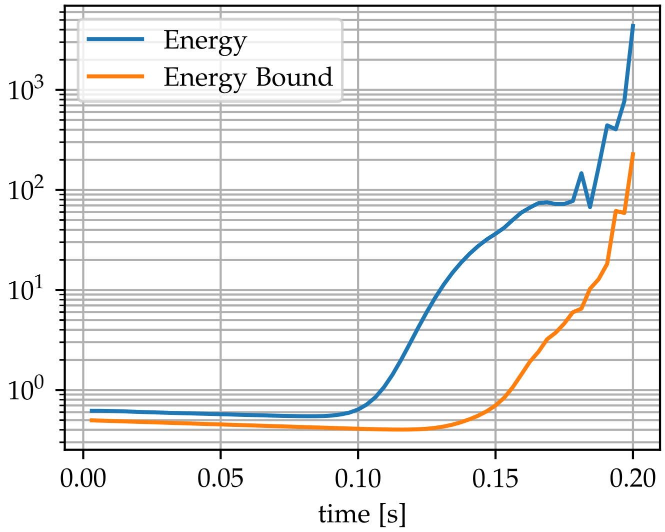

Figure 3.11: Experiment 3: Energy and energy bound defined through the left- and right-hand side of eq. (3.29) computed using scheme A on a simplicial mesh with mesh-width $h = 0.0474897$ and time-step $\tau = 0.003125$.

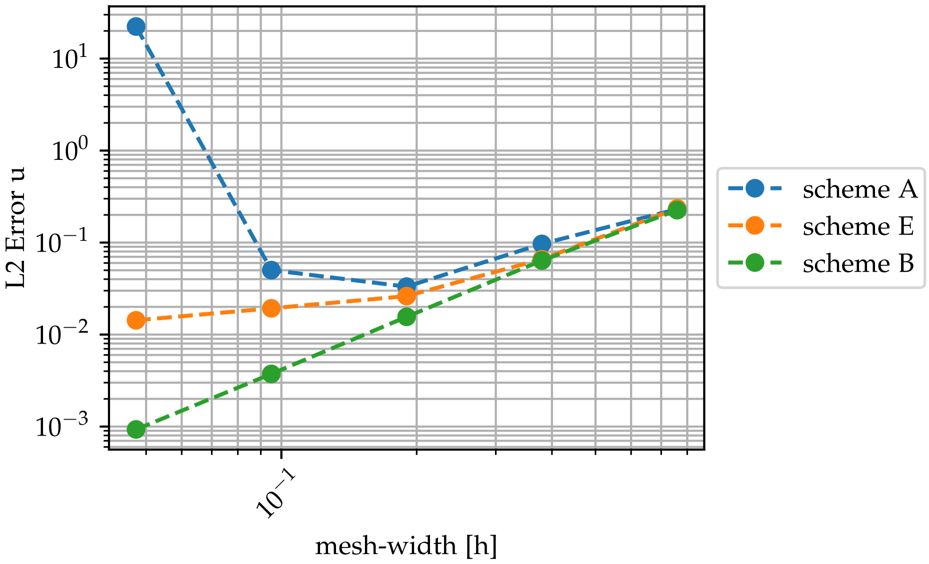

Figure 3.12: Experiment 3 performed using different schemes using a CFL condition of 0.06580367 on a simplicial mesh for fixed viscosity $\varepsilon = 0$ and fixed conductivity $\sigma = \infty$. The final time $T = 0.2$.

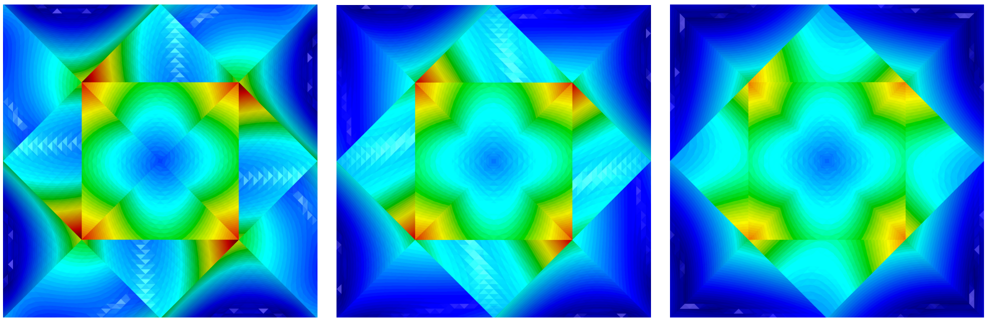

(a) Scheme A, $h = 0.3799$

(b) Partial scheme E, $h = 0.3799$

(c) Partial scheme B, $h = 0.3799$

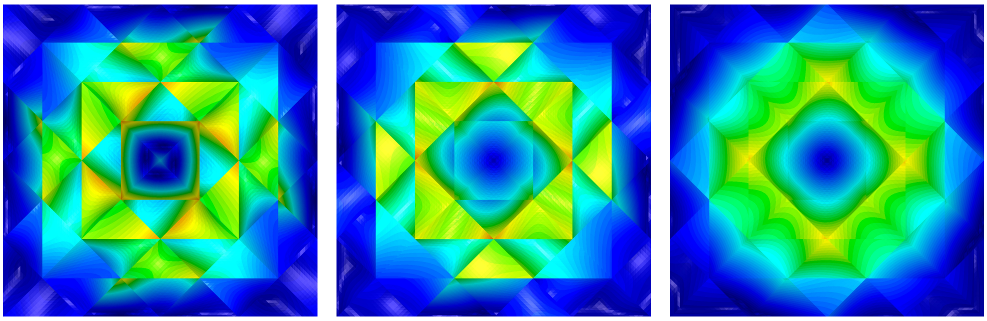

(d) Scheme A, $h = 0.1900$

(e) Partial scheme E, $h = 0.1900$

(f) Partial scheme B, $h = 0.1900$

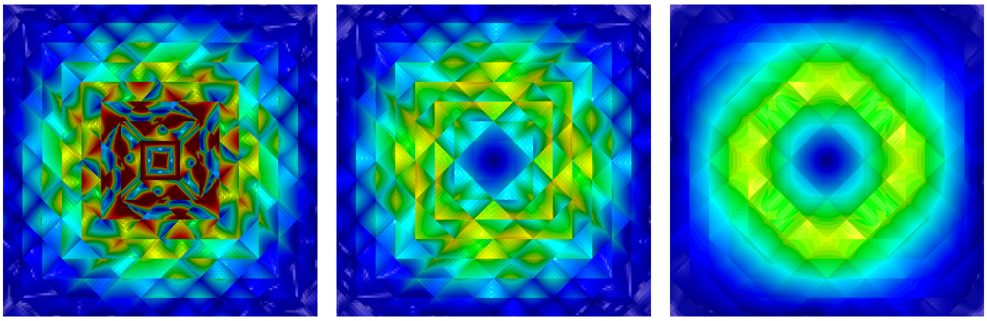

(g) Scheme A, $h = 0.09498$

(h) Partial scheme E, $h = 0.09498$

(i) Partial scheme B, $h = 0.09498$

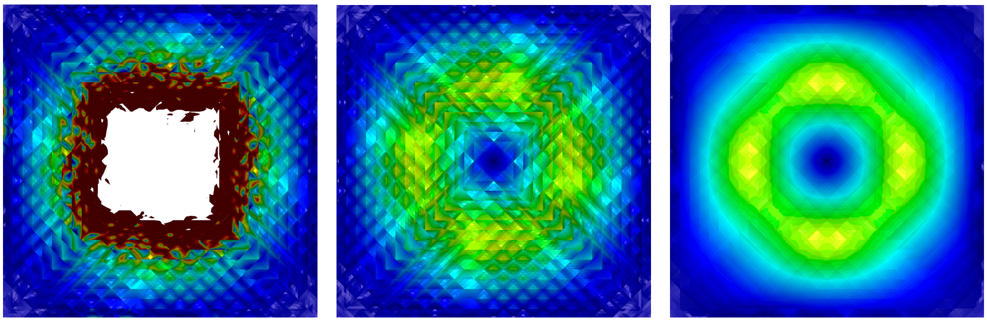

(j) Scheme A, $h = 0.04749$

(k) Partial scheme E, $h = 0.04749$

(l) Partial scheme B, $h = 0.04749$

Figure 3.13: Experiment 3: magnitude of the computed Lorentz force at $T = 0.2$ using different schemes on simplicial meshes with mesh-width h and time-step $\tau = 0.0658037427h$.

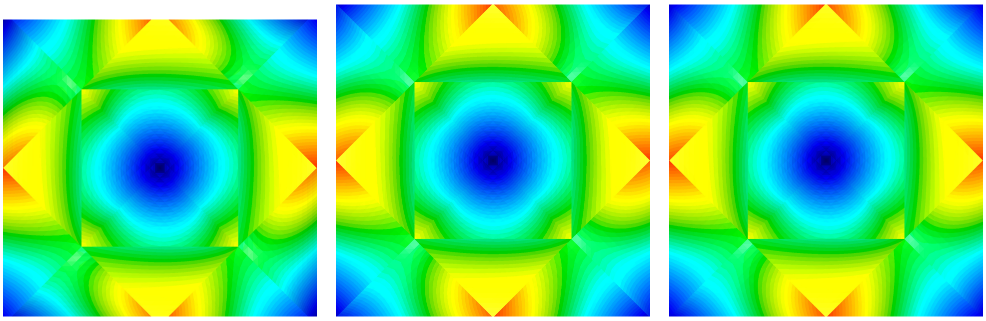

(a) Scheme A, $h = 0.3799$ (b) Partial scheme E, $h = 0.3799$ (c) Partial scheme B, $h = 0.3799$

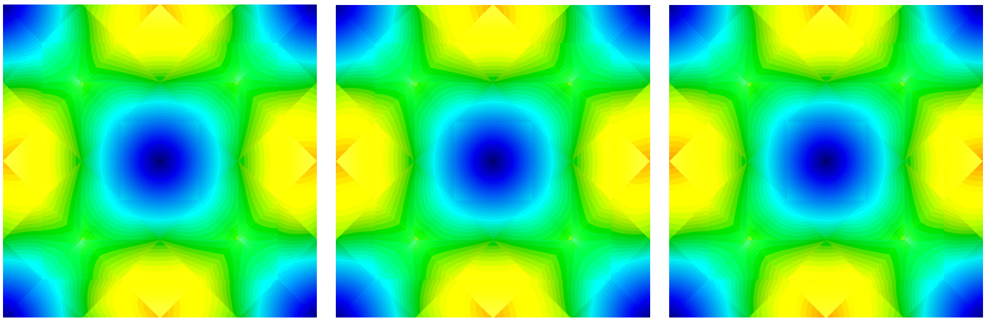

(d) Scheme A, $h = 0.1900$ (e) Partial scheme E, $h = 0.1900$ (f) Partial scheme B, $h = 0.1900$

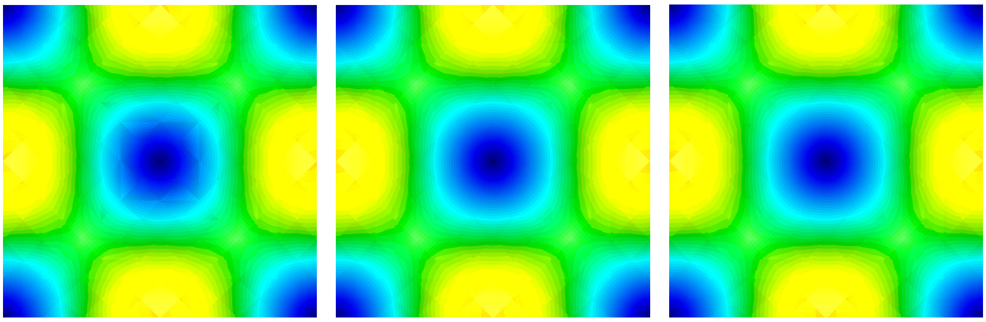

(g) Scheme A, $h = 0.09498$ (h) Partial scheme E, $h = 0.09498$ (i) Partial scheme B, $h = 0.09498$

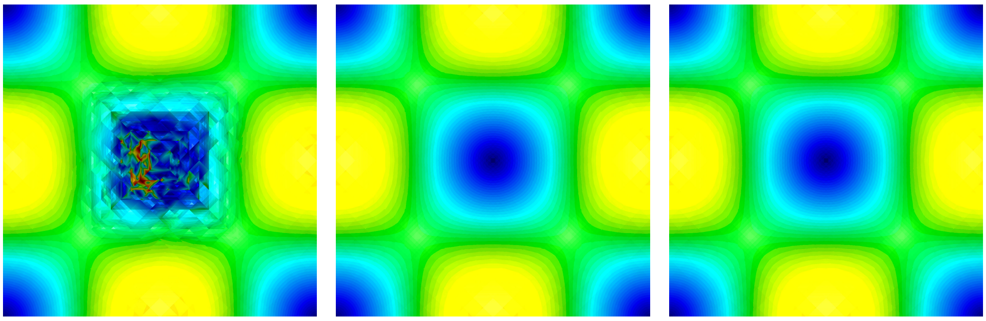

(j) Scheme A, $h = 0.04749$ (k) Partial scheme E, $h = 0.04749$ (l) Partial scheme B, $h = 0.04749$

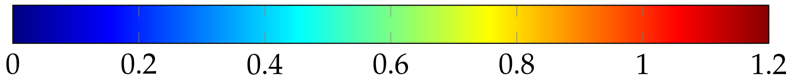

Figure 3.14: Experiment 3: magnitude of computed A_h^n at $T = 0.2$ using different schemes on simplicial meshes with mesh-width h and time-step $\tau = 0.0658037427h$.

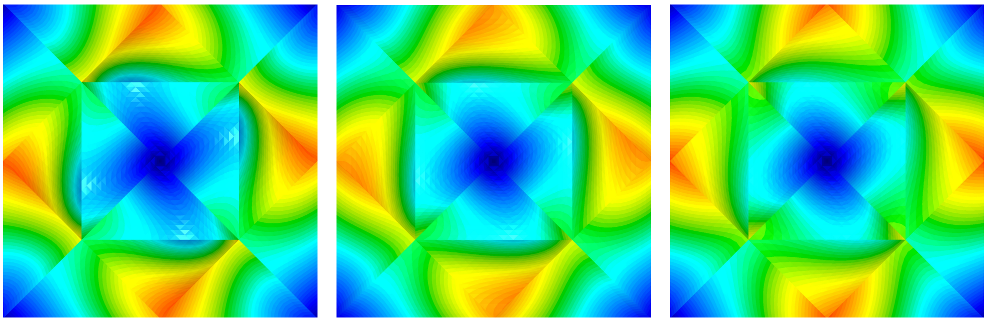

(a) Scheme A, $h = 0.3799$

(b) Partial scheme E, $h = 0.3799$

(c) Partial scheme B, $h = 0.3799$

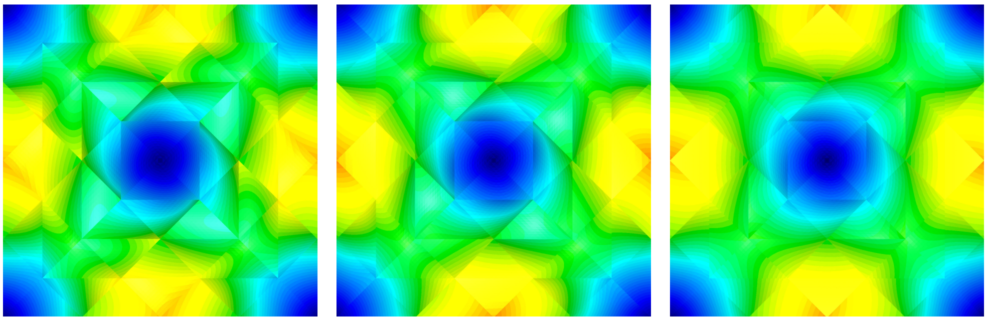

(d) Scheme A, $h = 0.1900$

(e) Partial scheme E, $h = 0.1900$

(f) Partial scheme B, $h = 0.1900$

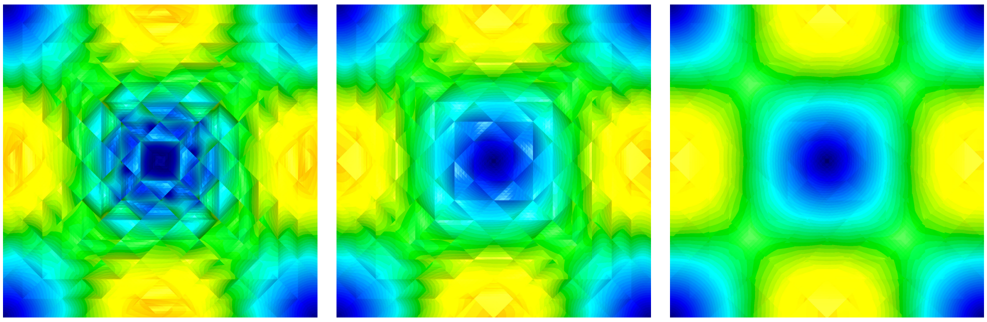

(g) Scheme A, $h = 0.09498$

(h) Partial scheme E, $h = 0.09498$

(i) Partial scheme B, $h = 0.09498$

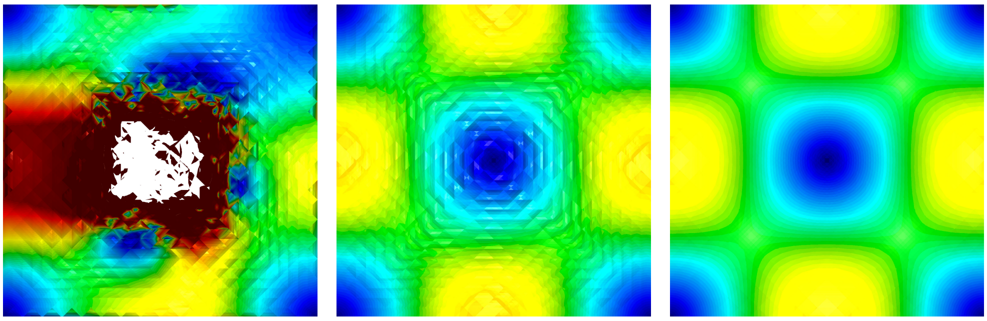

(j) Scheme A, $h = 0.04749$

(k) Partial scheme E, $h = 0.04749$

(l) Partial scheme B, $h = 0.04749$

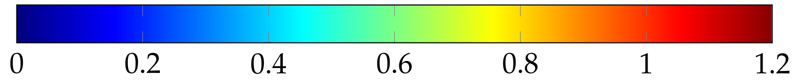

Figure 3.15: Experiment 3: magnitude of computed $\boldsymbol{u}_h^n$ at $T = 0.2$ using different schemes on simplicial meshes with mesh-width h and time-step $\tau = 0.0658037427h$.

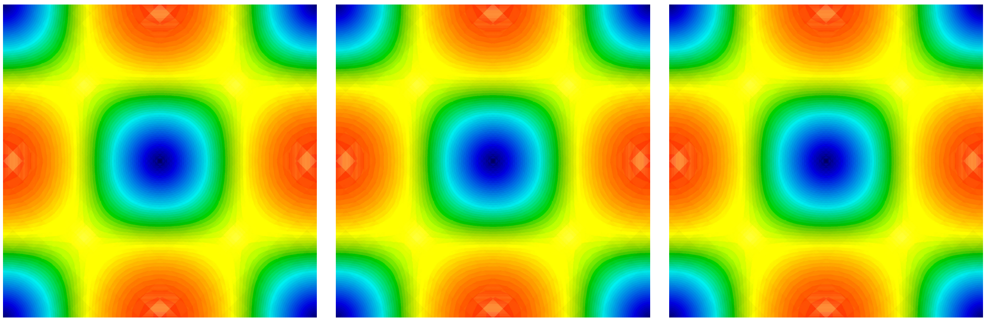

(a) Scheme A, $t = 0$

(b) Partial scheme E, $t = 0$

(c) Partial scheme B, $t = 0$

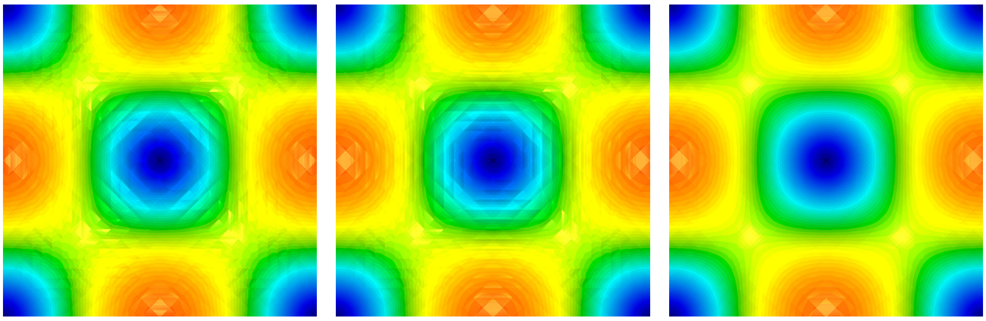

(d) Scheme A, $t = 0.05$

(e) Partial scheme E, $t = 0.05$

(f) Partial scheme B, $t = 0.05$

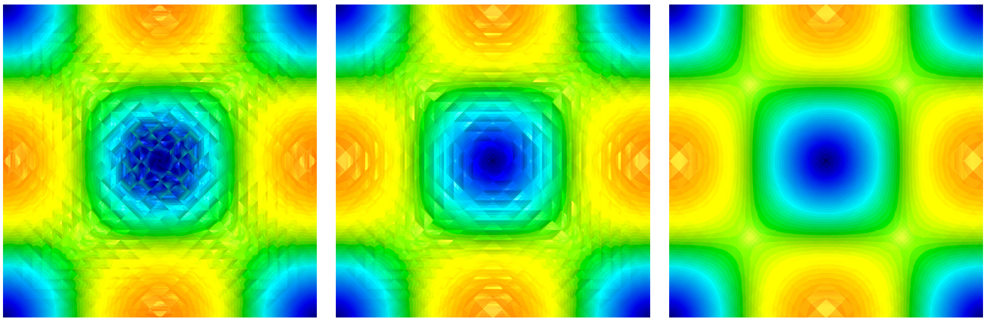

(g) Scheme A, $t = 0.1$

(h) Partial scheme E, $t = 0.1$

(i) Partial scheme B, $t = 0.1$

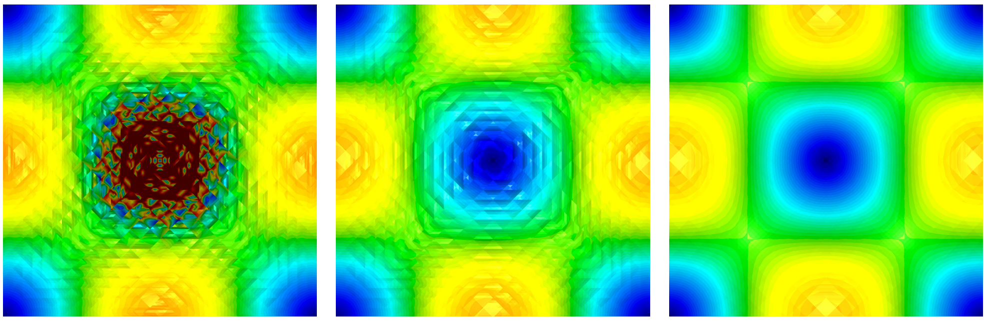

(j) Scheme A, $t = 0.15$

(k) Partial scheme E, $t = 0.15$

(l) Partial scheme B, $t = 0.15$

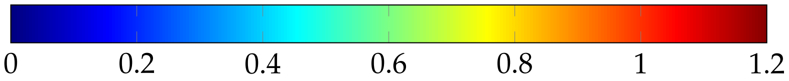

Figure 3.16: Experiment 3: magnitude of computed $\boldsymbol{u}_h^n$ using scheme A on a simplicial mesh with mesh-width $h = 0.0474897$ and time-step $\tau = 0.003125$.

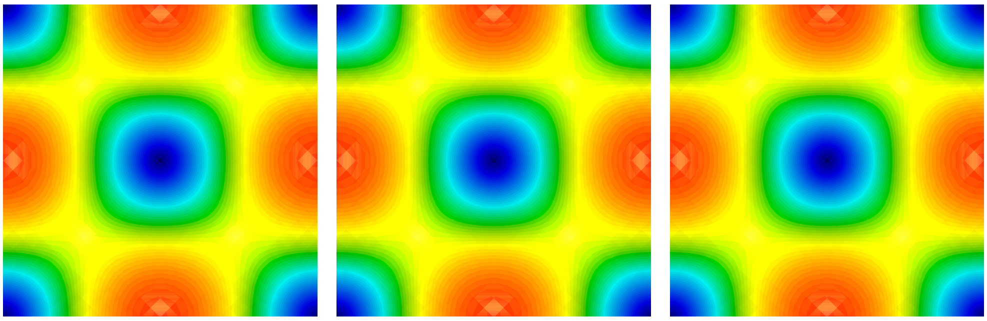

(a) Scheme A, $t = 0$

(b) Partial scheme E, $t = 0$

(c) Partial scheme B, $t = 0$

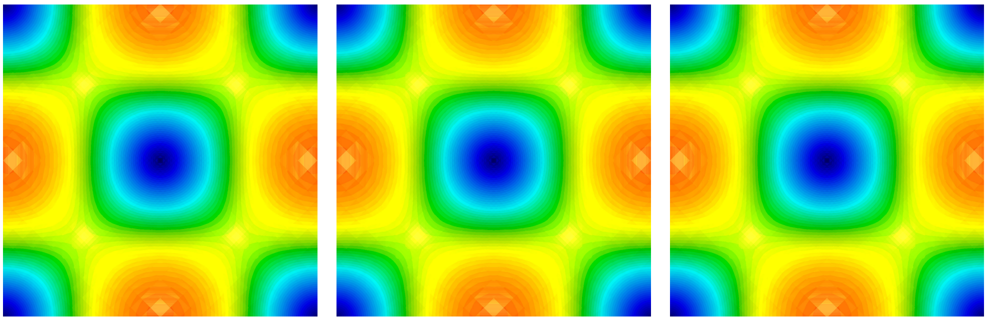

(d) Scheme A, $t = 0.05$

(e) Partial scheme E, $t = 0.05$

(f) Partial scheme B, $t = 0.05$

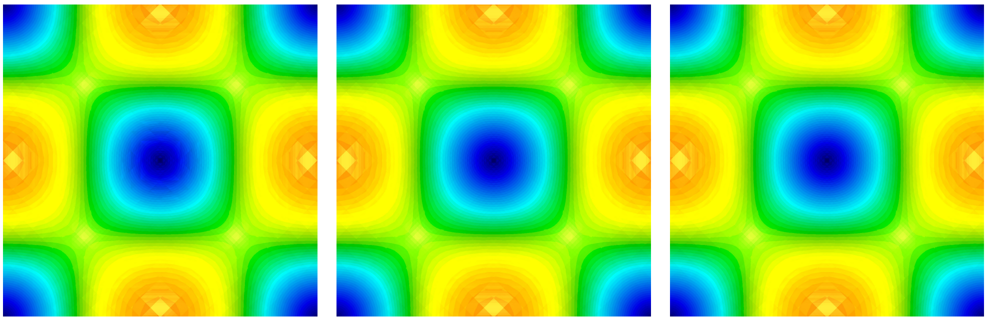

(g) Scheme A, $t = 0.1$

(h) Partial scheme E, $t = 0.1$

(i) Partial scheme B, $t = 0.1$

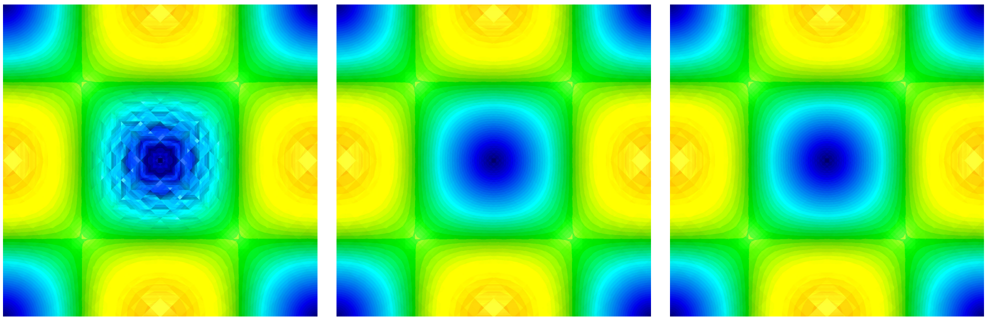

(j) Scheme A, $t = 0.15$

(k) Partial scheme E, $t = 0.15$

(l) Partial scheme B, $t = 0.15$

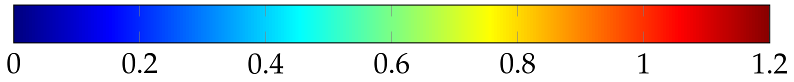

Figure 3.17: Experiment 3: magnitude of computed $\boldsymbol{A}_h^n$ using scheme A on a simplicial mesh with mesh-width $h = 0.0474897$ and time-step $\tau = 0.003125$.

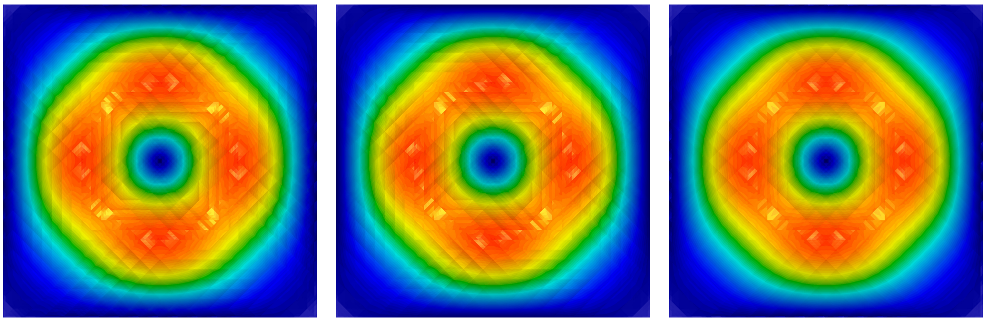

(a) Scheme A, $t = 0.003125$

(b) Partial scheme E, $t = 0.003125$

(c) Partial scheme B, $t = 0.003125$

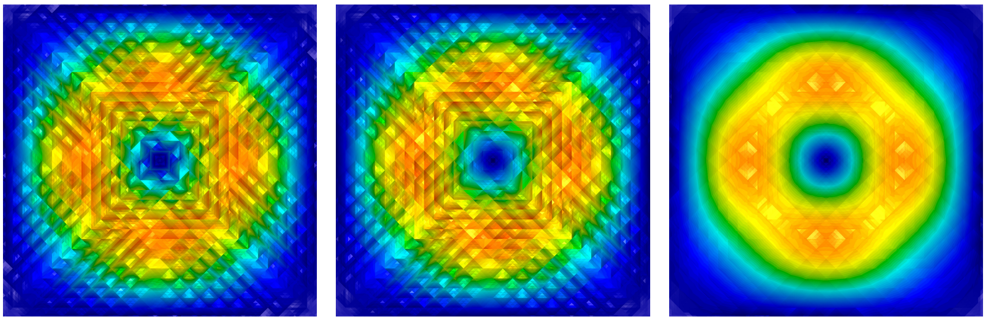

(d) Scheme A, $t = 0.05$

(e) Partial scheme E, $t = 0.05$

(f) Partial scheme B, $t = 0.05$

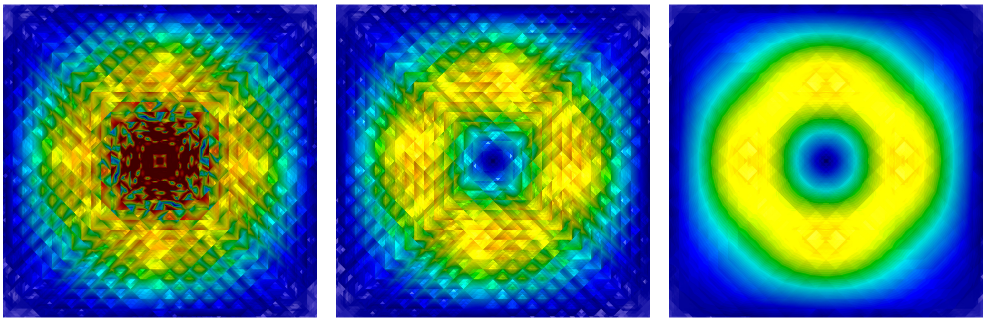

(g) Scheme A, $t = 0.1$

(h) Partial scheme E, $t = 0.1$

(i) Partial scheme B, $t = 0.1$

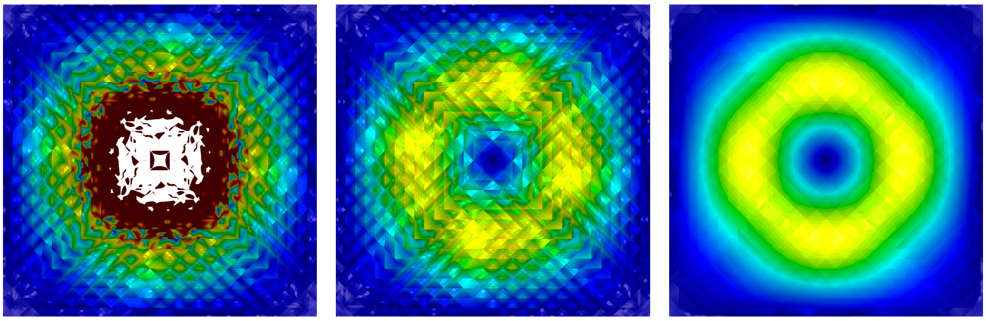

(j) Scheme A, $t = 0.15$

(k) Partial scheme E, $t = 0.15$

(l) Partial scheme B, $t = 0.15$

Figure 3.18: Experiment 3: magnitude of computed Lorentz force using scheme A on a simplicial mesh with mesh-width $h = 0.0474897$ and time-step $\tau = 0.003125$.

Chapter 4

Conclusion

In this work, a fully-discrete method for the advection of discrete differential forms has been extended to second-order. Using this extension, a second-order, structure-preserving numerical scheme was developed for the transient incompressible Euler equations that preserves both energy and helicity. The advantage of this scheme is that it converges independently of the value for the viscosity. Also, advances were made on the extension of this method to the incompressible, resistive and viscous magnetohydrodynamics equations. Unfortunately, the developed scheme gets unstable in the limit to ideal magnetohydrodynamics. It has been established that the instability is caused by the discretization of the Lorentz force and the failure of the scheme to satisfy an appropriate energy bound. More work is needed to see if this limitation can be avoided.

Appendix A

An introduction to Lie theory

We shall need the notion of Lie groups and their Lie algebras. Let us start with the definition of a group.

Definition 16 A group G is a set G equipped with a binary operator $\cdot : G \times G \mapsto G$ such that

- $(a \cdot b) \cdot c = a \cdot (b \cdot c)$ for all $a, b, c \in G$,
- $\exists e \in G$ s.t. for all $g \in G$ we have $e \cdot g = g$,
- For all $a \in G$ there exists a $b \in G$ s.t. $a \cdot b = e$.

This allows us to define a Lie group.

Definition 17 A Lie group G is a group G that is also a smooth manifold that satisfies

- The map $\cdot : G \times G \mapsto G$ is smooth,
- The map $i : G \mapsto G$, mapping elements to their inverse, is smooth.

Lie groups are of particular interest in physics, because they can be used to describe symmetries. To see this, we consider "right-invariant vector fields". With this goal in mind, we proceed by defining for $g \in G$

$$\begin{aligned} r_g &: G \mapsto G \\ G \ni f &\mapsto r_g(f) := f \cdot g \in G \end{aligned} \tag{A.1}$$

This allows us to define for a vector field X and $g \in G$ the following.

$$\begin{aligned} R_{g*} &: \Gamma(TG) \mapsto \Gamma(TG), \\ \Gamma(TG) \ni X &\mapsto R_{g*}X, \end{aligned} \tag{A.2}$$

where

$$\forall f \in C^\infty(G), p \in G : (R_{g*}X)_p(f) := X_{r_g^{-1}(p)}(f \circ r_g) = X_{pg^{-1}}(f \circ r_g). \tag{A.3}$$

We say $X \in \Gamma(TG)$ is right-invariant if

$$R_{g*}X = X \Leftrightarrow \forall f \in C^\infty(G) : X(f \circ r_g) = X(f) \circ r_g. \tag{A.4}$$

We define the space of right-invariant vector fields on G as the Lie Algebra of G.

Definition 18 Let G be a Lie Group, then we define $\mathfrak{g} := \mathcal{L}(G)$ as the corresponding Lie Algebra, where $\mathcal{L}(G)$ denotes the space of all right-invariant vector fields. The multiplication operator on $\mathcal{L}(G)$ is defined for $X, Y \in \mathcal{L}(G)$

$$\forall f \in C^\infty(G) : XY(f) := X(Y(f)).$$

The corresponding Lie Bracket on $\mathcal{L}(G)$ is defined as

$$[X, Y] = XY - YX.$$

An important result in Lie Theory is the following

Lemma 6 $T_eG \cong \mathfrak{g}$.

Proof We refer to [56]. □

Remark 7 The isomorphism $j : T_eG \mapsto \Gamma(TG)$ corresponding to the above lemma is the following

$$\begin{aligned} T_eG \ni \dot{q} &\mapsto j(q) \\ j(X)|_g(f) &= \frac{d}{ds}\Big|_{s=0}(f(q(s) \cdot g)). \end{aligned} \tag{A.5}$$

We define the Lie bracket $[\cdot,\cdot] : \mathfrak{g} \times \mathfrak{g} \mapsto \mathfrak{g}$ for $X, Y \in \mathfrak{g}$ as

$$[X, Y] = j^{-1}[j(X), j(Y)]. \tag{A.6}$$

Appendix B

Proofs for the geometric Euler equations

B.1 Proof of lemma 2

It is clear that $J_0(x) = Id$. To prove the ordinary differential equation given in equation (2.8), consider

$$\begin{aligned}\frac{\partial J_t}{\partial t}(x) &= \frac{\partial}{\partial t}\det(D_x\boldsymbol{\varphi}_t(x))\\ &= \left.\frac{\partial}{\partial s}\right|_{s=0}\det(D_x\varphi_s \circ \boldsymbol{\varphi}_t(x))\\ &= \left.\frac{\partial}{\partial s}\right|_{s=0}\det\left[D\varphi_s\big|_{\boldsymbol{\varphi}_t(x)} D\boldsymbol{\varphi}_t\big|_x\right]\\ &= \det\left[D\boldsymbol{\varphi}_t\big|_x\right]\left.\frac{\partial}{\partial s}\right|_{s=0}\det\left[D\varphi_s\big|_{\boldsymbol{\varphi}_t(x)}\right]\\ &= J_t(x)\left.\frac{\partial}{\partial s}\right|_{s=0}\det\left[D\varphi_s\big|_{\boldsymbol{\varphi}_t(x)}\right].\end{aligned} \tag{B.1}$$

For ease of notation, let us set $A(t) := D_x\boldsymbol{\varphi}_t(x)$, then $A(0) = Id$. Also, let us consider the determinant as a map, $\det : \mathbb{R}^{d^2} \cong \mathcal{L}(\mathbb{R}^d) \mapsto \mathbb{R}$. In the following, we will consider A as an element of $\mathcal{L}(\mathbb{R}^d)$ or $\mathbb{R}^{d^2}$ as needed. We have

$$\begin{aligned}\left.\frac{d}{dt}\right|_{t=0} \det(A(t)) &= (D\det)(A(0))A'(0) \\ &= \left.\frac{d}{ds}\right|_{s=0} \det(A(0)+sA'(0)) \\ &= \left.\frac{d}{ds}\right|_{s=0} \det(I+sA'(0)) \\ &= \operatorname{tr}(A'(0)),\end{aligned} \tag{B.2}$$

where we used the chain rule and inverse chain rule, and the identity

$$\det(I+sB) = 1 + s\operatorname{tr}(B) + O(s^2), \tag{B.3}$$

which holds for small enough s. We thus conclude

$$\begin{aligned}\frac{\partial}{\partial t}J_t(x) &= \operatorname{tr}\left(D\left.\frac{\partial \boldsymbol{\varphi}_0}{\partial t}\right|_{\boldsymbol{\varphi}_t(x)}\right) J_t(x) \\ &= \operatorname{tr}\left(Df|_{\boldsymbol{\varphi}_t(x)}\right) J_t(x) \\ &= (\nabla\cdot f)(t,\boldsymbol{\varphi}_t)J_t(x)\end{aligned} \tag{B.4}$$

B.2 Proof of theorem 5

We prove the different cases case-by-case.

- $1 \Leftrightarrow 2$: Let us extend $g(t)$ to an arbitrary curve $g_\varepsilon(t)$ such that $g_0(t) = g(t)$, $g_\varepsilon(0) = g(0)$, and $g_\varepsilon(T) = g(T)$. Then we can write

  $$\delta g(t) = \left.\frac{d}{d\varepsilon}\right|_{\varepsilon=0} g_\varepsilon(t) \tag{B.5}$$

  We have

  $$\begin{aligned}\delta\xi(t) &= \left.\frac{d}{d\varepsilon}\right|_{\varepsilon=0}\left[T_{g_\varepsilon(t)}L_{g_\varepsilon(t)^{-1}}\dot{g}_\varepsilon(t)\right] \\ &= \left.\frac{d}{d\varepsilon}\right|_{\varepsilon=0}\left[\left.\frac{d}{ds}\right|_{s=t} g_\varepsilon(t)^{-1}g_\varepsilon(s)\right]\end{aligned} \tag{B.6}$$

  Let us define

  $$\eta(t) := T_{g_0(t)}L_{g_0(t)^{-1}}\left.\frac{d}{d\varepsilon}\right|_{\varepsilon=0} g_\varepsilon(t) \tag{B.7}$$

  Then we have

  $$\begin{aligned}\dot{\eta}(t) &= \left.\frac{d}{ds}\right|_{s=t}\left[T_{g_0(t)}L_{g_0(t)^{-1}}\left.\frac{d}{d\varepsilon}\right|_{\varepsilon=0} g_\varepsilon(t)\right] \\ &= \left.\frac{d}{ds}\right|_{s=t}\left[\left.\frac{d}{d\varepsilon}\right|_{\varepsilon=0} g_0(t)^{-1}g_\varepsilon(t)\right]\end{aligned} \tag{B.8}$$

In the following, we will use the operator $j : T_eG \mapsto \Gamma(TG)$ as defined in appendix A. We have for $f \in C^\infty(G)$

$$\begin{aligned} j[\eta,\xi](f) &= [j(\eta), j(\xi)](f) \\ &= j(\eta)j(\xi)(f) - j(\xi)j(\eta)(f), \end{aligned} \tag{B.9}$$

where for $p \in G$

$$\begin{aligned} F(p) := j(\xi(t))(f)(p) &= \frac{d}{ds}\Big|_{s=t} f(\xi(s) \circ p) \\ &= \frac{d}{ds}\Big|_{s=t} f(g_0(t)^{-1} \circ g_0(s) \circ p), \end{aligned} \tag{B.10}$$

which leads to

$$\begin{aligned} j(\eta(t))j(\xi(t))(f)(p) &= j(\eta)(F)(p) \\ &= \frac{d}{d\varepsilon}\Big|_{\varepsilon=0} F(g_0^{-1} \circ g_\varepsilon \circ p) \\ &= \frac{d}{d\varepsilon}\Big|_{\varepsilon=0} \frac{d}{ds}\Big|_{s=t} f(g_0(t)^{-1} \circ g_0(s) \circ g_0(s)^{-1} \circ g_\varepsilon(s) \circ p) \\ &= \frac{d}{d\varepsilon}\Big|_{\varepsilon=0} \frac{d}{ds}\Big|_{s=t} f(g_0(t)^{-1} \circ g_\varepsilon(s) \circ p) \\ &= \left[\frac{d}{d\varepsilon}\Big|_{\varepsilon=0} \frac{d}{ds}\Big|_{s=t} g_0(t)^{-1} \circ g_\varepsilon(s)\right] (f(\cdot \circ p)) = j(\dot\eta(t))(f)(p) \end{aligned} \tag{B.11}$$

Thus

$$j\dot\eta(t) = j(\eta)j(\xi). \tag{B.12}$$

Similarly, we can show

$$j\delta\xi(t) = j(\xi)j(\eta). \tag{B.13}$$

We thus find

$$[\xi, \eta] = \delta\xi - \dot\eta \tag{B.14}$$

- 2 ⇔ 3: Follows by a standard variational argument. See [35] for details.

B.3 Proof of theorem 4

Let φ_ε be a variation of φ, and define $v_\varepsilon := \dot\varphi_\varepsilon \circ \varphi_\varepsilon^{-1}$. Since φ_ε are diffeomorphisms, we find

$$\frac{d}{d\varepsilon}\Big|_{\varepsilon=0} \frac{1}{2} \int_0^1 \int_\Omega |v_\varepsilon|^2 dxdt = 0. \tag{B.15}$$

This yields

$$\int_0^1 \int_\Omega \left(v(x,t), \frac{d}{d\varepsilon}\Big|_{\varepsilon=0} v_\varepsilon(x,t) \right) dxdt = 0. \tag{B.16}$$

Using equation (B.14), we find

$$\int_0^1 \int_\Omega (v(x,t), \dot{u} + [v,u])\, dxdt = 0, \tag{B.17}$$

where $u \in \mathfrak{g}$ vanishes on the endpoints. If $\Omega = \mathbb{R}^n$, we find a vector representation of $[v,u]$, that is,

$$[v,u] = \nabla u \cdot v - \nabla v \cdot u, \tag{B.18}$$

where ∇u denotes the transpose of the Jacobian of u, $J_u = \nabla u^T$. We thus obtain

$$0 = \int_0^1 \int_\Omega (v, \dot{u} + \nabla u \cdot v - \nabla v \cdot u)\, dxdt \tag{B.19}$$

Let us consider the last part of the integral,

$$\begin{aligned}
\int_\Omega (v, \nabla v \cdot u) dx &= \int_\Omega (v, J_v u) dx \\
&= \int_\Omega (J_v^T v, u) dx \\
&= \int_\Omega (\frac{1}{2} \nabla |v|^2, u) dx \\
&= \int_{\partial\Omega} \frac{1}{2} |v|^2 u \cdot n dx - \int_\Omega \frac{1}{2} |v|^2 \nabla \cdot u dx = 0,
\end{aligned} \tag{B.20}$$

since $\nabla \cdot u = 0$ and, on $\partial\Omega$, $u \cdot n = 0$, because u is the time derivative of a diffeomorphism on Ω. Note that for the second part of equation (B.19), we have

$$\begin{aligned}
\int_\Omega (v, \nabla u \cdot v) dx &= \int_\Omega (v, J_u v) dx \\
&= \int_\Omega (v, \nabla (v \cdot u)) - (u, J_v v) dx \\
&= \int_{\partial\Omega} (v \cdot u) v \cdot n dx - \int_\Omega \nabla \cdot v (v \cdot u) dx - \int_\Omega (J_v v, u) dx \\
&= - \int_\Omega (v \cdot \nabla v, u) dx,
\end{aligned} \tag{B.21}$$

since $\nabla \cdot v = 0$ and, on $\partial\Omega$, $v \cdot n = 0$, because v is the time derivative of a diffeomorphism on Ω. We thus find, after integration by parts in time with u vanishing on the endpoints,

$$\int_0^1 \int_\Omega (\dot{v} + v \cdot \nabla v, u) dxdt = 0 \tag{B.22}$$

Since this holds for arbitrary $u \in \mathfrak{g} \cong T_e SDiff(\Omega)$, we find that $\dot{v} + v \cdot \nabla v$ is orthogonal to all elements in $SDiff(\Omega)$. Now suppose that, for a vector field q, we have

$$\int_0^1 \int_\Omega (\dot{v} + v \cdot \nabla v + q, u) dxdt = 0. \tag{B.23}$$

Using the Helmholtz decomposition (see [38]), we can write $q = \nabla p + z$, where $\nabla \cdot z = 0$ (so $z \in SDiff(\Omega)$) and $\int_\Omega (\nabla p, z) dx = 0$. Then, if we choose $u = z$, we find

$$\begin{aligned} 0 &= \int_0^1 \int_\Omega (\dot{v} + v \cdot \nabla v + \nabla p + z, z) dxdt \\ &= \int_0^1 \int_\Omega (\dot{v} + v \cdot \nabla v, z) dxdt + \int_0^1 \int_\Omega (\nabla p, z) dxdt + \int_0^1 \int_\Omega (z, z) dxdt \\ &= \int_0^1 \int_\Omega (z, z) dxdt. \end{aligned} \tag{B.24}$$

We can thus conclude that $z = 0$, but p is not necessarily zero. We can now conclude that, for some p, we have

$$\dot{v} + v \cdot \nabla v + \nabla p = 0. \tag{B.25}$$

Appendix C

Some additional experimental results

This Appendix includes some additional experimental results regarding the MHD equations.

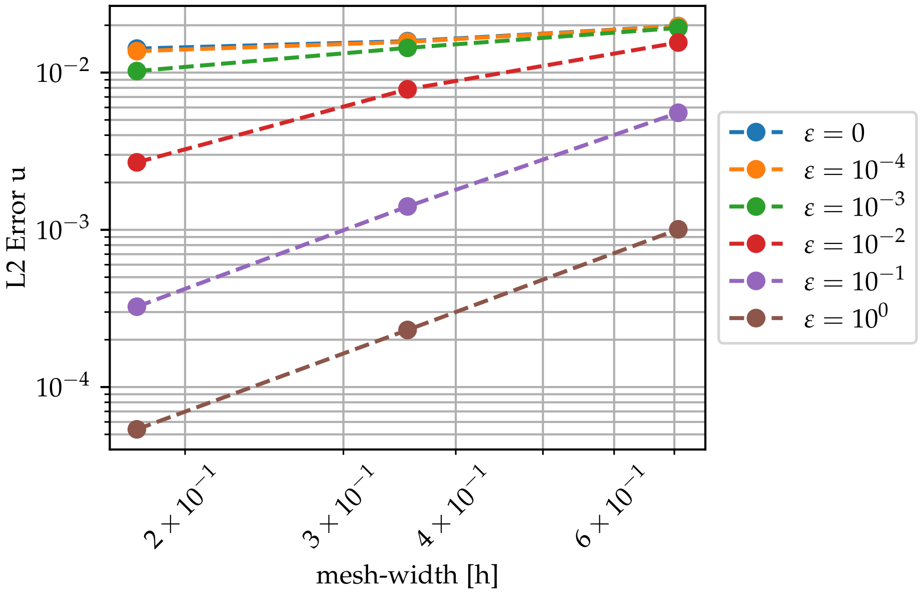

Figure C.1: Experiment 1 performed using partial scheme E using a CFL condition of $\sqrt{\frac{1}{5}}$ on a simplicial mesh for varying viscosities ε and fixed conductivity $\sigma = \infty$.

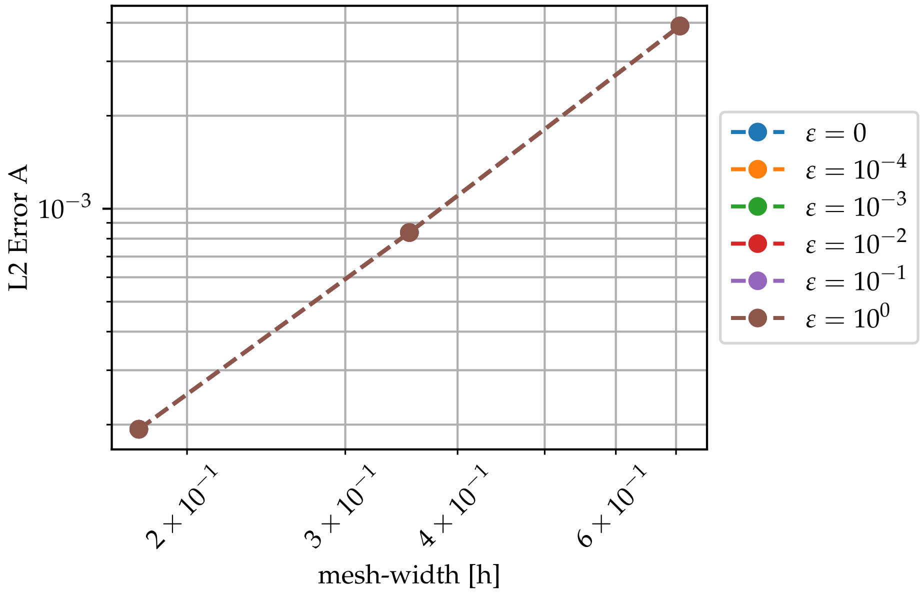

Figure C.2: Experiment 1 performed using partial scheme E using a CFL condition of $\sqrt{\frac{1}{5}}$ on a simplicial mesh for varying viscosities ε and fixed conductivity $\sigma = \infty$.

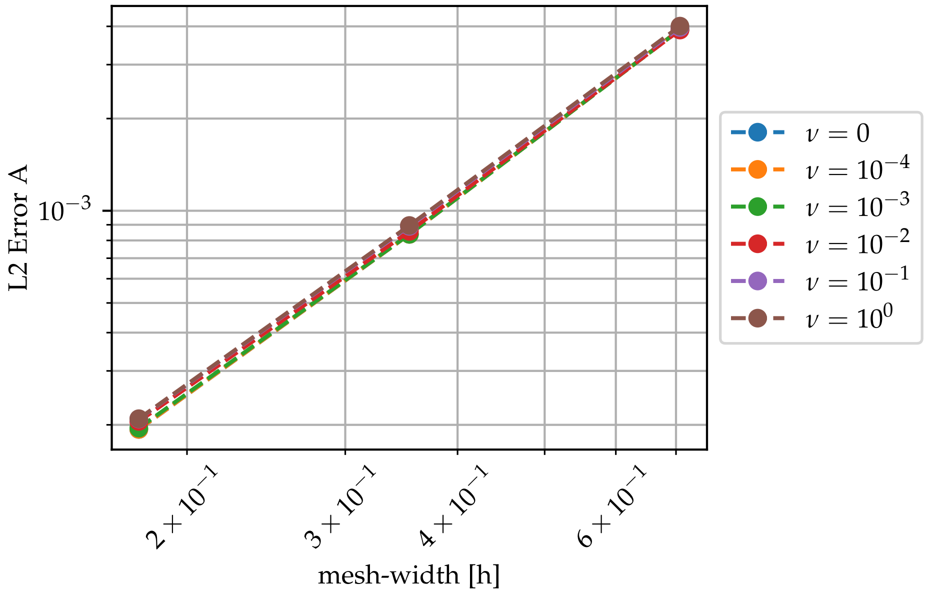

Figure C.3: Experiment 1 performed using partial scheme E using a CFL condition of $\sqrt{\frac{1}{5}}$ on a simplicial mesh for fixed viscosity $\varepsilon = 0$ and varying values for the conductivity $\sigma = \frac{1}{\nu}$.

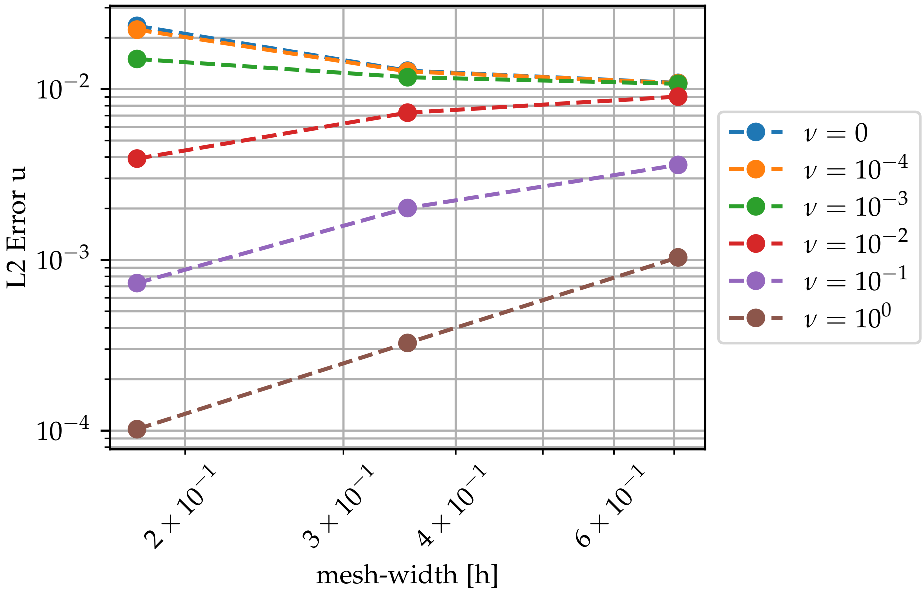

Figure C.4: Experiment 1 performed using scheme A using a CFL condition of $\sqrt{\frac{1}{5}}$ on a simplicial mesh for fixed viscosity $\varepsilon = 0$ and varying values for the conductivity $\sigma = \frac{1}{\nu}$.

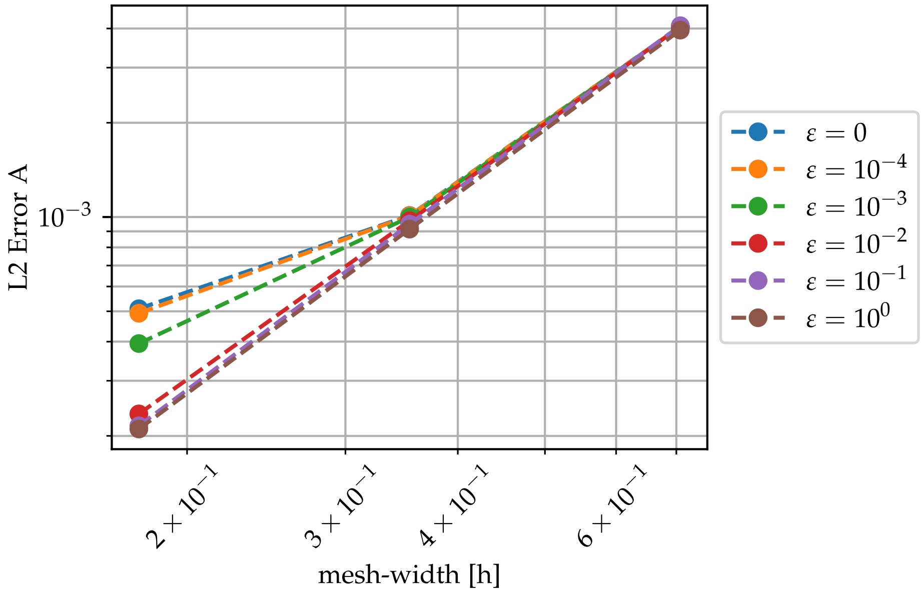

Figure C.5: Experiment 1 performed using scheme A using a CFL condition of $\sqrt{\frac{1}{5}}$ on a simplicial mesh for varying viscosities ε and fixed conductivity $\sigma = \infty$.

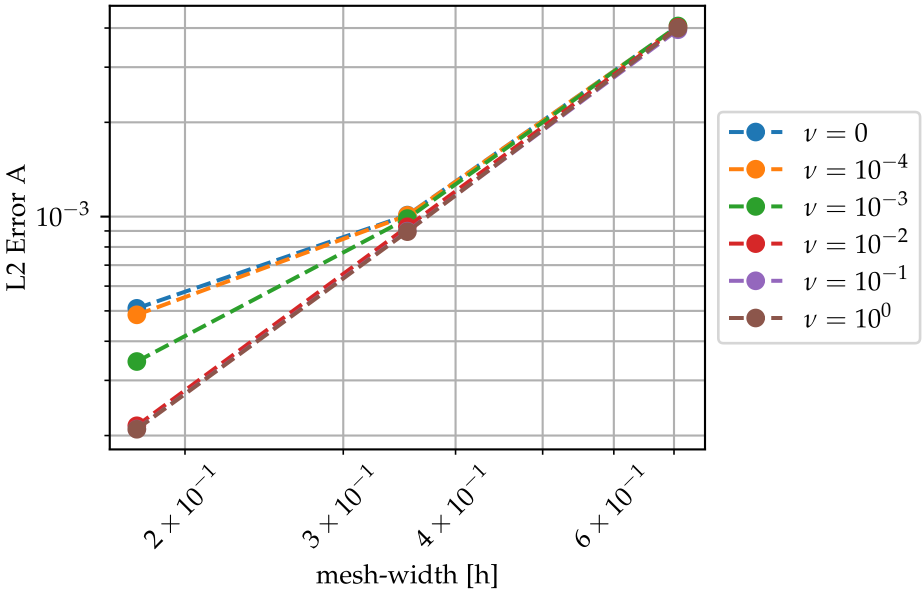

Figure C.6: Experiment 1 performed using scheme A using a CFL condition of $\sqrt{\frac{1}{5}}$ on a simplicial mesh for fixed viscosity $\varepsilon = 0$ and varying values for the conductivity $\sigma = \frac{1}{\nu}$.

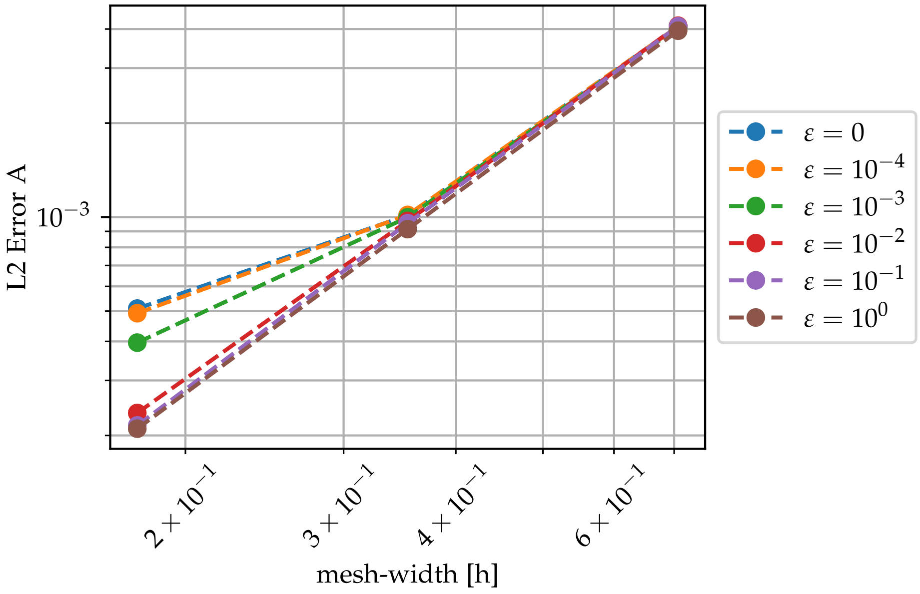

Figure C.7: Experiment 1 performed using partial scheme C using a CFL condition of $\sqrt{\frac{1}{5}}$ on a simplicial mesh for varying viscosities ε and fixed conductivity $\sigma = \infty$.

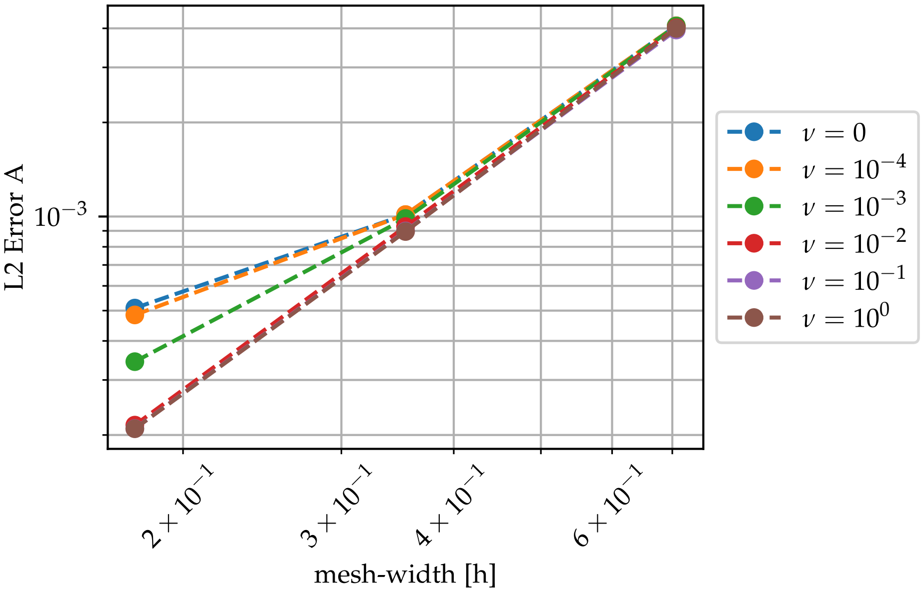

Figure C.8: Experiment 1 performed using partial scheme C using a CFL condition of $\sqrt{\frac{1}{5}}$ on a simplicial mesh for fixed viscosity $\varepsilon = 0$ and varying values for the conductivity $\sigma = \frac{1}{\nu}$.

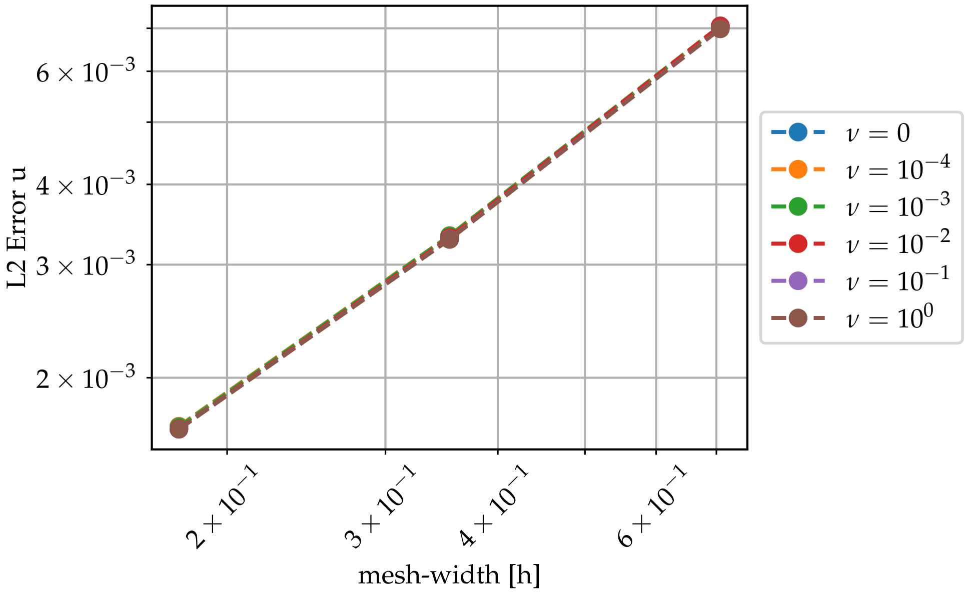

Figure C.9: Experiment 1 performed using partial scheme B using a CFL condition of $\sqrt{\frac{1}{5}}$ on a simplicial mesh for fixed viscosity $\varepsilon = 0$ and varying values for the conductivity $\sigma = \frac{1}{\nu}$.

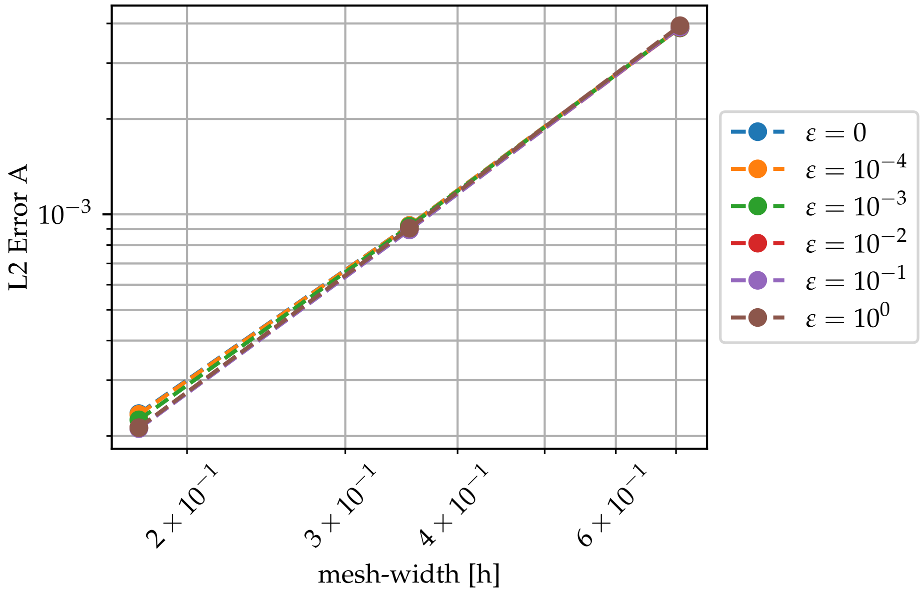

Figure C.10: Experiment 1 performed using partial scheme B using a CFL condition of $\sqrt{\frac{1}{5}}$ on a simplicial mesh for varying viscosities ε and fixed conductivity $\sigma = \infty$.

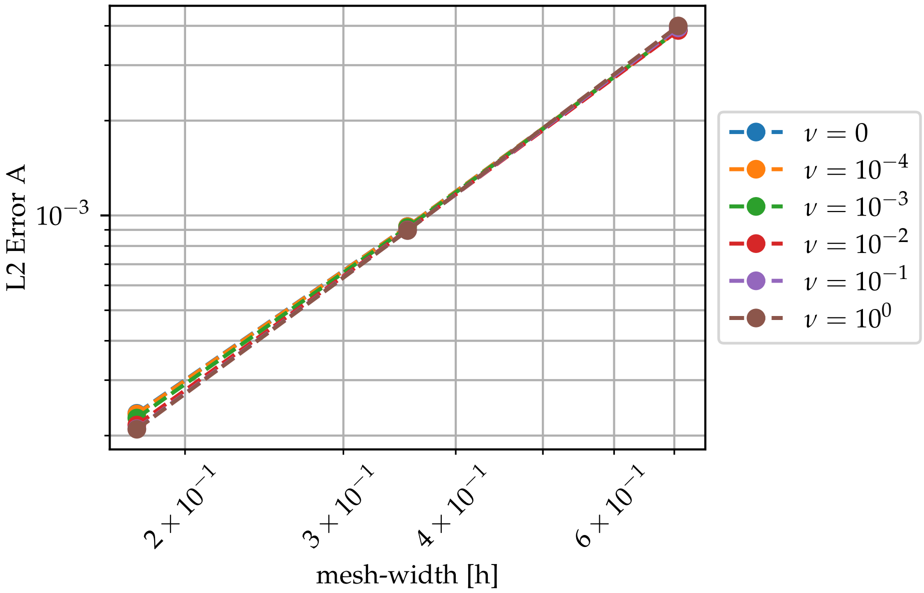

Figure C.11: Experiment 1 performed using partial scheme B using a CFL condition of $\sqrt{\frac{1}{5}}$ on a simplicial mesh for fixed viscosity $\varepsilon = 0$ and varying values for the conductivity $\sigma = \frac{1}{\nu}$.

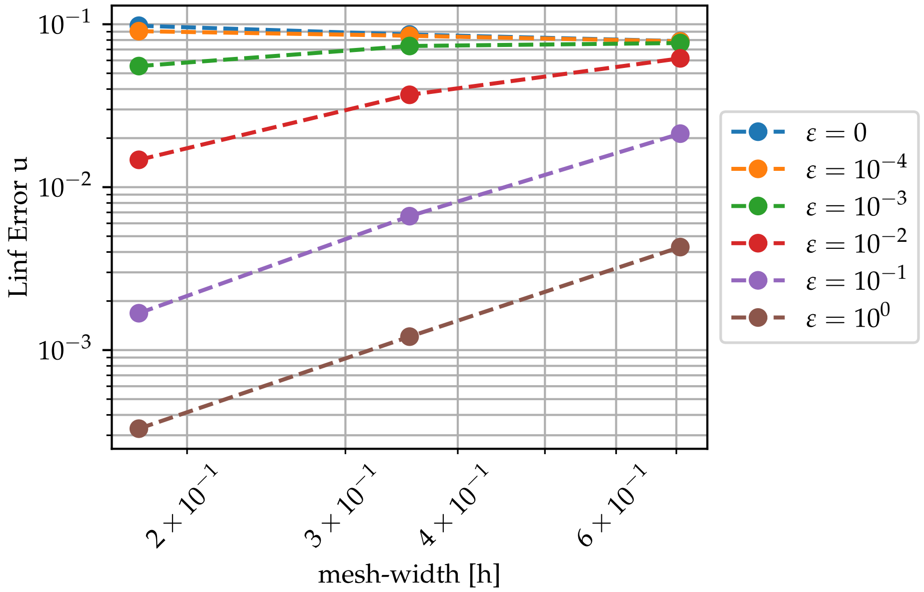

Figure C.12: Experiment 1 performed using partial scheme E using a CFL condition of $\sqrt{\frac{1}{5}}$ on a simplicial mesh for varying viscosities ε and fixed conductivity $\sigma = \infty$.

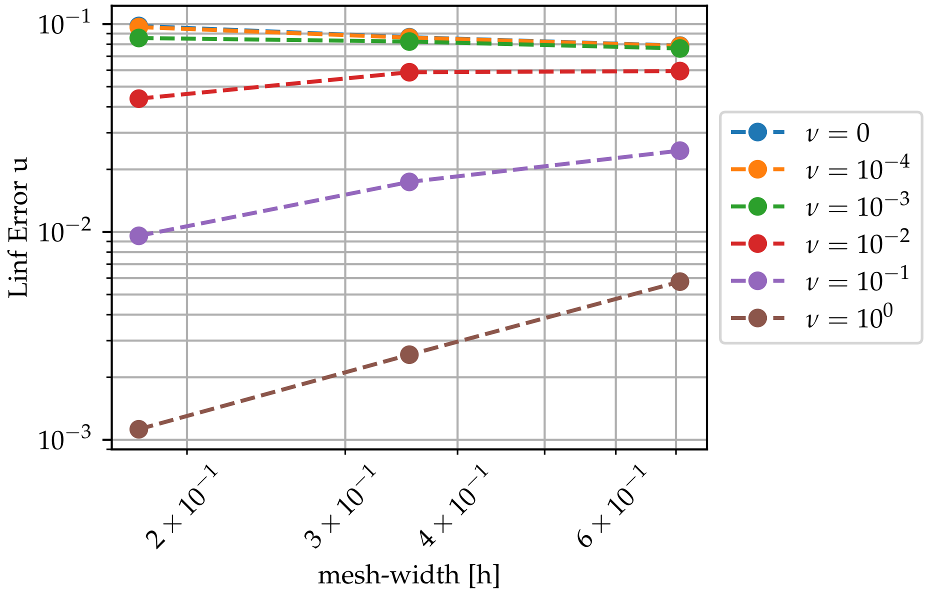

Figure C.13: Experiment 1 performed using partial scheme E using a CFL condition of $\sqrt{\frac{1}{5}}$ on a simplicial mesh for fixed viscosity $\varepsilon = 0$ and varying values for the conductivity $\sigma = \frac{1}{\nu}$.

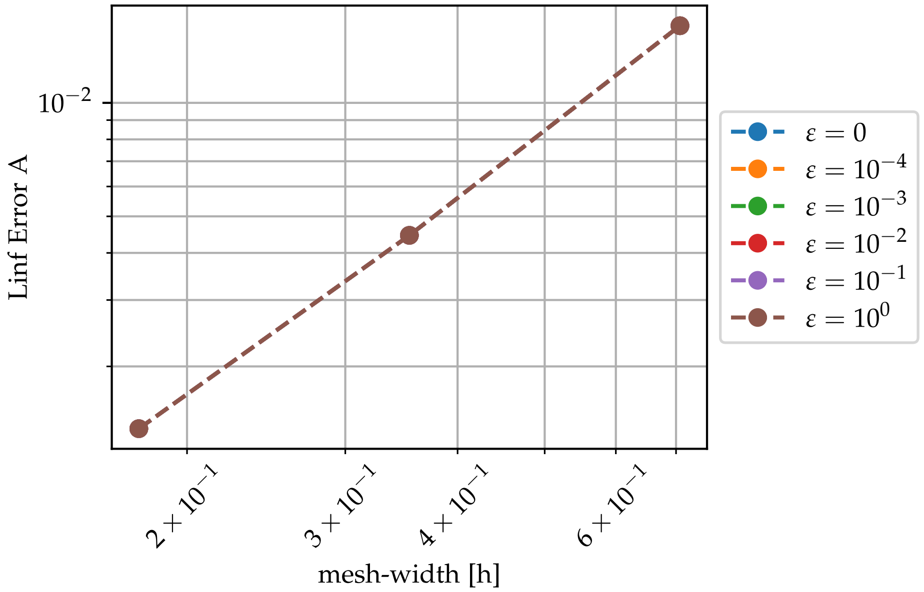

Figure C.14: Experiment 1 performed using partial scheme E using a CFL condition of $\sqrt{\frac{1}{5}}$ on a simplicial mesh for varying viscosities ε and fixed conductivity $\sigma = \infty$.

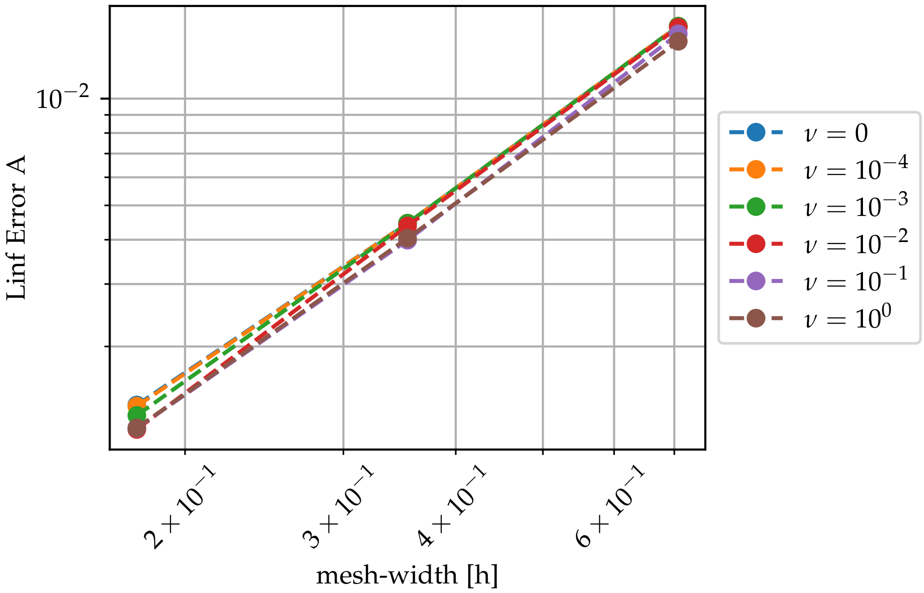

Figure C.15: Experiment 1 performed using partial scheme E using a CFL condition of $\sqrt{\frac{1}{5}}$ on a simplicial mesh for fixed viscosity $\varepsilon = 0$ and varying values for the conductivity $\sigma = \frac{1}{\nu}$.

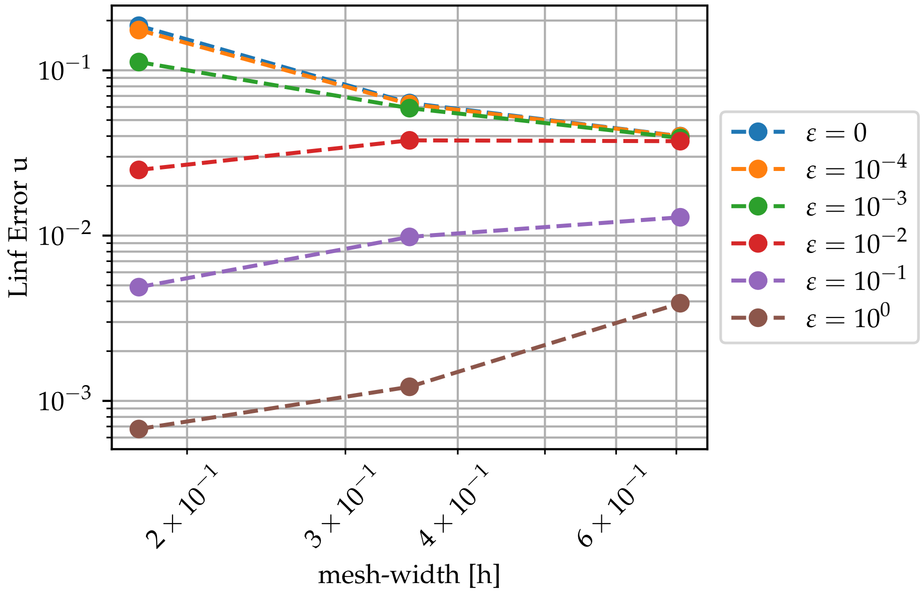

Figure C.16: Experiment 1 performed using scheme A using a CFL condition of $\sqrt{\frac{1}{5}}$ on a simplicial mesh for varying viscosities ε and fixed conductivity $\sigma = \infty$.

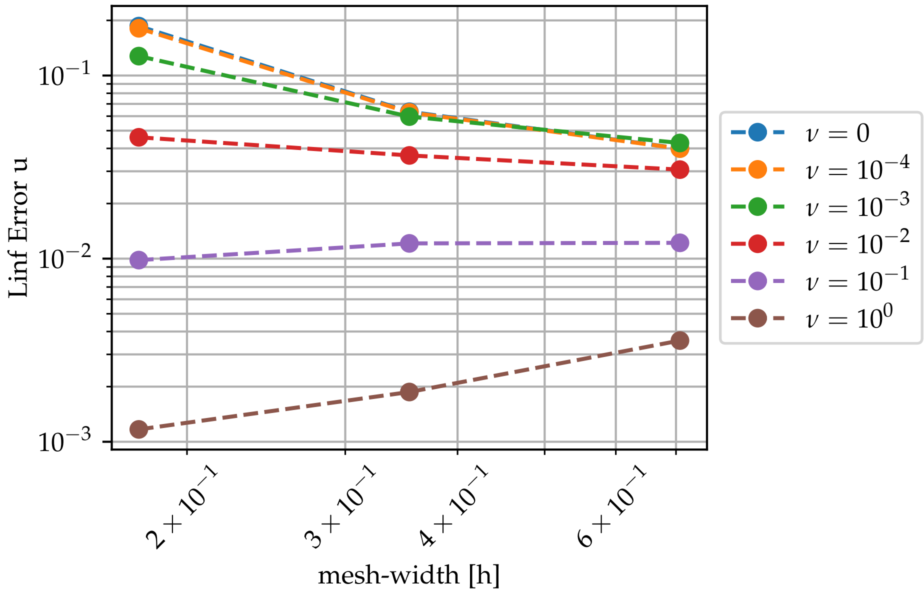

Figure C.17: Experiment 1 performed using scheme A using a CFL condition of $\sqrt{\frac{1}{5}}$ on a simplicial mesh for fixed viscosity $\varepsilon = 0$ and varying values for the conductivity $\sigma = \frac{1}{\nu}$.

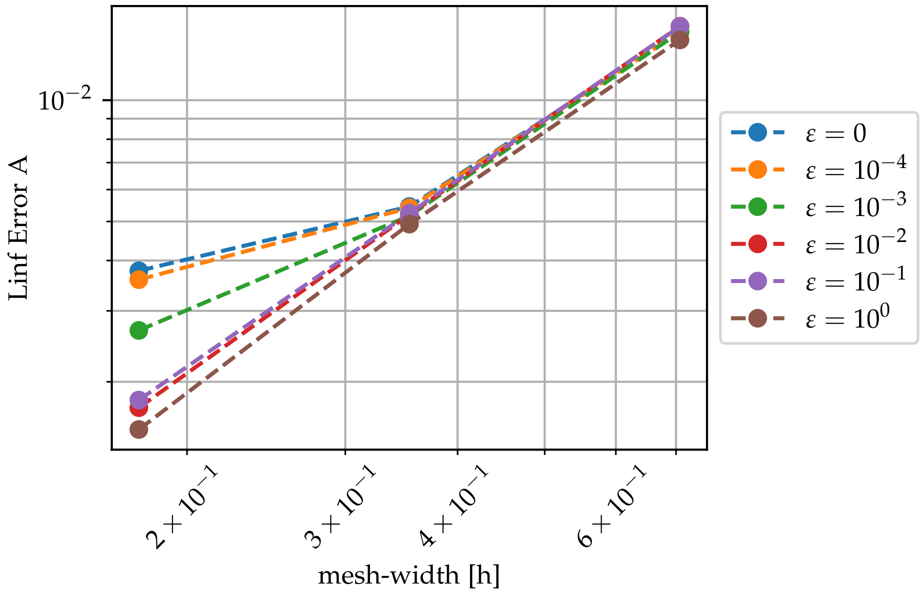

Figure C.18: Experiment 1 performed using scheme A using a CFL condition of $\sqrt{\frac{1}{5}}$ on a simplicial mesh for varying viscosities ε and fixed conductivity $\sigma = \infty$.

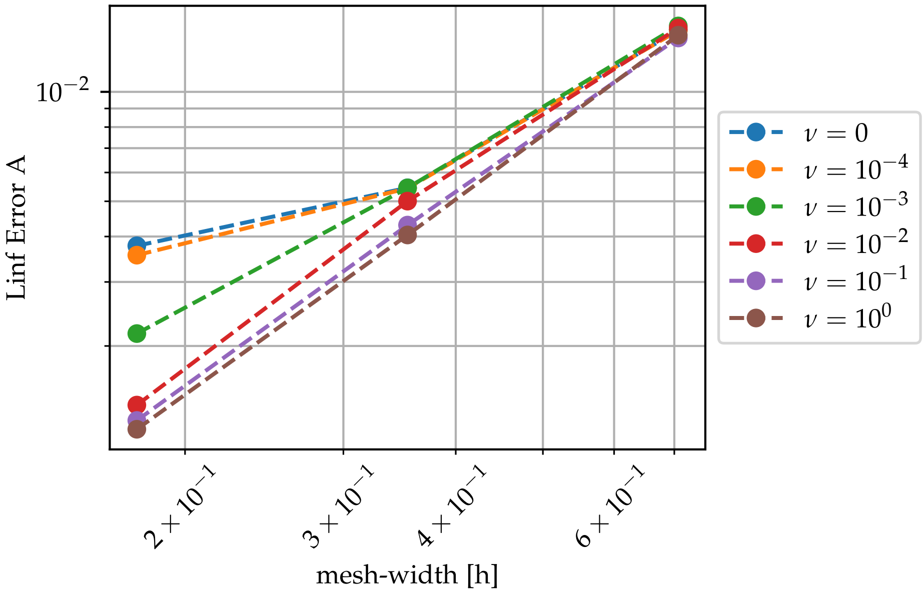

Figure C.19: Experiment 1 performed using scheme A using a CFL condition of $\sqrt{\frac{1}{5}}$ on a simplicial mesh for fixed viscosity $\varepsilon = 0$ and varying values for the conductivity $\sigma = \frac{1}{\nu}$.

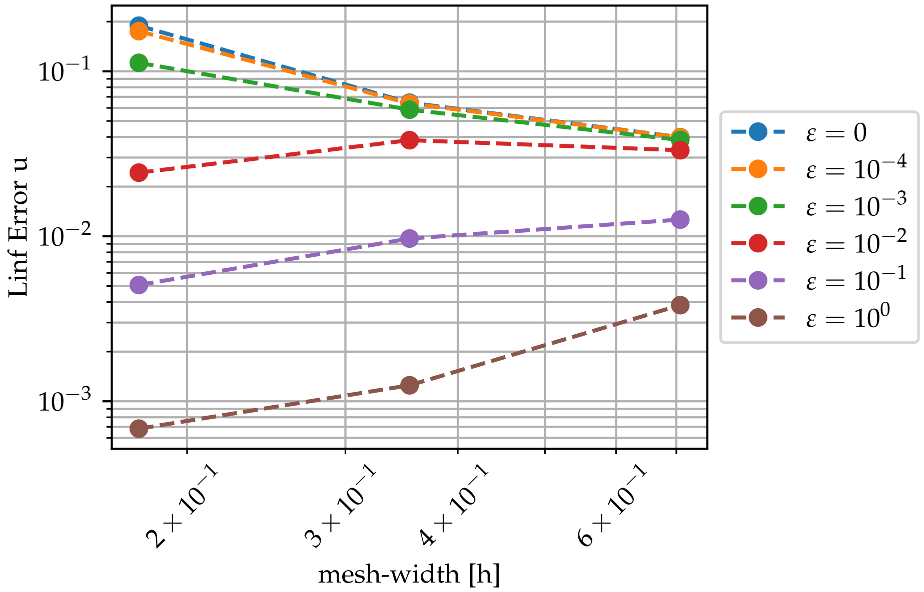

Figure C.20: Experiment 1 performed using partial scheme C using a CFL condition of $\sqrt{\frac{1}{5}}$ on a simplicial mesh for varying viscosities ε and fixed conductivity $\sigma = \infty$.

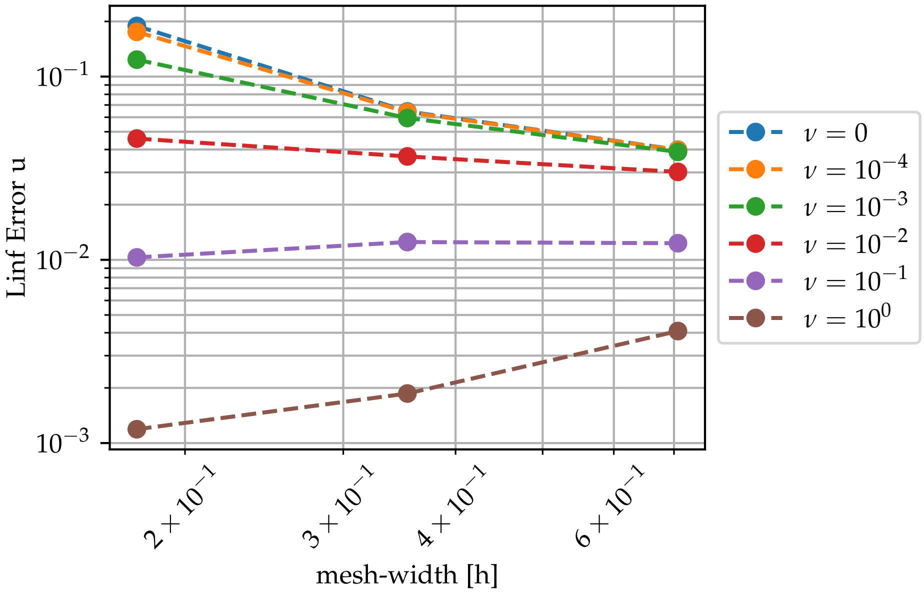

Figure C.21: Experiment 1 performed using partial scheme C using a CFL condition of $\sqrt{\frac{1}{5}}$ on a simplicial mesh for fixed viscosity $\varepsilon = 0$ and varying values for the conductivity $\sigma = \frac{1}{\nu}$.

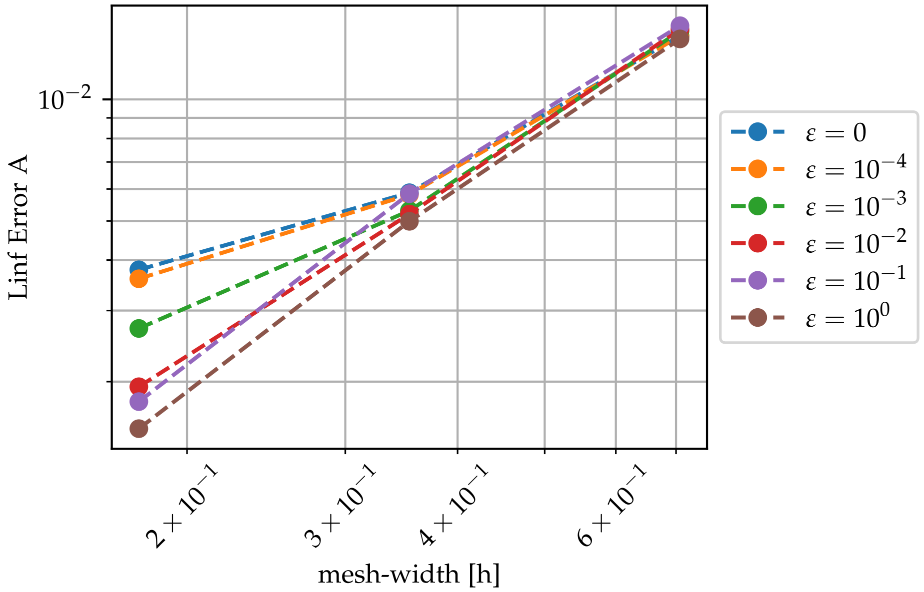

Figure C.22: Experiment 1 performed using partial scheme C using a CFL condition of $\sqrt{\frac{1}{5}}$ on a simplicial mesh for varying viscosities ε and fixed conductivity $\sigma = \infty$.

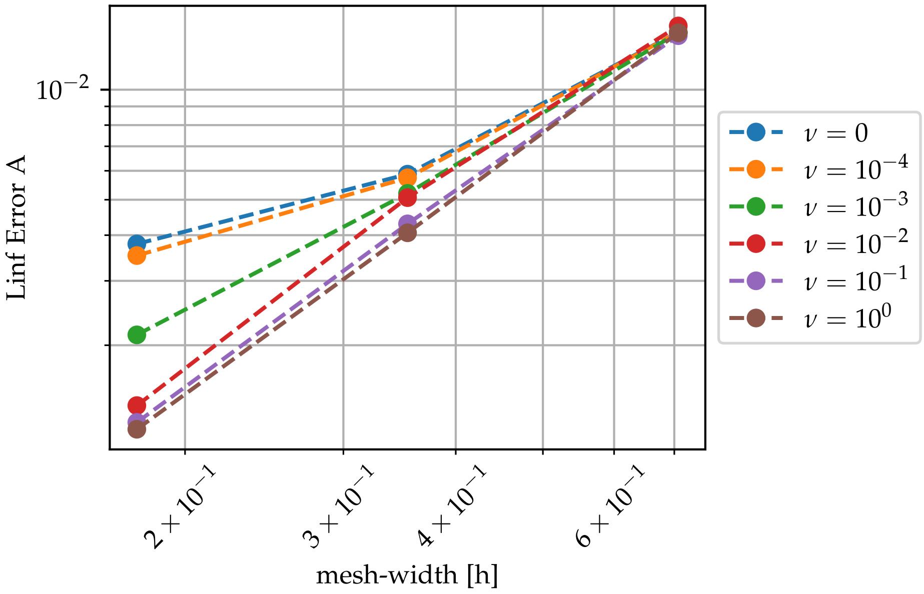

Figure C.23: Experiment 1 performed using partial scheme C using a CFL condition of $\sqrt{\frac{1}{5}}$ on a simplicial mesh for fixed viscosity $\varepsilon = 0$ and varying values for the conductivity $\sigma = \frac{1}{\nu}$.

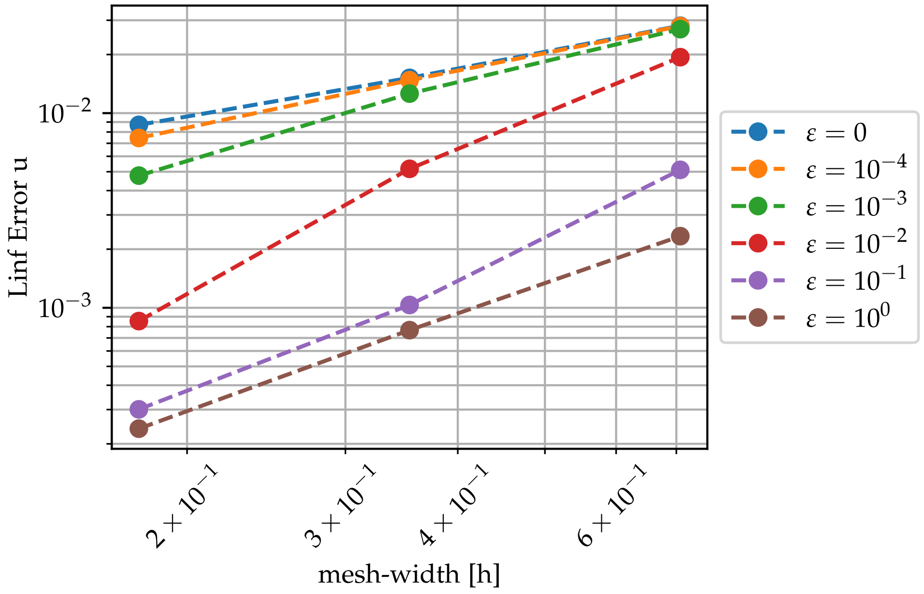

Figure C.24: Experiment 1 performed using partial scheme B using a CFL condition of $\sqrt{\frac{1}{5}}$ on a simplicial mesh for varying viscosities ε and fixed conductivity $\sigma = \infty$.

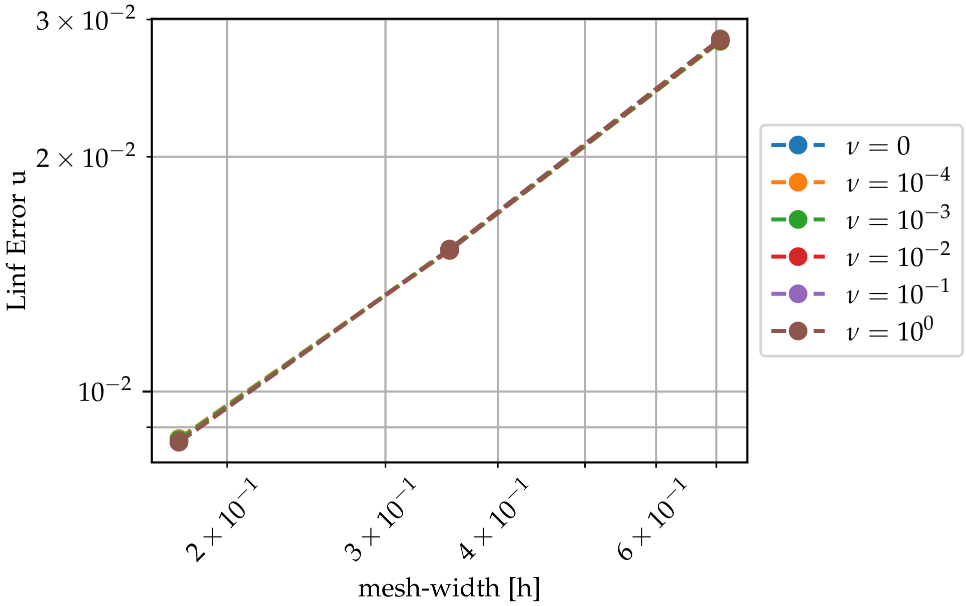

Figure C.25: Experiment 1 performed using partial scheme B using a CFL condition of $\sqrt{\frac{1}{5}}$ on a simplicial mesh for fixed viscosity $\varepsilon = 0$ and varying values for the conductivity $\sigma = \frac{1}{\nu}$.

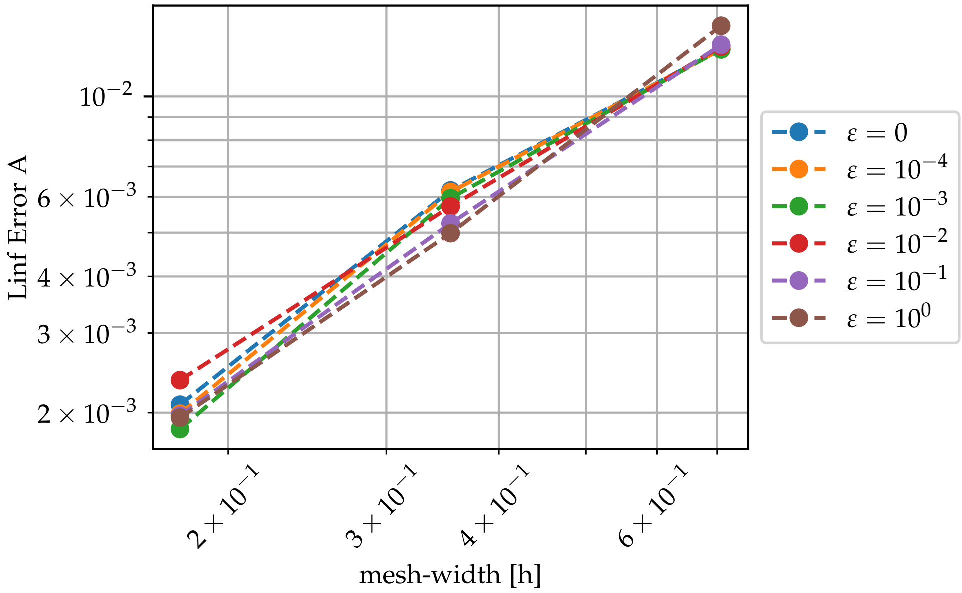

Figure C.26: Experiment 1 performed using partial scheme B using a CFL condition of $\sqrt{\frac{1}{5}}$ on a simplicial mesh for varying viscosities ε and fixed conductivity $\sigma = \infty$.

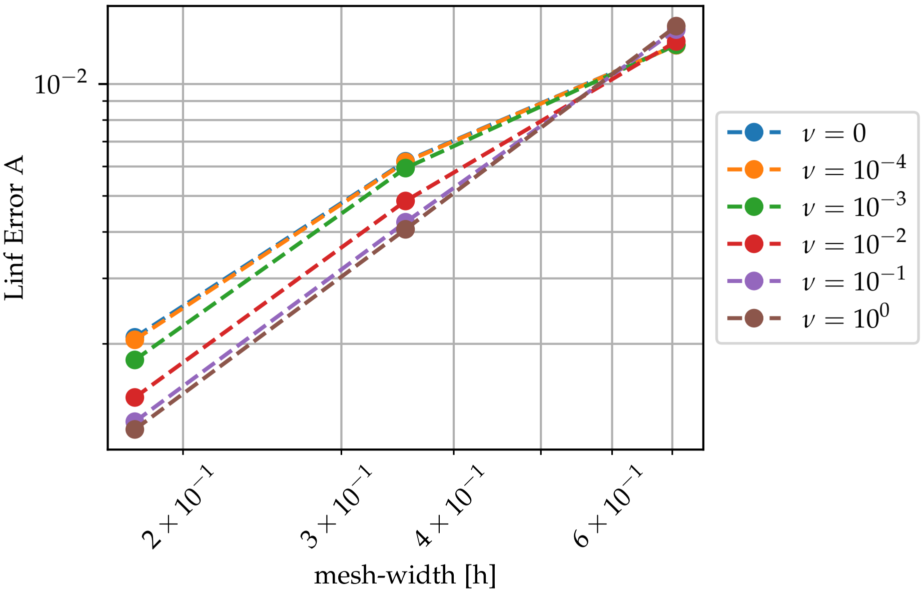

Figure C.27: Experiment 1 performed using partial scheme B using a CFL condition of $\sqrt{\frac{1}{5}}$ on a simplicial mesh for fixed viscosity $\varepsilon = 0$ and varying values for the conductivity $\sigma = \frac{1}{\nu}$.

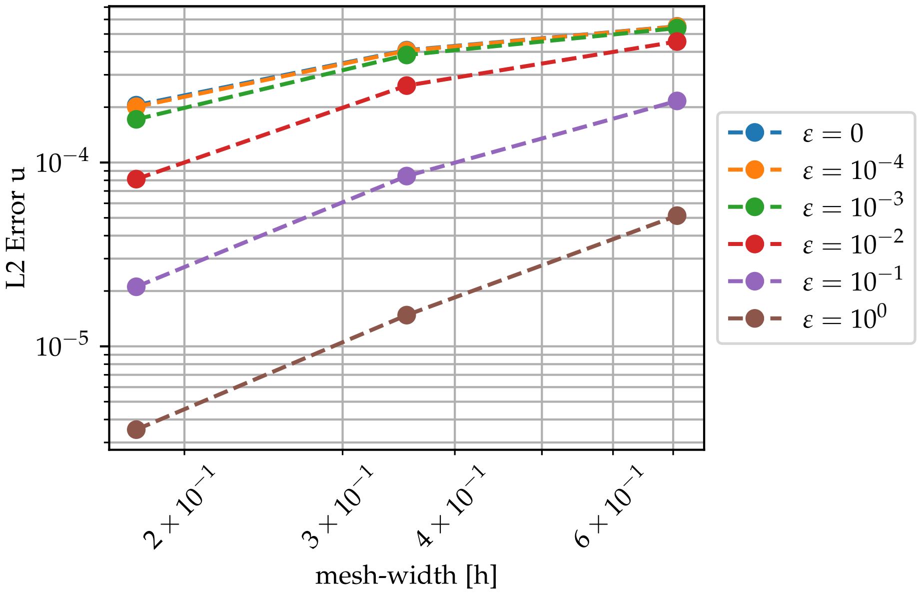

Figure C.28: Experiment 2 performed using partial scheme E using a CFL condition of $\sqrt{\frac{1}{20}}$ on a simplicial mesh for varying viscosities ε and fixed conductivity $\sigma = \infty$.

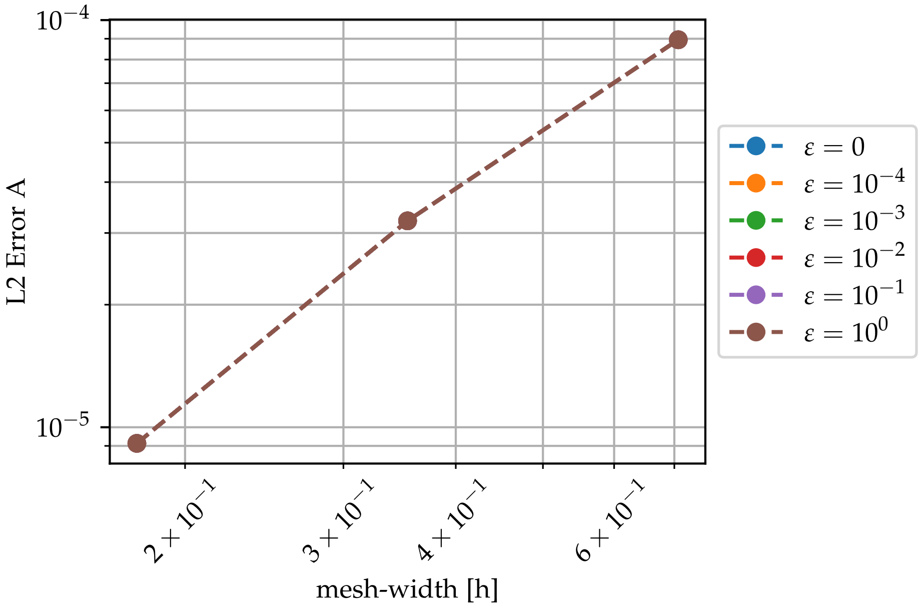

Figure C.29: Experiment 2 performed using partial scheme E using a CFL condition of $\sqrt{\frac{1}{20}}$ on a simplicial mesh for varying viscosities ε and fixed conductivity $\sigma = \infty$.

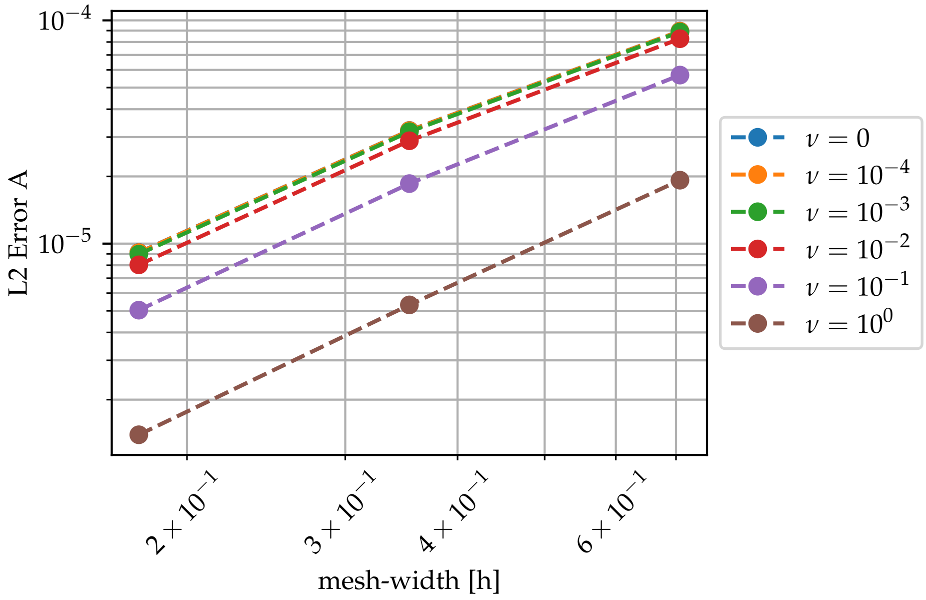

Figure C.30: Experiment 2 performed using partial scheme E using a CFL condition of $\sqrt{\frac{1}{20}}$ on a simplicial mesh for fixed viscosity $\varepsilon = 0$ and varying values for the conductivity $\sigma = \frac{1}{\nu}$.

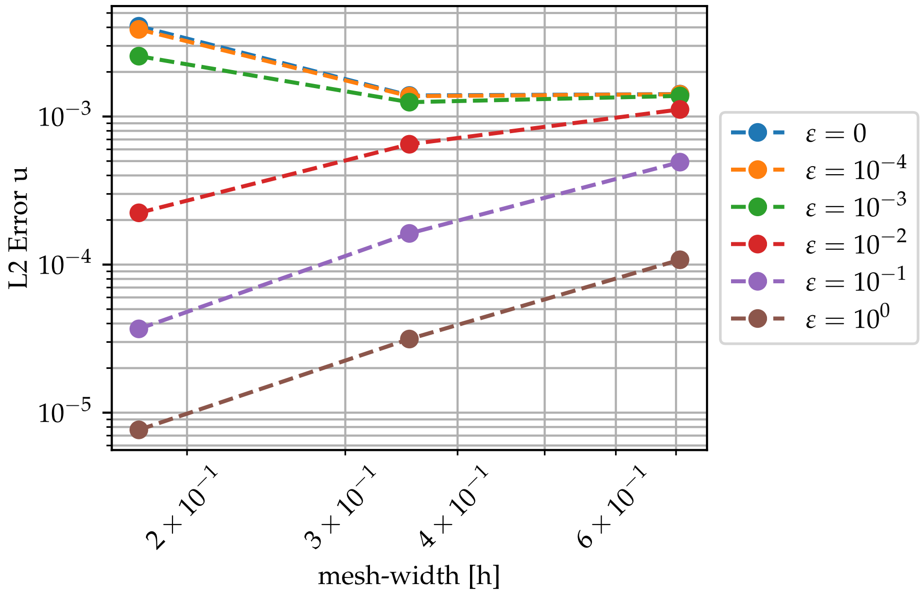

Figure C.31: Experiment 2 performed using scheme A using a CFL condition of $\sqrt{\frac{1}{20}}$ on a simplicial mesh for varying viscosities ε and fixed conductivity $\sigma = \infty$.

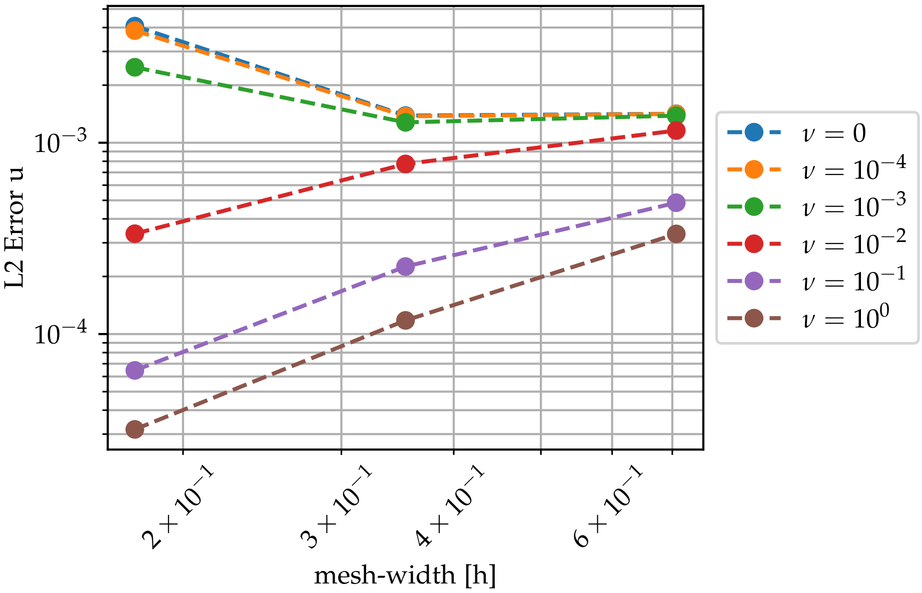

Figure C.32: Experiment 2 performed using scheme A using a CFL condition of $\sqrt{\frac{1}{20}}$ on a simplicial mesh for fixed viscosity $\varepsilon = 0$ and varying values for the conductivity $\sigma = \frac{1}{\nu}$.

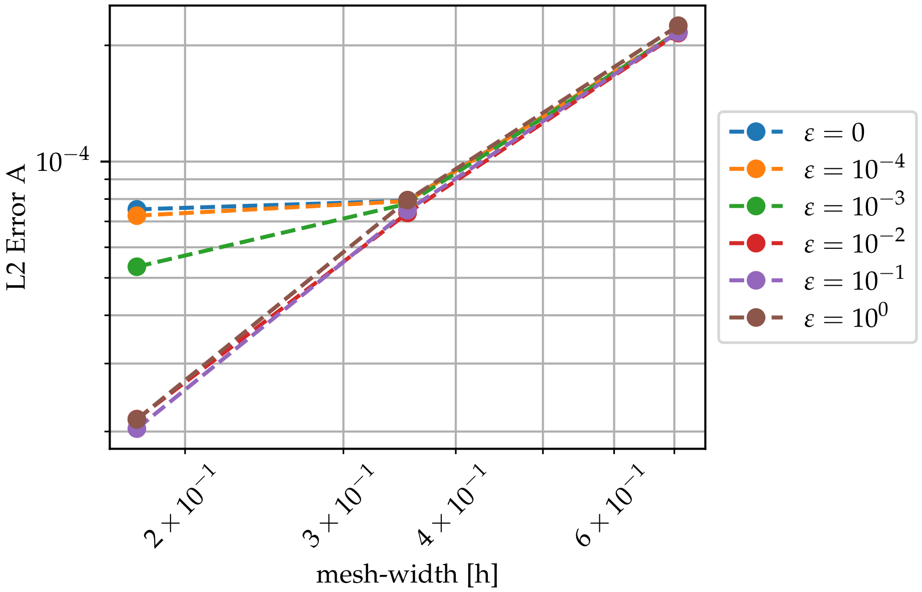

Figure C.33: Experiment 2 performed using scheme A using a CFL condition of $\sqrt{\frac{1}{20}}$ on a simplicial mesh for varying viscosities ε and fixed conductivity $\sigma = \infty$.

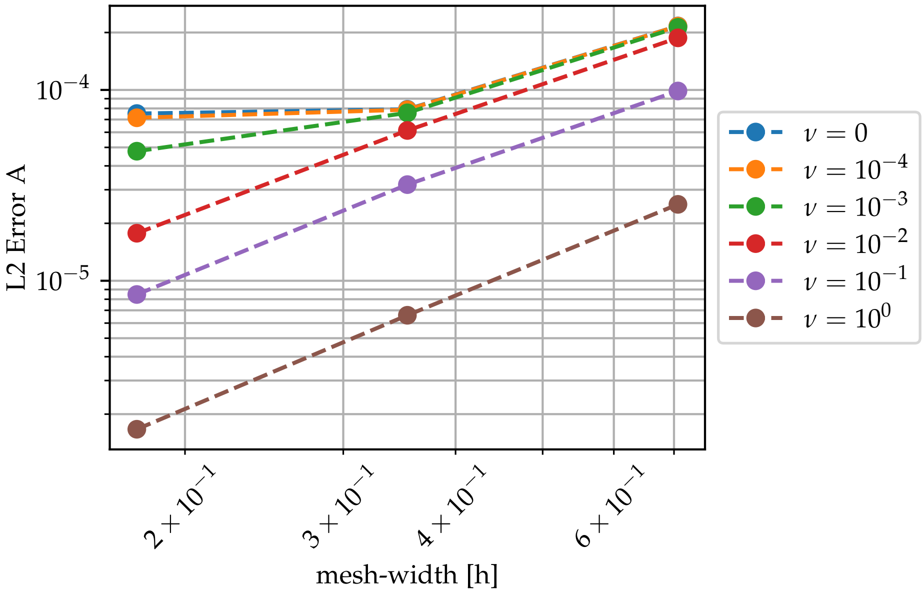

Figure C.34: Experiment 2 performed using scheme A using a CFL condition of $\sqrt{\frac{1}{20}}$ on a simplicial mesh for fixed viscosity $\varepsilon = 0$ and varying values for the conductivity $\sigma = \frac{1}{\nu}$.

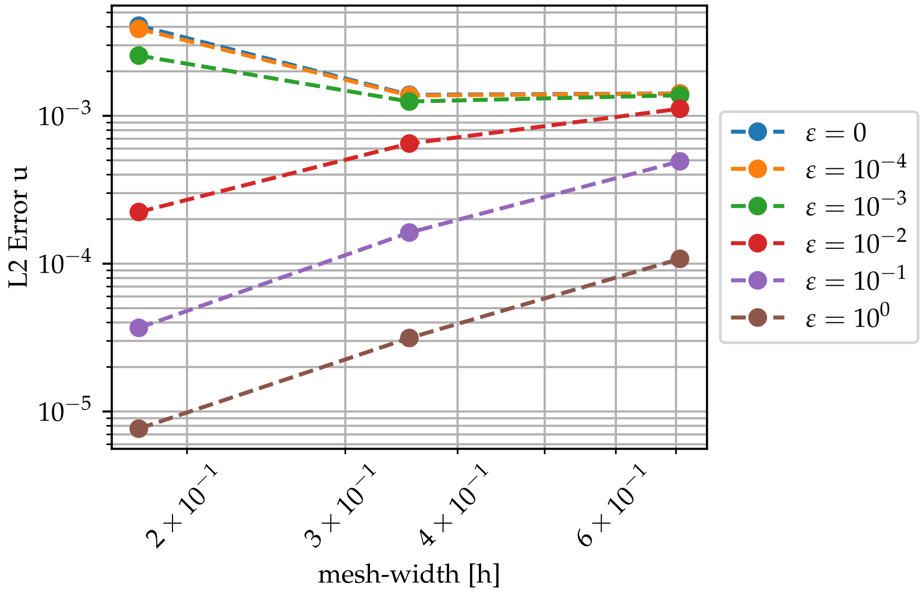

Figure C.35: Experiment 2 performed using partial scheme C using a CFL condition of $\sqrt{\frac{1}{20}}$ on a simplicial mesh for varying viscosities ε and fixed conductivity $\sigma = \infty$.

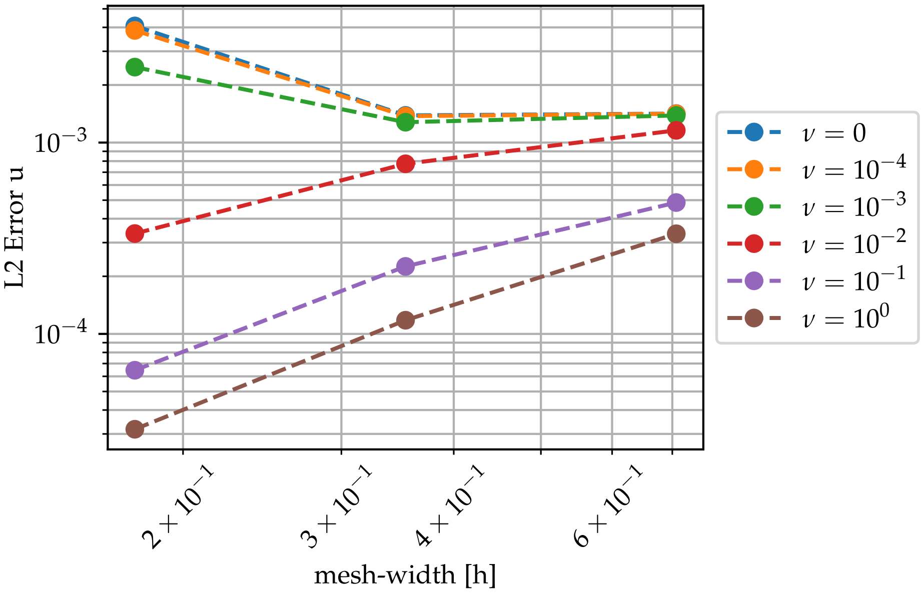

Figure C.36: Experiment 2 performed using partial scheme C using a CFL condition of $\sqrt{\frac{1}{20}}$ on a simplicial mesh for fixed viscosity $\varepsilon = 0$ and varying values for the conductivity $\sigma = \frac{1}{\nu}$.

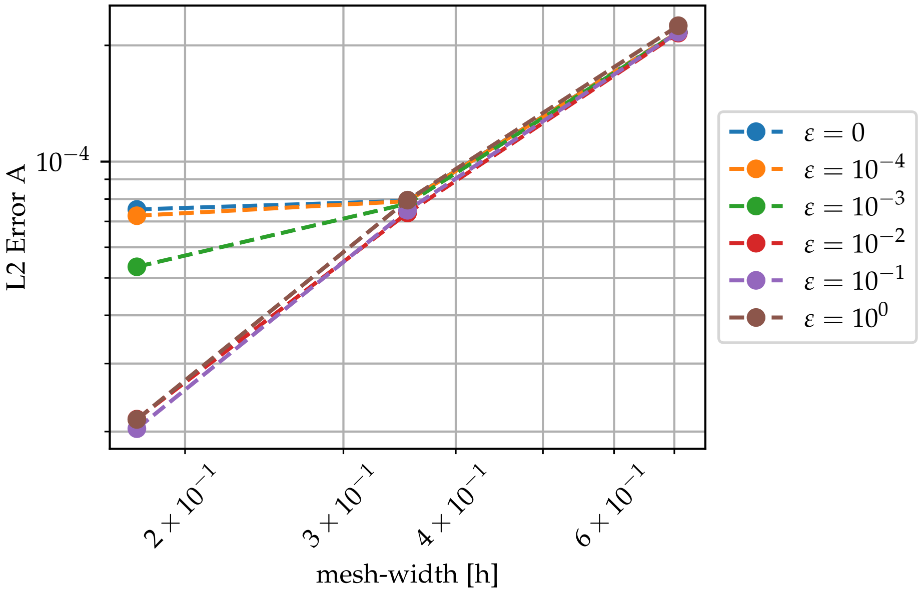

Figure C.37: Experiment 2 performed using partial scheme C using a CFL condition of $\sqrt{\frac{1}{20}}$ on a simplicial mesh for varying viscosities ε and fixed conductivity $\sigma = \infty$.

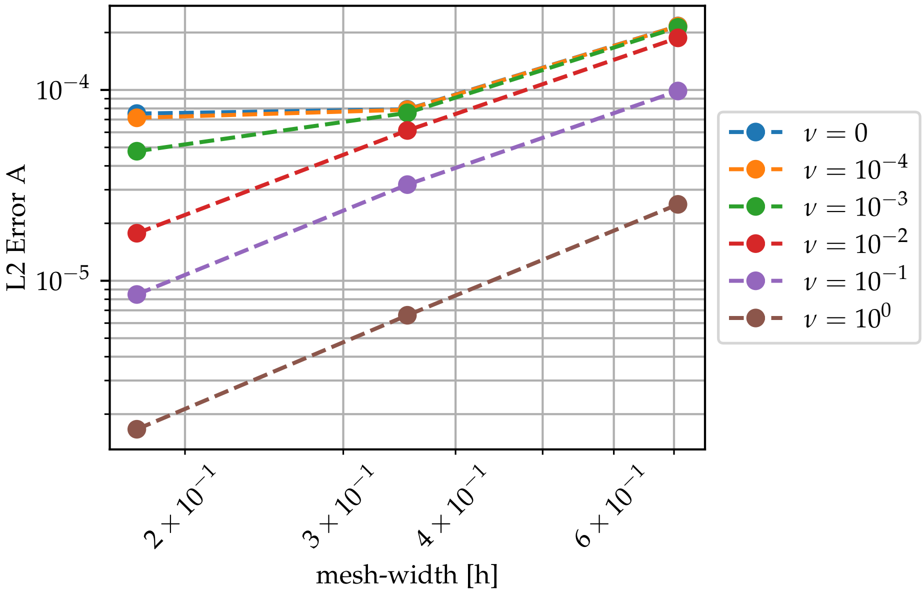

Figure C.38: Experiment 2 performed using partial scheme C using a CFL condition of $\sqrt{\frac{1}{20}}$ on a simplicial mesh for fixed viscosity $\varepsilon = 0$ and varying values for the conductivity $\sigma = \frac{1}{\nu}$.

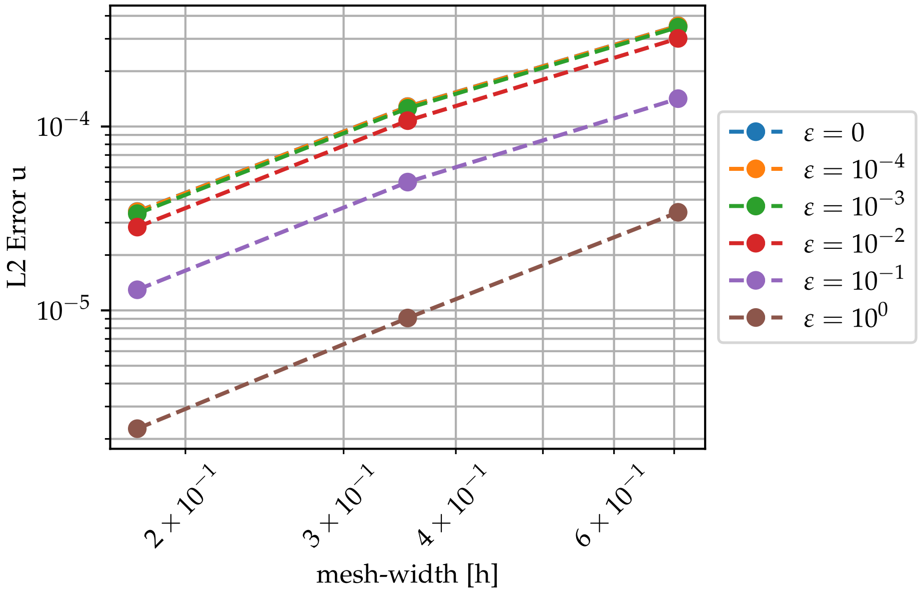

Figure C.39: Experiment 2 performed using partial scheme B using a CFL condition of $\sqrt{\frac{1}{20}}$ on a simplicial mesh for varying viscosities ε and fixed conductivity $\sigma = \infty$.

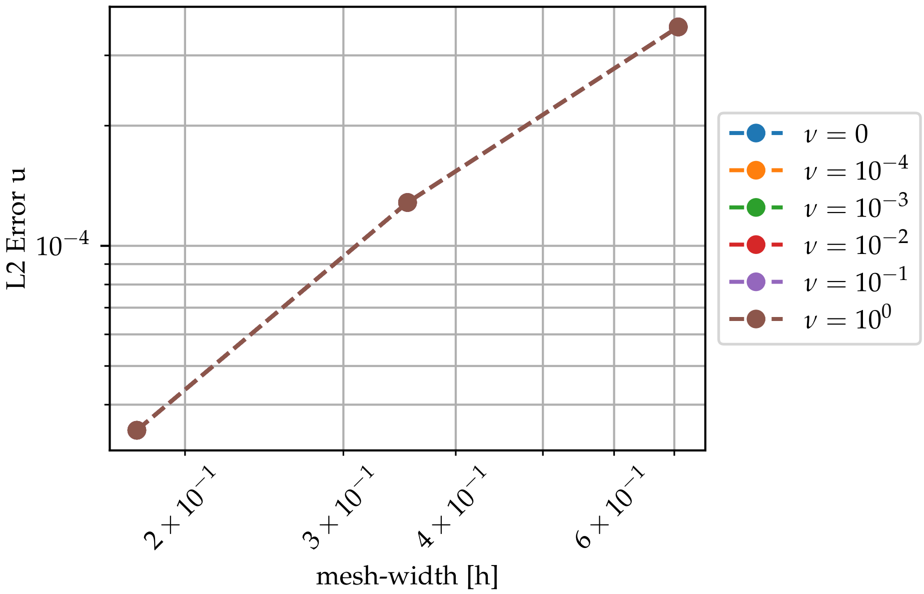

Figure C.40: Experiment 2 performed using partial scheme B using a CFL condition of $\sqrt{\frac{1}{20}}$ on a simplicial mesh for fixed viscosity $\varepsilon = 0$ and varying values for the conductivity $\sigma = \frac{1}{\nu}$.

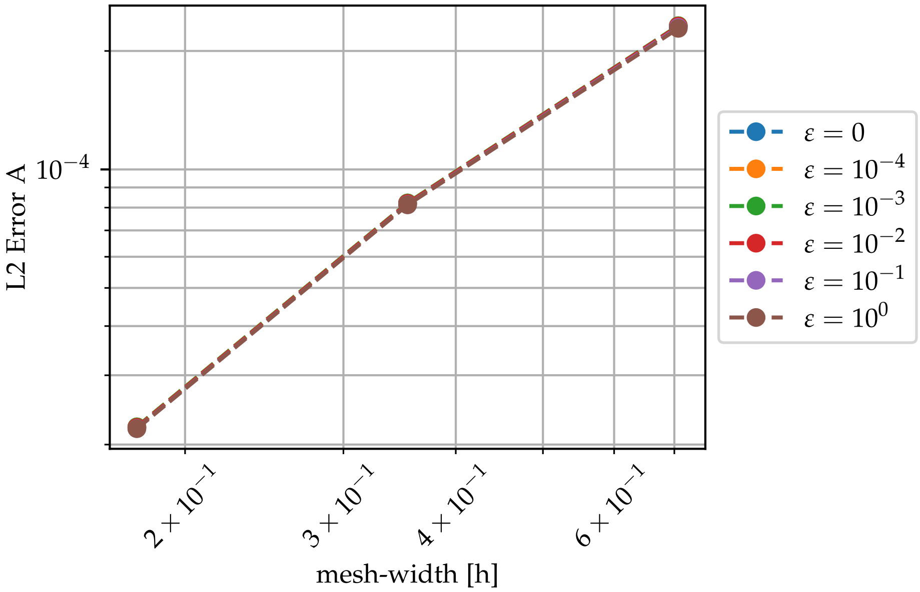

Figure C.41: Experiment 2 performed using partial scheme B using a CFL condition of $\sqrt{\frac{1}{20}}$ on a simplicial mesh for varying viscosities ε and fixed conductivity $\sigma = \infty$.

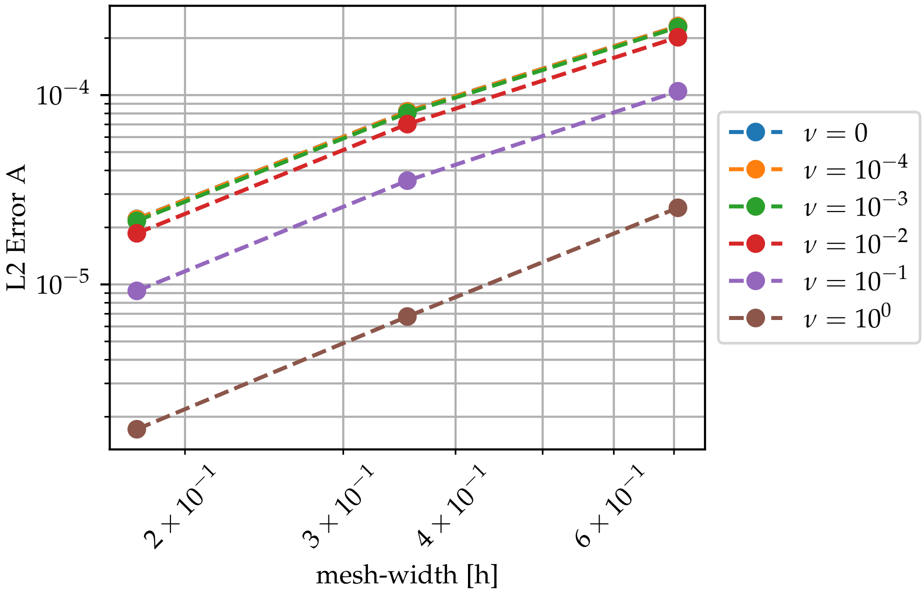

Figure C.42: Experiment 2 performed using partial scheme B using a CFL condition of $\sqrt{\frac{1}{20}}$ on a simplicial mesh for fixed viscosity $\varepsilon = 0$ and varying values for the conductivity $\sigma = \frac{1}{\nu}$.

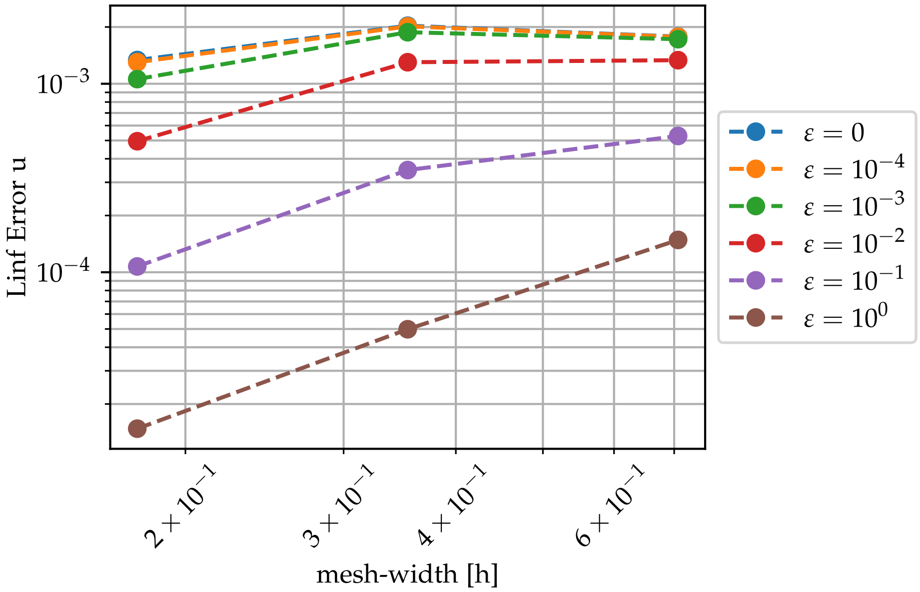

Figure C.43: Experiment 1 performed using partial scheme E using a CFL condition of $\sqrt{\frac{1}{20}}$ on a simplicial mesh for varying viscosities ε and fixed conductivity $\sigma = \infty$.

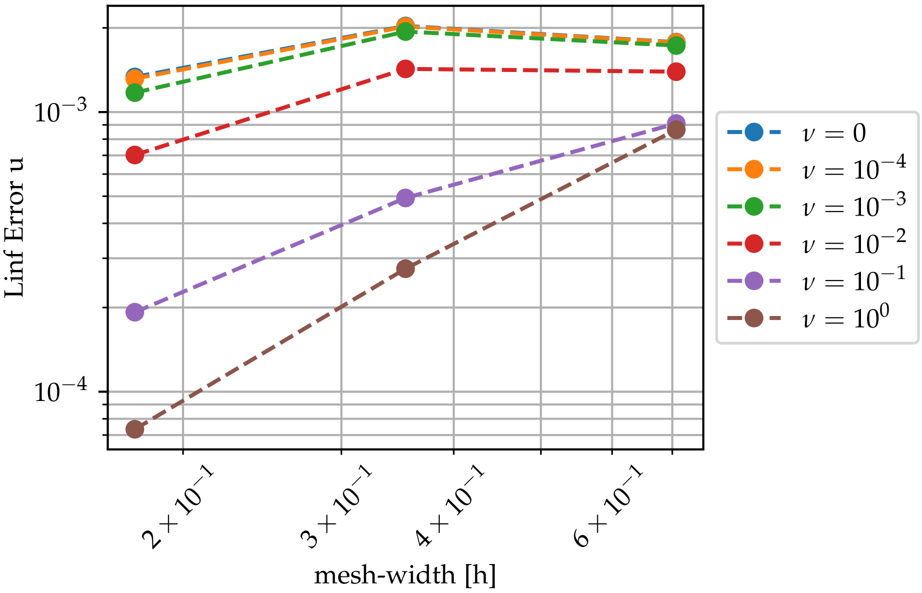

Figure C.44: Experiment 1 performed using partial scheme E using a CFL condition of $\sqrt{\frac{1}{20}}$ on a simplicial mesh for fixed viscosity $\varepsilon = 0$ and varying values for the conductivity $\sigma = \frac{1}{\nu}$.

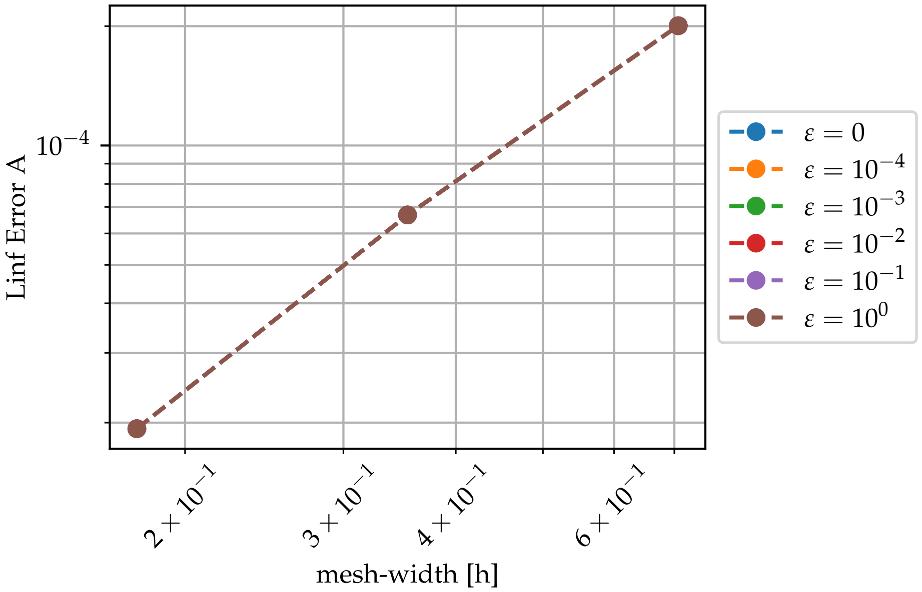

Figure C.45: Experiment 1 performed using partial scheme E using a CFL condition of $\sqrt{\frac{1}{20}}$ on a simplicial mesh for varying viscosities ε and fixed conductivity $\sigma = \infty$.

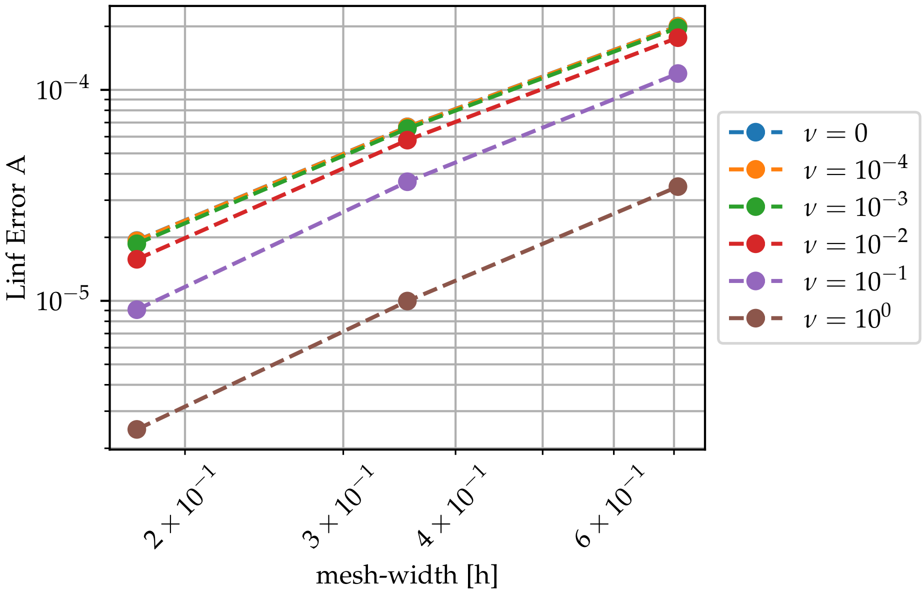

Figure C.46: Experiment 1 performed using partial scheme E using a CFL condition of $\sqrt{\frac{1}{20}}$ on a simplicial mesh for fixed viscosity $\varepsilon = 0$ and varying values for the conductivity $\sigma = \frac{1}{\nu}$.

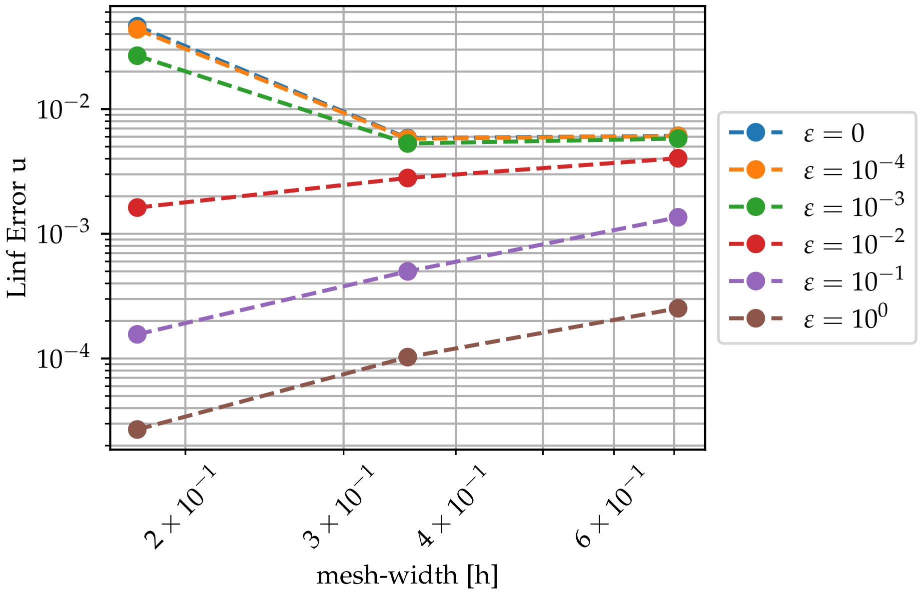

Figure C.47: Experiment 1 performed using scheme A using a CFL condition of $\sqrt{\frac{1}{20}}$ on a simplicial mesh for varying viscosities ε and fixed conductivity $\sigma = \infty$.

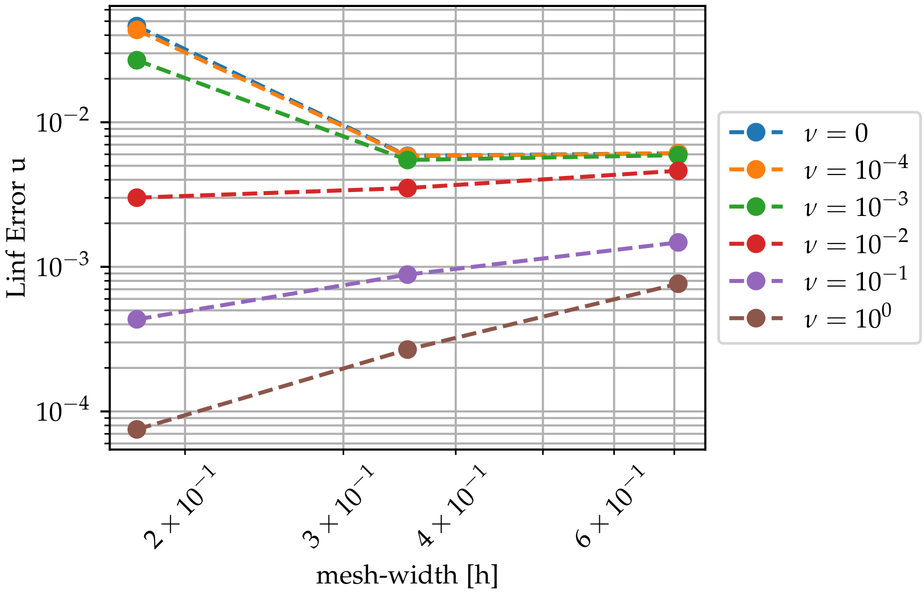

Figure C.48: Experiment 1 performed using scheme A using a CFL condition of $\sqrt{\frac{1}{20}}$ on a simplicial mesh for fixed viscosity $\varepsilon = 0$ and varying values for the conductivity $\sigma = \frac{1}{\nu}$.

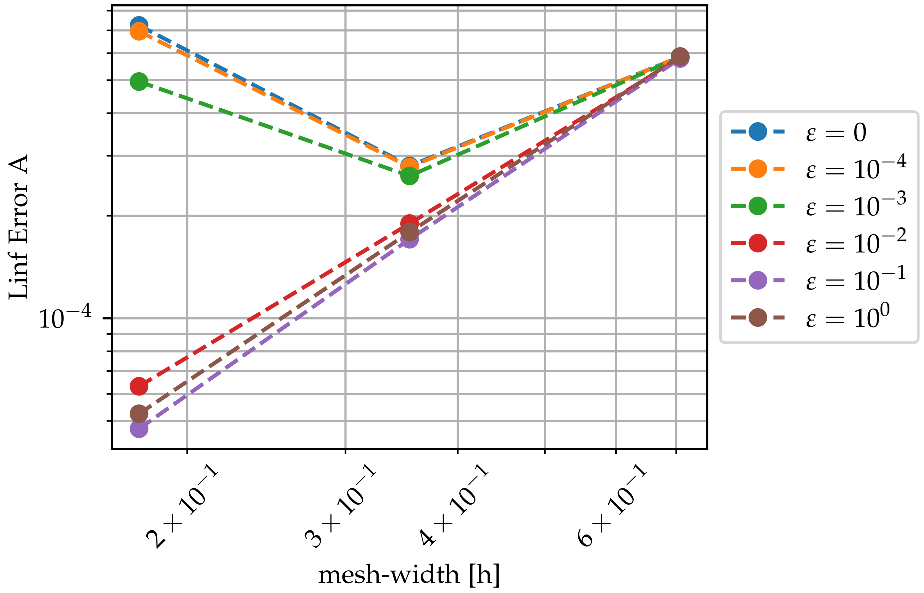

Figure C.49: Experiment 1 performed using scheme A using a CFL condition of $\sqrt{\frac{1}{20}}$ on a simplicial mesh for varying viscosities ε and fixed conductivity $\sigma = \infty$.

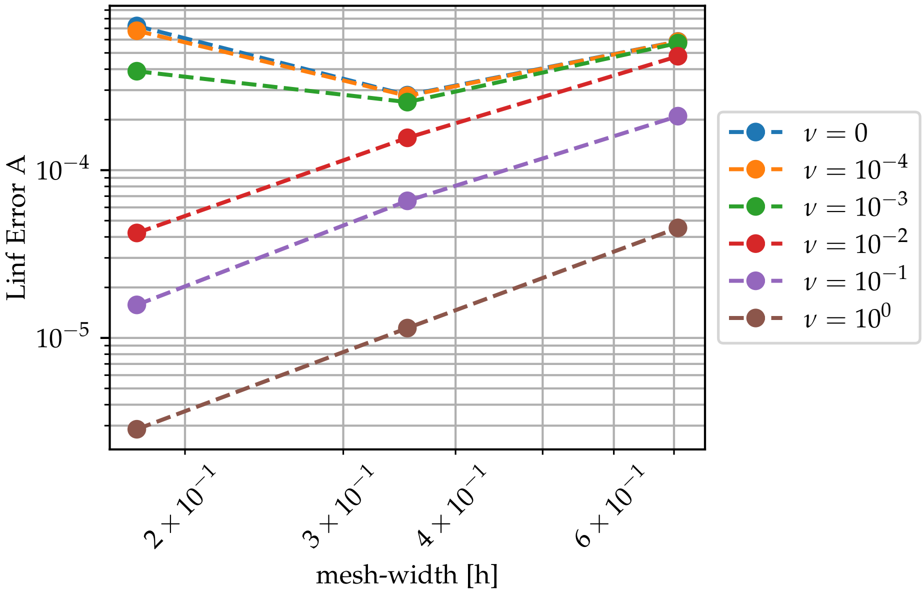

Figure C.50: Experiment 1 performed using scheme A using a CFL condition of $\sqrt{\frac{1}{20}}$ on a simplicial mesh for fixed viscosity $\varepsilon = 0$ and varying values for the conductivity $\sigma = \frac{1}{\nu}$.

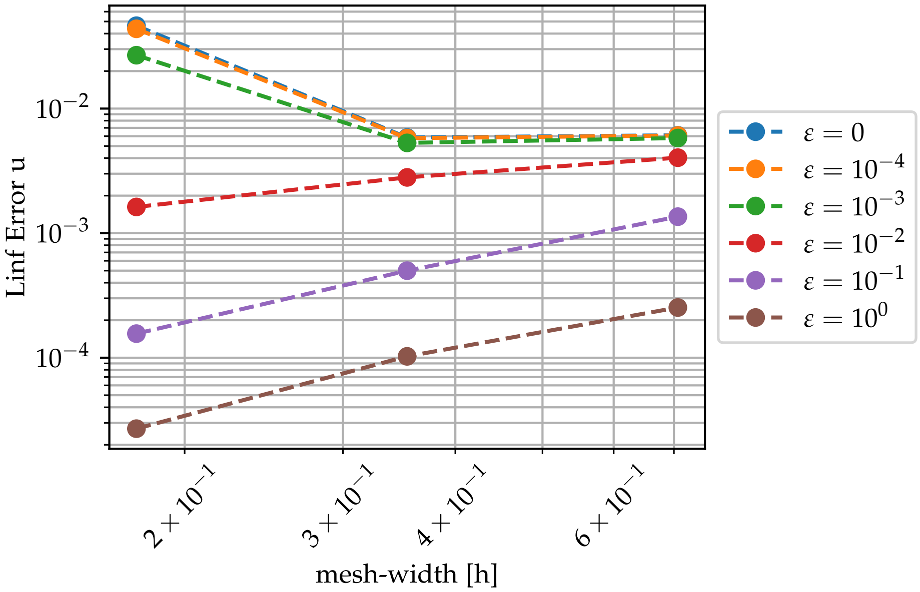

Figure C.51: Experiment 1 performed using partial scheme C using a CFL condition of $\sqrt{\frac{1}{20}}$ on a simplicial mesh for varying viscosities ε and fixed conductivity $\sigma = \infty$.

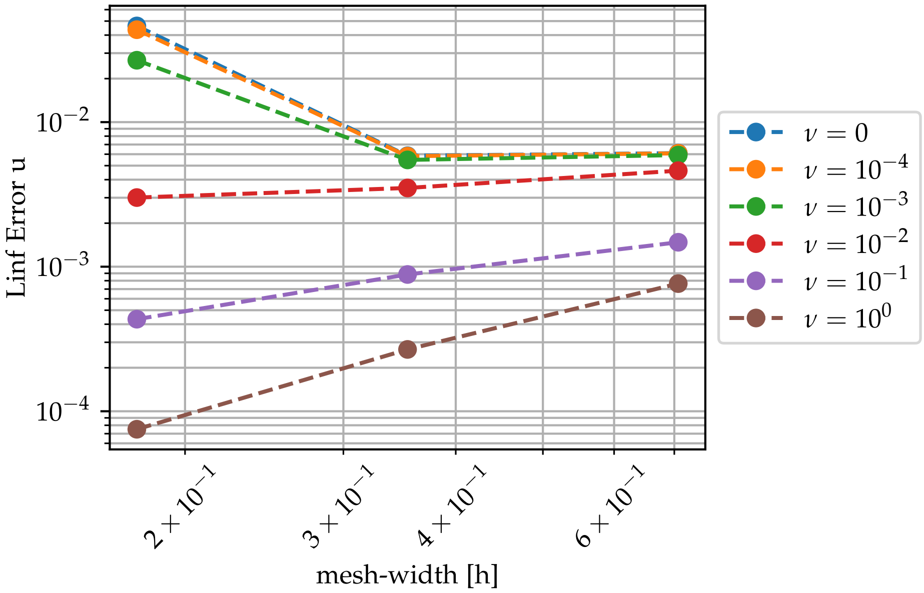

Figure C.52: Experiment 1 performed using partial scheme C using a CFL condition of $\sqrt{\frac{1}{20}}$ on a simplicial mesh for fixed viscosity $\varepsilon = 0$ and varying values for the conductivity $\sigma = \frac{1}{\nu}$.

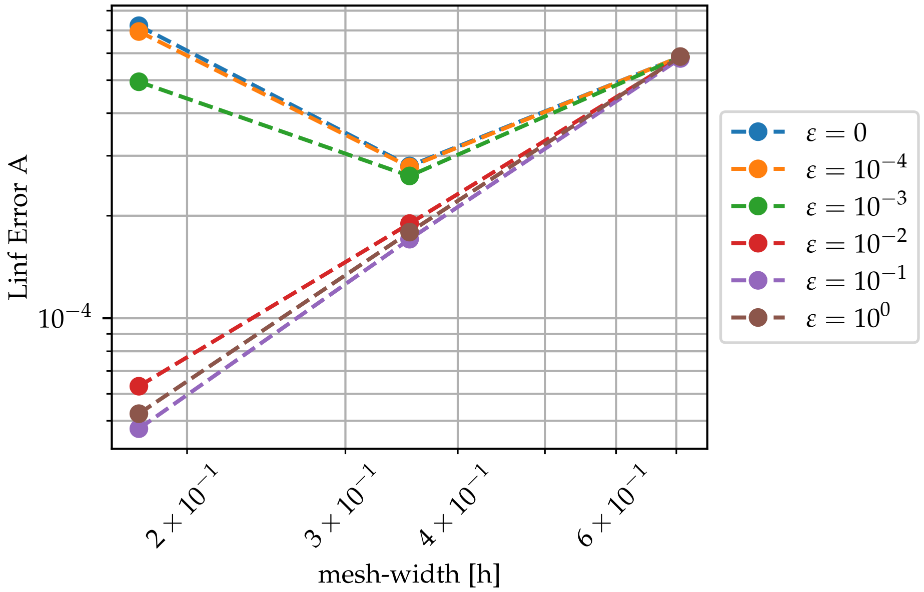

Figure C.53: Experiment 1 performed using partial scheme C using a CFL condition of $\sqrt{\frac{1}{20}}$ on a simplicial mesh for varying viscosities ε and fixed conductivity $\sigma = \infty$.

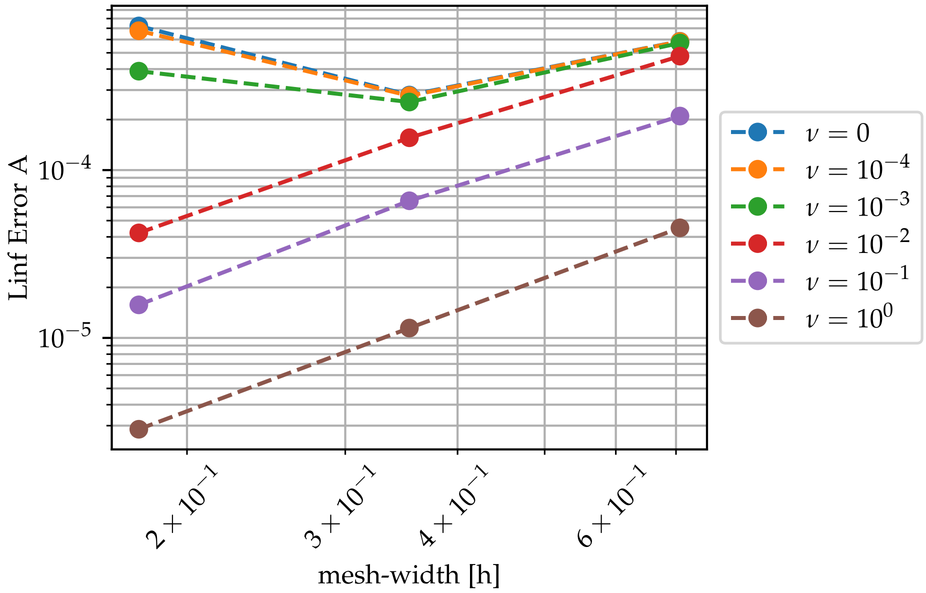

Figure C.54: Experiment 1 performed using partial scheme C using a CFL condition of $\sqrt{\frac{1}{20}}$ on a simplicial mesh for fixed viscosity $\varepsilon = 0$ and varying values for the conductivity $\sigma = \frac{1}{\nu}$.

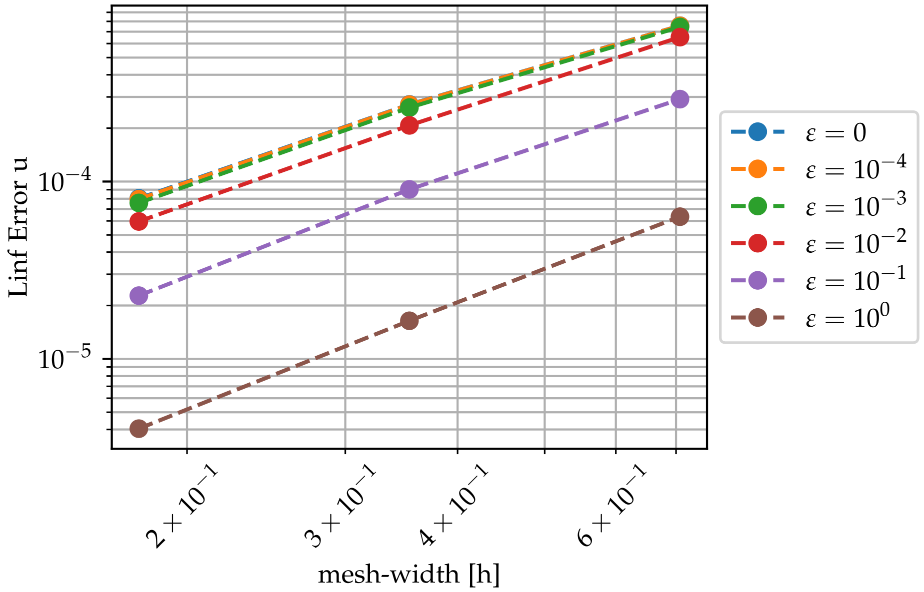

Figure C.55: Experiment 1 performed using partial scheme B using a CFL condition of $\sqrt{\frac{1}{20}}$ on a simplicial mesh for varying viscosities ε and fixed conductivity $\sigma = \infty$.

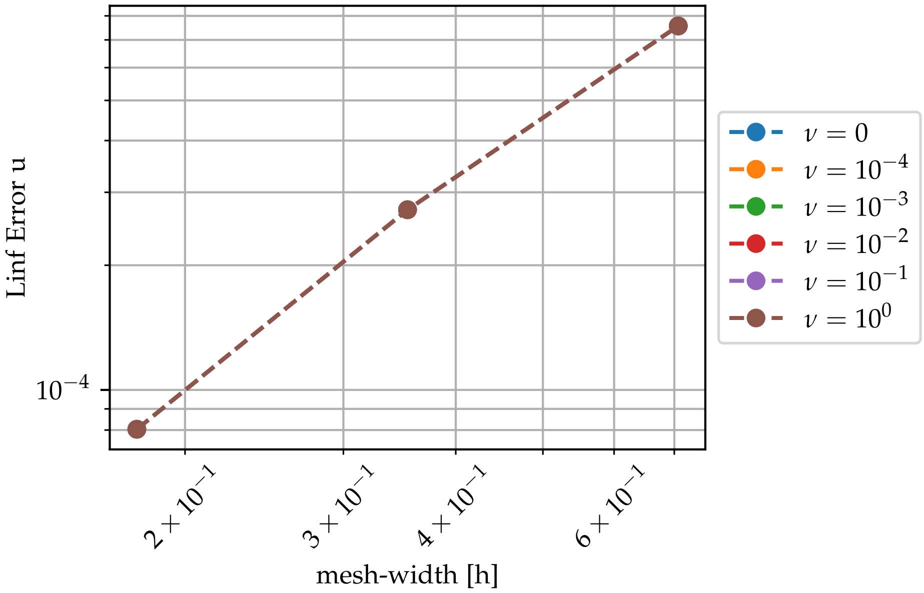

Figure C.56: Experiment 1 performed using partial scheme B using a CFL condition of $\sqrt{\frac{1}{20}}$ on a simplicial mesh for fixed viscosity $\varepsilon = 0$ and varying values for the conductivity $\sigma = \frac{1}{\nu}$.

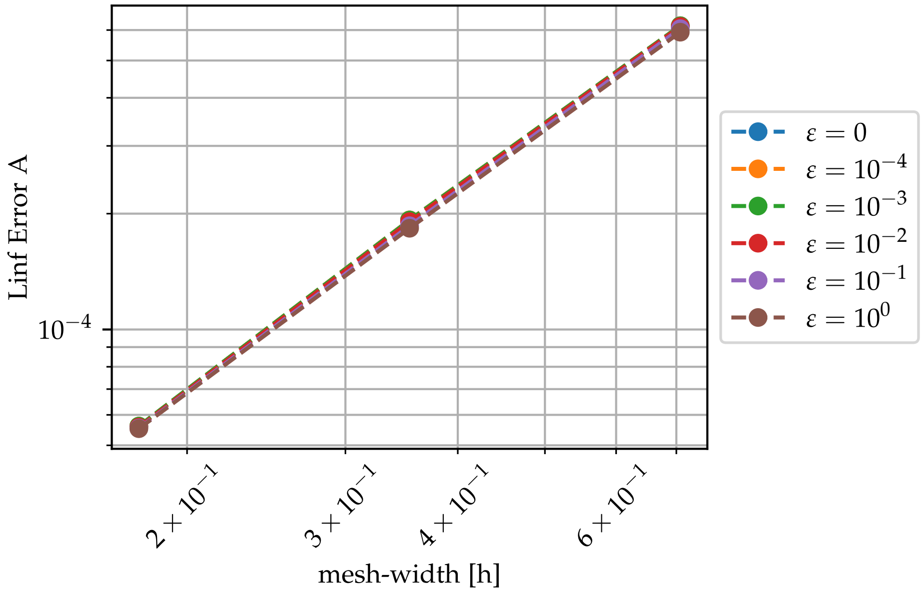

Figure C.57: Experiment 1 performed using partial scheme B using a CFL condition of $\sqrt{\frac{1}{20}}$ on a simplicial mesh for varying viscosities ε and fixed conductivity $\sigma = \infty$.

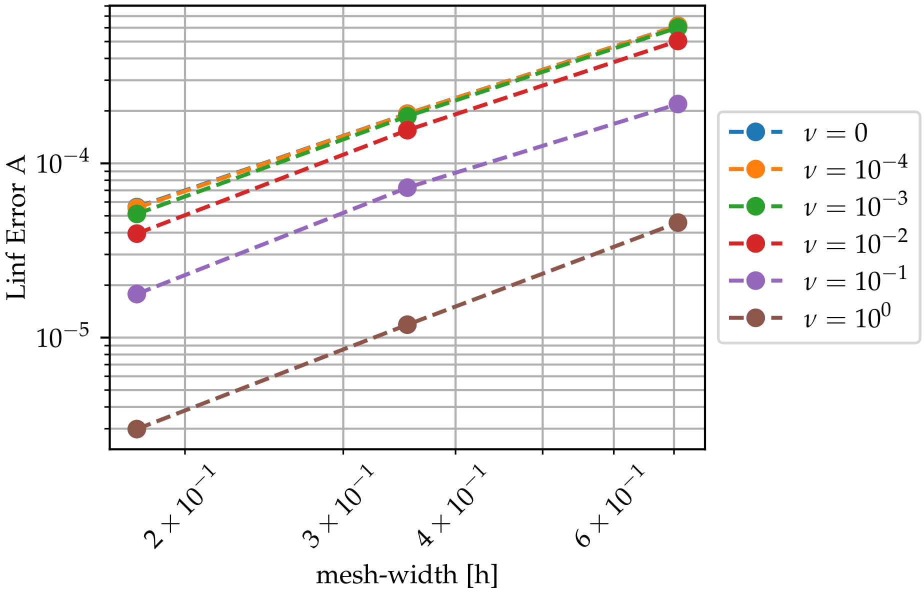

Figure C.58: Experiment 1 performed using partial scheme B using a CFL condition of $\sqrt{\frac{1}{20}}$ on a simplicial mesh for fixed viscosity $\varepsilon = 0$ and varying values for the conductivity $\sigma = \frac{1}{\nu}$.

Bibliography

[1] M Abdou, D Sze, C Wong, M Sawan, A Ying, N B Morley, and S Malang. US plans and strategy for ITER blanket testing. *Fusion Science and Technology*, 47(3):475–487, 2005.

[2] M A Abdou, A Ying, N Morley, K Gulec, S Smolentsev, M Kotschenreuther, S Malang, S Zinkle, T Rognlien, and P Fogarty. On the exploration of innovative concepts for fusion chamber technology. *Fusion Engineering and Design*, 54(2):181–247, 2001.

[3] Douglas N. Arnold. *Finite Element Exterior Calculus*.

[4] Douglas N. Arnold, Richard S. Falk, and Ragnar Whinther. *Finite element exterior calculus, homological techniques, and applications*, volume 15. 2006.

[5] V.I. Arnold. Sur la géométrie différentielle des groupes de Lie de dimension infinie et ses applications à l'hydrodynamique des fluides parfaits. 4:913–937, 1990.

[6] J P Benqué, G Labadie, and J Ronat. A new finite element method for Navier-Stokes equations coupled with a temperature equation. *Finite element flow analysis*, pages 295–302, 1982.

[7] M Bercovier and O Pironneau. Characteristics and the finite element method. *Finite Element Flow Analysis*, pages 67–73, 1982.

[8] M Bercovier, O Pironneau, and V Sastri. Finite elements and characteristics for some parabolic-hyperbolic problems. *Applied Mathematical Modelling*, 7(2):89–96, 1983.

[9] Rodolfo Bermejo and Laura Saavedra. Modified Lagrange-Galerkin methods of first and second order in time for convection-diffusion problems. *Numerische Mathematik*, 120(4), 2012.

[10] Rodolfo Bermejo and Laura Saavedra. Lagrange-Galerkin methods for the incompressible Navier-Stokes equations: A review. *Communications in Applied and Industrial Mathematics*, 7(3):23–52, 2016.

[11] Roland Berton. *Magnétohydrodynamique*. Masson, 1991.

[12] Jeremiah U Brackbill and Daniel C Barnes. The effect of nonzero div B on the numerical solution of the magnetohydrodynamic equations. *Journal of Computational Physics*, 35(3):426–430, 1980.

[13] Henri Cartan. *Differential forms*. Courier Corporation, 2006.

[14] Elena Celledoni, Bawfeh Kingsley Kometa, and Olivier Verdier. High Order Semi-Lagrangian Methods for the Incompressible Navier–Stokes Equations. *Journal of Scientific Computing*, 66(1):91–115, 2016.

[15] Alexandre Joel Chorin, Jerrold E Marsden, and Jerrold E Marsden. *A mathematical introduction to fluid mechanics*, volume 168. Springer, 1990.

[16] Luigi De Rosa. On the Helicity conservation for the incompressible Euler equations. 12 2018.

[17] Jim Douglas Jr and Thomas F Russell. Numerical methods for convection-dominated diffusion problems based on combining the method of characteristics with finite element or finite difference procedures. *SIAM Journal on Numerical Analysis*, 19(5):871–885, 1982.

[18] David G Ebin and Jerrold Marsden. Groups of Diffeomorphisms and the Motion of an Incompressible Fluid. *Annals of Mathematics*, 92(1):102–163, 1970.

[19] Alexandre Ern and Jean-Luc Guermond. *Theory and practice of finite elements*, volume 159. Springer Science \& Business Media, 2013.

[20] Richard E Ewing, Thomas F Russell, and Mary Fanett Wheeler. Convergence analysis of an approximation of miscible displacement in porous media by mixed finite elements and a modified method of characteristics. *Computer Methods in Applied Mechanics and Engineering*, 47(1-2):73–92, 1984.

[21] Alain Bossavit Francesca Rapetti. Whitney Forms of Higher Degree. *SIAM Journal on Numerical Analysis*, 47(3):2369–2386, 2009.

[22] Thomas Gallouët and Quentin Mérigot. A Lagrangian scheme for the incompressible Euler equation using optimal transport. pages 1–21, 2016.

[23] J. F. Gerbeau. A stabilized finite element method for the incompressible magnetohydrodynamic equations. *Numerische Mathematik*, 87(1):83–111, 2000.

[24] Johnny Guzmán, Chi Wang Shu, and Filánder A. Sequeira. H(div) conforming and DG methods for incompressible Euler's equations. *IMA Journal of Numerical Analysis*, 37(4):1733–1771, 2017.

[25] Y Hasbani, E Livne, and M Bercovier. Finite elements and characteristics applied to advection-diffusion equations. *Computers \& Fluids*, 11(2):71–83, 1983.

[26] Holger Heumann. Eulerian and semi-Lagrangian methods for advection-diffusion of differential forms. 2010.

[27] Holger Heumann and Ralf Hiptmair. Convergence of Lowest Order Semi-Lagrangian Schemes. *Foundations of Computational Mathematics*, 13(2):187–220, 2013.

[28] Holger Heumann, Ralf Hiptmair, Kun Li, and Jinchao Xu. Fully discrete semi-Lagrangian methods for advection of differential forms. *BIT Numerical Mathematics*, 52(4):981–1007, 2012.

[29] Ralf Hiptmair, Lingxiao Li, Shipeng Mao, and Weiying Zheng. A fully divergence-free finite element method for magnetohydrodynamic equations. *Mathematical Models and Methods in Applied Sciences*, 28(4):659–695, 2018.

[30] Paul Houston, Christoph Schwab, and Endre Süli. Discontinuous hp-finite element methods for advection-diffusion-reaction problems. *SIAM Journal on Numerical Analysis*, 39(6):2133–2163, 2002.

[31] Kaibo Hu, Yicong Ma, and Jinchao Xu. Stable finite element methods preserving div B= 0 exactly for MHD models. *Numerische Mathematik*, 135(2):371–396, 2017.

[32] Klaus Jaenich. *Vector Analysis*. 2001.

[33] George Karniadakis and Spencer Sherwin. *Spectral/hp Element Methods for Computational Fluid Dynamics*. Oxford University Press, Oxford, 2 edition, 2005.

[34] Pierre Lesaint and Pierre-Arnaud Raviart. On a finite element method for solving the neutron transport equation. *Publications mathématiques et informatique de Rennes*, (S4):1–40, 1974.

[35] J. Marsden and J. Scheurle. The reduced Euler-Lagrange equations. *Dynamics and Control of Mechanical Systems: The Falling Cat and Related Problems*, pages 139–164, 1993.

[36] Robert I McLachlan. Explicit Lie-Poisson integration and the Euler equations. *Physical review letters*, 71(19):3043, 1993.

[37] Quentin Mérigot and Jean-Marie Mirebeau. Minimal geodesics along volume-preserving maps, through semidiscrete optimal transport. *SIAM Journal on Numerical Analysis*, 54(6):3465–3492, 2016.

[38] Klas Modin. Geometric hydrodynamics: From Euler, to Poincaré, to Arnold. *arXiv*, pages 1–21, 2019.

[39] K.W. Morton, A. Priestley, and E. Suli. Stability of the Lagrange-Galerkin method with non-exact Integration. *Mathematical Modelling and Numerical Analysis*, 22(4):625–653, 1988.

[40] Andrea Natale and Colin J. Cotter. A variational H(div) finite-element discretization approach for perfect incompressible fluids. *IMA Journal of Numerical Analysis*, 38(3):1388–1419, 2018.

[41] Uno Nävert. *A finite element method for convection-diffusion problems*. Chalmers Tekniska Högskola/Göteborgs Universitet. Department of Computer Science, 1982.

[42] Ming-Jiu Ni, Ramakanth Munipalli, Peter Huang, Neil B Morley, and Mohamed A Abdou. A current density conservative scheme for incompressible MHD flows at a low magnetic Reynolds number. Part II: On an arbitrary collocated mesh. *Journal of Computational Physics*, 227(1):205–228, 2007.

[43] Ming-Jiu Ni, Ramakanth Munipalli, Neil B Morley, Peter Huang, and Mohamed A Abdou. A current density conservative scheme for incompressible MHD flows at a low magnetic Reynolds number. Part I: On a rectangular collocated grid system. *Journal of Computational Physics*, 227(1):174–204, 2007.

[44] Anthony T. Patera. A spectral element method for fluid dynamics: Laminar flow in a channel expansion. *Journal of Computational Physics*, 54(3):468–488, 1984.

[45] Olivier Pironneau. On the transport-diffusion algorithm and its applications to the Navier-Stokes equations. *Numerische Mathematik*, 38(3):309–332, 1982.

[46] Olivier Pironneau and Masahisa Tabata. Stability and convergence of a Galerkin-characteristics finite element scheme of lumped mass type. *International Journal for Numerical Methods in Fluids*, 64(10-12):1240–1253, 2010.

[47] Stéphane Popinet. Gerris: a tree-based adaptive solver for the incompressible Euler equations in complex geometries. *Journal of computational physics*, 190(2):572–600, 2003.

[48] Stéphane Popinet. The Gerris Flow Solver, 2007.

[49] A. Priestley. The Lagrange-Galerkin Method: Quadrature is Dead, Long Live Inexact Integration. Technical report, 1993.

[50] A Priestley. Exact projections and the Lagrange-Galerkin method: A realistic alternative to quadrature. *Journal of Computational Physics*, 112(2):316–333, 1994.

[51] Francesca Rapetti. High order Whitney forms on simplices.

[52] William H Reed and Thomas R Hill. Triangular mesh methods for the neutron transport equation. Technical report, Los Alamos Scientific Lab., N. Mex.(USA), 1973.

[53] Hans-G. Roos, Martin Stynes, and Lutz Tobiska. *Robust Numerical Methods for Singularly Perturbed Differential Equations*. Springer-Verlag Berlin Heidelberg, 2 edition, 2008.

[54] Thomas F Russell. Time stepping along characteristics with incomplete iteration for a Galerkin approximation of miscible displacement in porous media. *SIAM Journal on Numerical Analysis*, 22(5):970–1013, 1985.

[55] Dominik Schötzau. Mixed finite element methods for stationary incompressible magneto–hydrodynamics. *Numerische Mathematik*, 96(4):771–800, 2004.

[56] Frederic Schuller. Lectures on the Geometric Anatomy of Theoretical Physics. 2014.

[57] Günter Schwarz. *Hodge decomposition - a method for solving boundary value problems*, volume 1607. 1995.

[58] Endre Süli. Convergence and nonlinear stability of the Lagrange-Galerkin method for the Navier-Stokes equations. *Numerische Mathematik*, 53(4):459–483, 1988.

[59] K Tanaka. A characteristic finite element method using the exact integration. *Computing and Communications Center Report*, 2:11–18, 2002.

[60] Geoffrey Ingram Taylor and Albert Edward Green. Mechanism of the production of small eddies from large ones. *Proceedings of the Royal Society of London. Series A-Mathematical and Physical Sciences*, 158(895):499–521, 1937.

[61] W.R. Tonnon. https://gitlab.com/WouterTonnon/semi-lagrangian-tools, 2021.

[62] Cornelis Vuik, Fredericus Johannes Vermolen, Martin Bastiaan Gijzen, and M J Vuik. *Numerical methods for ordinary differential equations*. VSSD, 2007.

[63] D. Xiu, S. J. Sherwin, S. Dong, and G. E. Karniadakis. Strong and auxiliary forms of the semi-Lagrangian method for incompressible flows. *Journal of Scientific Computing*, 25(1):323–346, 2005.

[64] Dongbin Xiu; and George Karniadakis;. A semi-Lagrangian high-order method for Navier-Stokes equations.

[65] Shi-Jing Xu, Nian-Mei Zhang, and Ming-Jiu Ni. Influence of flow channel insert with pressure equalization opening on MHD flows in a rectangular duct. *Fusion Engineering and Design*, 88(5):271–275, 2013.

[66] V Yu Zeitlin. Algebraization of 2-d ideal fluid hydrodynamical systems and their finite-mode approximations. In *Advances in Turbulence 3*, pages 257–260. Springer, 1991.

[67] Jie Zhang and Ming-Jiu Ni. A consistent and conservative scheme for MHD flows with complex boundaries on an unstructured Cartesian adaptive system. *Journal of Computational Physics*, 256:520–542, 2014.

Eidgenössische Technische Hochschule Zürich
Swiss Federal Institute of Technology Zurich

Declaration of originality

The signed declaration of originality is a component of every semester paper, Bachelor's thesis, Master's thesis and any other degree paper undertaken during the course of studies, including the respective electronic versions.

Lecturers may also require a declaration of originality for other written papers compiled for their courses.

I hereby confirm that I am the sole author of the written work here enclosed and that I have compiled it in my own words. Parts excepted are corrections of form and content by the supervisor.

Title of work (in block letters):

A semi-Lagrangian approach to incompressible flows.

Authored by (in block letters):

For papers written by groups the names of all authors are required.

Name(s):	**First name(s):**
Tonnon	Wouter Rens

With my signature I confirm that

- I have committed none of the forms of plagiarism described in the 'Citation etiquette' information sheet.
- I have documented all methods, data and processes truthfully.
- I have not manipulated any data.
- I have mentioned all persons who were significant facilitators of the work.

I am aware that the work may be screened electronically for plagiarism.

Place, date	**Signature(s)**
Zürich, 04-11-2021	WRTonnon

For papers written by groups the names of all authors are required. Their signatures collectively guarantee the entire content of the written paper.